Supporting Information

Rare-Earth Supported Nickel Catalysts for Alkyne Semihydrogenation: Chemo- and Regioselectivity Impacted by the Lewis Acidity and Size of the Support

Bianca L. Ramirez[†] and Connie C. Lu[†,*]

[†]Department of Chemistry, University of Minnesota, Minneapolis, Minnesota 55455-0431, United States

*corresponding author e-mail: clu@umn.edu

Supporting Information Table of Contents

Experimental Section

General Considerations. Unless otherwise stated, all manipulations were performed under an inert argon atmosphere in a glovebox or using standard Schlenk techniques. Standard solvents were deoxygenated by sparging with inert gas and dried by passing through activated alumina columns of a SG Water solvent purification system. Deuterated solvents were purchased from Cambridge Isotope Laboratories, Inc. or Sigma–Aldrich, degassed via freeze−pump−thaw cycles and stored over activated 4 Å molecular sieves. The reagents $Ni(COD)_2$ and MCl_3 (M = Sc, Y, La, Ga) were purchased from Strem Chemicals and used without further purification. $^{i}Pr_2PCH_2NHPh$ (abbreviated **HL**),[1] $NiLuL_3$ (**1**),[1] and [*n*-Pr_4N][$BAr^F{}_4$][2] were synthesized according to literature procedures. 1,3,5–Trimethoxybenzene was purified by sublimation before use. Alkyne and alkene substrates were purchased from Sigma Aldrich or Alfa Aesar and used without further purification. Liquid substrates were degassed via three free–pump–thaw cycles, brought into the glove box, and stored over activated 4 Å molecular sieves. Elemental analyses were performed by Robertson Microlit Laboratories (Ledgewood, NJ).

NMR Spectroscopy. ^1H, ^2H, ^{13}C, ^{31}P NMR spectra were recorded on Varian 500 MHz or Bruker 400 MHz spectrometers at ambient temperature unless otherwise stated.^1H and ^{13}C chemical shifts were referenced to residual solvent. ^{31}P spectra were referenced to external 85% phosphoric acid (δ = 0 ppm). $T_{1(min)}$ values were determined by fitting the pulse-recovery ^1H spectra at various temperatures using the T_1 calculation protocols in Bruker Topspin software.

Cyclic voltammetry. Cyclic voltammograms were collected with a CH Instruments 600 electrochemical analyzer with a one–cell setup, comprising a glassy carbon working electrode, a platinum wire counter electrode, and Ag/AgCl reference electrode. Analytes were dissolved in 0.1 M [*n*-Pr_4N][$BAr^F{}_4$] ($BAr^F{}_4$ = tetrakis(3,5-bis(trifluoromethyl)phenyl)borate)) in difluorobenzene, and internally referenced to the $FeCp_2/FeCp_2^+$ redox couple.

Synthesis of Li($^{i}Pr_2PCH_2NPh$) (abbreviated **Li·L**). In a 20 mL scintillation vial, a solution of **HL** (0.500g, 2.24 mmol) in hexanes (~10 mL) was cooled to –60 ºC in a dry ice/acetone coldwell. *n*-BuLi (0.896 mL, 2.5 M in hexanes, 2.24 mmol) was then added, and the mixture stirred for 1 h at room temperature. The resulting white precipitate was isolated on a fine glass fritted Büchner funnel, washed with hexanes (3 x 5 mL), and dried in vacuo to give the desired product as a white powder (0.482 g, 94 %).

$^1H\{^{31}P\}$ NMR (400 MHz, C_6D_6): δ 7.21 (br t, 2H, aryl), 6.67 (br d, 2H, aryl), 6.48 (br t, ^3J = 6.9 Hz, 1H, aryl), 3.39 (s, 2H, CH_2P), 1.68 (br, 2H, CHMe$_2$), 1.08−1.04 (m, 12H, CH_3).^{31}P (162 MHz, C_6D_6): δ 2.7. Due to the poor solubility of **Li·L** in aromatic solvents, the ^{13}C NMR spectrum in C_6D_6 was not collected.

$^1H\{^{31}P\}$ NMR (400 MHz, THF–d_8): δ 6.63 (t, ^3J = 6.9 Hz, 2H, aryl), 6.08 (d, ^3J = 8.1 Hz, 2H, aryl), 5.70 (t, ^3J = 7.0 Hz, 1H, aryl), 3.25 (s, 2H, CH_2P), 1.75 (m, 2H, CHMe$_2$), 1.10 (m, 12H, CH_3 and C′H_3). ^{31}P (162 MHz, THF–d_8): δ –1.7. $^{13}C\{^1H\}$ NMR (126 MHz, THF–d_8): δ 162.6 (d, $J_{C–P}$ = 15.4 Hz, aryl), 128.6 (aryl), 113.0 (br, aryl), 105.8 (aryl), 47.3 (*C*H$_2$P), 24.0 (d, $^2J_{C–P}$ = 14.6 Hz, P*C*HMe$_2$), 20.3 (d, $^1J_{C–P}$ = 12.0 Hz, *C*H$_3$), 20.1 (d, $^1J_{C–P}$ = 12.0 Hz, *C*H$_3$).

General synthetic route to monometallic complexes 2 and 3.

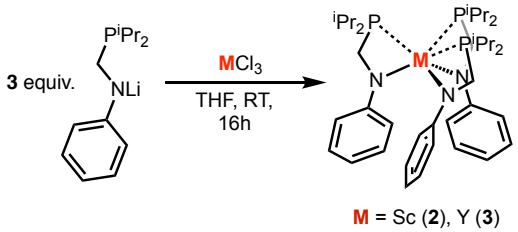

In a 20 mL scintillation vial, a solution of **Li·L** (0.200 g, 0.872 mmol) in THF (~6 mL) was added to a stirring solution of MCl_3 (0.291 mmol, M = Sc or Y) in THF (~10 mL) at room temperature and stirred overnight. After drying the solution in vacuo, the resulting crude solid was washed with hexanes (8 mL). The product was then extracted into benzene, filtered through a Celite pad, and dried in vacuo to afford the desired product.

Sc(^{i}Pr$_2$PCH$_2$NPh)$_3$ (abbreviated **ScL$_3$**, or **2**). The product was obtained as a white powder (0.175 g, 85%). Single crystals were grown by layering a concentrated benzene solution of **2** with hexanes. ^{1}H{^{31}P} NMR (400 MHz, C_6D_6): δ 7.24 (t, ^{3}J = 7.8 Hz, 6H, aryl), 7.11 (d, ^{3}J = 8.3 Hz, 6H, aryl), 6.72 (t, ^{3}J = 7.8 Hz, 3H, aryl), 3.57 (br, 3H, C*H*H′P), 3.47 (br, 3H, CH*H*′P), 1.97 (br, 3H, C*H*Me$_2$), 1.76 (br, 3H, C′*H*Me$_2$), 1.16–0.86 (m, 36H, C*H*$_3$). ^{31}P NMR (162 MHz, C_6D_6): δ −18.8. ^{13}C{^{1}H} NMR (126 MHz, C_6D_6): δ 156.2 (aryl), 129.2(aryl), 116.5(aryl), 114.9(aryl), 44.7 (*C*H$_2$P), 24.5 (P*C*HCH$_3$), 24.0 (P*C*′HCH$_3$), 21.1 (*C*H$_3$), 19.8 (*C*H$_3$), 19.3 (*C*H$_3$), 18.9 (*C*H$_3$). Anal. Calcd. for **2**(H$_2$O)$_3$, $C_{39}H_{69}N_3O_3P_3Sc$: C 65.79; H 8.93, N 5.91. Found: C 65.31; H 9.10; N 5.82. Combustion analysis is consistent with addition of 3 water molecules.

Y(^{i}Pr$_2$PCH$_2$NPh)$_3$ (abbreviated **YL$_3$**, or **3**). The product was obtained as a white powder (0.287 g, 88%). Single crystals were grown by layering a concentrated benzene solution of **3** with hexanes. ^{1}H{^{31}P} NMR (400 MHz, C_6D_6): δ 7.26 (t, ^{3}J = 7.7 Hz, 6H, aryl), 7.02 (d, ^{3}J = 7.9 Hz, 6H, aryl), 6.71 (t, ^{3}J = 7.3 Hz, 3H, aryl), 3.49 (s, 6H, C*H*$_2$P), 1.74 (br, 6H, C*H*Me$_2$), 0.94 (br, 36H, C*H*$_3$). ^{31}P NMR (162 MHz, C_6D_6): δ −14.1 (d, J_{P-Y} = 36.5 Hz). ^{13}C{^{1}H} NMR (126 MHz, C_6D_6): δ 156.5 (aryl), 129.2 (aryl), 115.4 (aryl), 113.7 (aryl), 43.0 (*C*H$_2$P), 23.2 (P*C*HCH$_3$), 18.94 (*C*H$_3$). Anal. Calcd. for **3**(H$_2$O)$_3$, $C_{39}H_{69}N_3P_3YO_3$: C 57.84; H 8.59; N 5.19. Found: C 57.22; H 8.41; N 5.56. Combustion analysis is consistent with addition of 3 water molecules.

Synthesis of La(^{i}Pr$_2$PCH$_2$NPh)$_3$ (abbreviated **LaL$_3$**, or **4**).

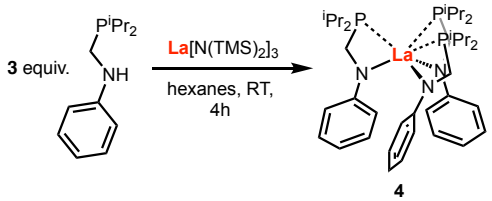

In a 20 mL scintillation vial, a solution of **HL** (0.200 g, 0.896 mmol) in hexanes (~10 mL) was added to a stirring solution of La[N(TMS)$_2$]$_3$ (0.185 g, 0.296 mmol) in hexanes (~8 mL) at room temperature. The solution was stirred for 4 h during which an off–white solid precipitated. After drying the solution in vacuo, the resulting crude solid was washed with hexanes (8 mL). The product was then extracted into benzene, filtered through a Celite pad, and dried in vacuo to afford the desired product as a white powder (0.165 g, 70%). Single crystals were grown by layering a concentrated benzene solution of **4** with hexanes. ^{1}H{^{31}P} NMR (400 MHz, C_6D_6): δ 7.32 (t, ^{3}J =

7.8 Hz, 6H, aryl), 6.90 (d, ^3J = 7.9 Hz, 6H, aryl), 6.74 (t, ^3J = 7.2 Hz, 3H, aryl), 3.53 (s, 6H, CH_2P), 1.72 (app pentet, ^3J = 7.1 Hz, 6H, CHMe$_2$), 0.97 (dd, ^3J = 7.1 & 2.9 Hz, 36H, CH_3). ^{31}P NMR (162 MHz, C_6D_6): δ −12.6. ^{13}C{^{1}H} NMR (126 MHz, C_6D_6): δ 156.5 (aryl), 130.2 (aryl), 115.1 (aryl), 112.1 (aryl), 43.1 (*C*H_2P), 23.5 (P*C*HCH$_3$), 19.3 (*C*H$_3$), 18.8 (*C*H$_3$). Anal. Calcd. for **4**(H_2O), $C_{39}H_{64}N_3OP_3La$: C 56.84; H 7.96; N 5.10. Found: C 56.60; H 8.32; N 5.08. Combustion analysis is consistent with addition of one water molecule.

Synthesis of Li$_3$·Ni(^{i}Pr$_2$PCH$_2$NPh)$_3$ (abbreviated **Li$_3$·NiL$_3$**, or **5**).

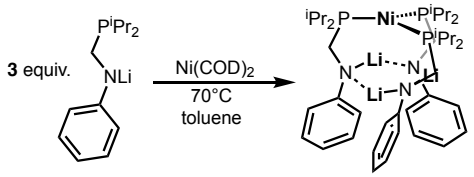

5

In a 20 mL scintillation vial, a solution of Ni(COD)$_2$ (0.060 g, 0.218 mmol) in toluene (~6 mL) was added to a stirring suspension of **Li·L** (0.150 g, 0.654 mmol) in toluene (~5 mL). The solution was heated to 70°C for 10 min to promote dissolution of **Li·L** and then stirred overnight at room temperature. The resulting purple precipitate was isolated on a fine glass fritted Buchner funnel, washed with toluene (5 mL) and hexanes (5 mL), and dried in vacuo to give the desired product as a purple powder (0.147 g, 90%). Single crystals were grown by recrystallization from hot toluene. ^{1}H{^{31}P} NMR (400 MHz, C_6D_6/THF–*d*$_8$): δ 7.27 (t, ^3J = 7.7 Hz, 6H, aryl), 6.97 (d, ^3J = 7.9 Hz, 6H, aryl), 6.57 (t, ^3J = 7.3 Hz, 3H, aryl), 3.62 (s, 6H, CH_2P), 2.14 (br, 6H, CHMe$_2$), 1.34−1.22 (br, 36H, CH_3). ^{31}P NMR (162 MHz, C_6D_6): δ 20.1. ^{13}C{^{1}H} NMR (126 MHz, C_6D_6/THF): δ 161.1 (aryl), 129.8 (aryl), 115.2 (aryl), 112.6 (aryl), 56.1 (*C*H_2P), 30.6 (P*C*HMe$_2$), 22.2 (*C*H$_3$), 19.5 (*C*H$_3$). Anal. Calcd. for **5**(H_2O)$_3$, $C_{39}H_{69}N_3O_3P_3Li_3Ni$: C 58.52; H 8.69; N 5.25. Found: C 58.48; H 8.47; N 5.21. Combustion analysis is consistent with addition of 3 water molecules.

General synthetic route to bimetallic Ni-rare earth complexes 6–8.
A solution of **2**, **3**, or **4** (0.150 g, 0.213 mmol) in toluene (~6 mL) was transferred to a Schlenk tube containing solid Ni(COD)$_2$ (1 equiv). The reaction was heated at 70 °C for 16 h, during which red crystals precipitated. The crystals were collected and washed with hexanes. Isolated crystals were used for determination of solid–state structure and elemental analysis. Alternatively, **6–8** can be synthesized by the addition of a solution of ML$_3$ (0.150 g, 0.213 mmol), where M is Sc, Y, or La, in THF (~4 mL) to a 20 mL scintillation vial charged with solid Ni(COD)$_2$ (0.213 mmol). The reaction was stirred for 16 h at room temperature and then dried in vacuo. Before workup, toluene (1−2 mL) was added to the crude solid and removed in vacuo twice to remove any residual THF. The crude was washed with hexanes (6 mL) and toluene (3 mL). The product was then extracted into hot toluene, filtered through a Celite pad, and dried in vacuo.

NiSc(^{i}Pr$_2$PCH$_2$NPh)$_3$ (abbreviated **NiScL$_3$**, or **6**). Isolated as a bright red powder or crystals (0.147 g, 90% yield, crystalline yield 75%). ^{1}H{^{31}P} NMR (400 MHz, toluene–*d*$_8$): δ 7.13 (t, ^3J = 7.6 Hz, 6H, aryl), 6.63 (m, 9H, aryl), 3.96 (s, 6H, CH_2P), 2.25 (sept, ^3J = 7.3 Hz, 6H, CHMe$_2$), 1.03 (dd, ^3J = 16.7 & 7.1 Hz, 18H, CH_3). ^{31}P NMR (162 MHz, toluene–*d*$_8$): δ 3.1. Due to the poor solubility of **6** in solvents at room temperature, a ^{13}C NMR spectrum was not collected. Anal. Calcd. for **6**, $C_{39}H_{63}N_3P_3NiSc$: C 60.79; H 8.24; N 5.45. Anal. Calcd. for **6**(H_2O)$_2$,

$C_{39}H_{67}N_3O_2P_3NiSc$: C 58.08; H 8.37; N 5.21. Found: C 57.77; H 8.27; N 4.97. Combustion analysis is consistent with addition of 2 water molecules.

NiY(^{i}Pr$_2$PCH$_2$NPh)$_3$ (abbreviated **NiYL$_3$**, or **7**). Isolated as red–orange powder or crystals (0.160 g, 92% yield, crystalline yield 80 %). Single crystals of **7**–**THF** were grown by layering hexane on a concentrated THF solution of **7** at –28 °C. ^{1}H{^{31}P} NMR (400 MHz, toluene–d_8): δ 7.22 (t, ^3J = 7.7 Hz, 6H, aryl), 6.63 (t, ^3J = 7.2 Hz, 3H, aryl), 6.51 (d, ^3J = 8.1 Hz, 6H, aryl), 3.93 (s, 6H, CH_2P), 2.21 (sept, ^3J = 7.2 Hz, 6H, CHMe$_2$), 1.10 (d, ^3J = 7.1 Hz, 18H, CH_3), 1.03 (d, ^3J = 7.1 Hz, 18H, C′H_3). Due to the poor solubility of **7** in aromatic solvents at room temperature, the ^{13}C NMR spectrum in C_6D_6 was not collected. ^{31}P NMR (162 MHz, toluene–d_8): δ 2.8. Anal. Calcd. for **7**(H_2O)$_3$, $C_{39}H_{69}N_3O_3P_3YNi$: C 53.91; H 8.01; N 4.83. Found: C 53.75; H 8.16; N 4.65. Combustion analysis is consistent with addition of 3 water molecules.

NMR data for **7**–THF: ^{1}H{^{31}P} NMR (400 MHz, THF–d_8): δ 6.92 (t, ^3J = 7.7 Hz, 6H, aryl), 6.52 (d, ^3J = 8.0 Hz, 6H, aryl), 6.31 (t, ^3J = 7.2 Hz, 3H, aryl), 3.88 (s, 6H, CH_2P), 2.45 (sept, ^3J = 7.2 Hz, 6H, CHMe$_2$), 1.29 (app t, J = 6.2 Hz, 36H, CH_3). ^{31}P NMR (162 MHz, THF–d_8): δ 10.7. ^{13}C{^{1}H} NMR (126 MHz, THF–d_8): δ 158.8 (aryl), 129.0 (aryl), 115.8 (aryl), 114.2 (aryl), 55.5 (*C*H$_2$P), 29.1 (P*C*HMe$_2$), 21.5 (*C*H$_3$), 19.7 (*C*H$_3$).

NiLa(^{i}Pr$_2$PCH$_2$NPh)$_3$ (abbreviated **NiLaL$_3$**, or **8**). Isolated as an orange powder or crystals (0.156 g, 85%, crystalline yield 72 %). Single crystals of **8** were grown by recrystallization from hot *p*–xylene, and the solid-state structure is reported in the main text. Another solid-state conformer of NiLaL$_3$, **8'**, was crystallized from hot toluene. Refer to X-ray details in the SI. The structure of **8'** features a η^2-(N-C$_{ipso}$) interaction between the NPh group and the La center. ^{1}H{^{31}P} NMR (400 MHz, C_6D_6): δ 7.33 (t, ^3J = 7.8 Hz, 6H, aryl), 6.65 (t, ^3J = 7.2 Hz, 3H, aryl), 6.40 (d, ^3J = 7.8 Hz, 6H, aryl), 3.93 (s, 6H, CH_2P), 2.12 (m, 6H, CHMe$_2$), 1.06 (dd, ^3J = 15.6, 7.1 Hz 36H, CH_3). ^{31}P NMR (162 MHz, C_6D_6): δ 1.7. Due to the poor solubility of **7** in aromatic solvents at room temperature, the ^{13}C{^{1}H} NMR spectrum in C_6D_6 was not collected. Anal. Calcd. for **8**(H_2O), $C_{39}H_{65}N_3OP_3NiLa$: C 53.08; H 7.42; N 4.76. Found: C 53.02; H 7.10; N 4.16. Combustion analysis is consistent with addition of one water molecule.

NMR data for **8**–THF: ^{1}H{^{31}P} NMR (400 MHz, THF–d_8, 25°C): δ 6.93 (t, ^3J = 7.8 Hz, 6H, aryl), 6.34 (d, ^3J = 7.9 Hz, 6H, aryl), 6.27 (t, ^3J = 7.1 Hz, 3H, aryl), 3.94 (s, 6H, CH_2P), 2.45 (sept, ^3J = 7.2 Hz, 6H, CHMe$_2$), 1.28 (app t, J = 6.2 Hz, 36H, CH_3). ^{31}P NMR (162 MHz, THF–d_8): δ 4.2. ^{13}C NMR (126 MHz, THF–d_8): δ 157.8 (aryl), 129.9 (aryl), 113.5 (aryl), 113.4 (aryl), 54.9 (*C*H$_2$P), 29.0 (P*C*HMe$_2$), 21.2 (*C*H$_3$), 19.9 (*C*H$_3$).

Synthesis of NiGa(^{i}Pr$_2$PCH$_2$NPh)$_3$ (abbreviated **NiGaL$_3$**, or **9**). A solution of $GaCl_3$ (0.035 g, 0.201 mmol) in Et_2O (~4 mL) was added to a stirring solution of **5** (0.150 g, 0.201 mmol) in Et_2O (~4 mL), resulting in an orange–brown color. The reaction was stirred for 6 h, filtered through a Celite pad to remove LiCl, and dried in vacuo. The crude was then washed with hexanes (6 mL) and diethyl ether (4 mL). After drying in vacuo, a red-brown powder was obtained (0.096 g, 60% yield). Single crystals were grown by layering a concentrated benzene solution of **9** with hexanes. ^{1}H{^{31}P} NMR (400 MHz C_6D_6): δ 7.21 (t, ^3J = 7.7 Hz, 6H, aryl), 7.03 (d, ^3J = 8.2 Hz, 6H, aryl), 6.69 (t, ^3J = 7.2 Hz, 3H, aryl), 3.40 (s, 6H, CH_2P^{i}Pr$_2$), 2.22 (sept, ^3J = 7.2 Hz, 6H, CHMe$_2$), 0.99 (app t, ^3J = 7.9 Hz, 36H, CH_3). ^{31}P NMR (162 MHz, C_6D_6): δ 31.8. ^{13}C{^{1}H} NMR (126 MHz,

C_6D_6): δ 153.4 (aryl), 129.5 (aryl), 115.7 (aryl), 114.6 (aryl), 50.2 (*C*H_2P), 29.4 (P*C*HMe_2), 20.7 (*C*H_3), 18.7 (*C*H_3). Anal. Calcd. for **9**(H_2O), $C_{39}H_{65}N_3OP_3GaNi$: 57.59 C, 8.05 H, 5.16 N. Found: C 57.34, H 7.89, N 4.97. Combustion analysis is consistent with addition of one water molecule.

***In situ* generation of (H$_2$)NiGa(^{i}Pr$_2$PCH$_2$NPh)$_3$** (abbreviated **(H$_2$)NiGaL$_3$**, or **9–H$_2$**). A solution of **9** (0.015 g, 0.019 mmol) in either C_6D_6 or toluene–d_8 (c. 0.5 mL) was added to a J. Young NMR tube. One freeze-pump-thaw cycle was performed to evacuate the headspace. Subsequent exposure to H_2 (1 atm) resulted in the solution changing color from dark red to orange–red. Lability of H_2 precluded elemental analysis from being obtained. ^{1}H NMR (400 MHz C_6D_6): δ 7.23 (t, ^3J = 7.7 Hz, 6H, aryl), 7.14 (d, ^3J = 9.1 Hz, 6H, aryl), 6.72 (t, ^3J = 7.2 Hz, 3H, aryl), 3.31 (s, 6H, CH_2P^{i}Pr$_2$), 1.85 (sept, ^3J = 7.6 Hz, 6H, C*H*Me$_2$), 0.95 (s, ^3J = 7.8 Hz, 36H, CH_3). −2.03 (br, 2H, Ni-H_2). ^{31}P NMR (162 MHz, C_6D_6): δ 48.5. T_1(min) (500 MHz, –20 °C) = 27.8(4) ms.

***In situ* generation of (HD)NiGa(^{i}Pr$_2$PCH$_2$NPh)$_3$** (abbreviated **(HD)NiGaL$_3$**, or **9–HD**). A solution of **9** (0.015 g, 0.019 mmol) in either C_6D_6 or toluene–d_8 (~0.5 mL) was added to a J. Young NMR tube. Two freeze-pump-thaw cycle was performed to evacuate the headspace. Subsequent exposure to HD (1 atm) resulted in the solution changing color from dark red to orange–red. To observe HD coupling, the NMR spectrum was collected at –62 °C. ^{1}H{^{31}P} NMR (400 MHz, C_6D_6, –62 °C): δ 7.28 (t, ^3J = 7.7 Hz, 6H, aryl), 7.16 (d, ^3J = 9.1 Hz, 6H, aryl), 6.8 (t, ^3J = 7.2 Hz, 3H, aryl), 3.26 (br, 3H, CH_2P^{i}Pr$_2$), 3.14 (br, 3H, CH_2P^{i}Pr$_2$), 1.84 (br, 6H, C*H*Me$_2$), 1.64 (br, 3H, C*H*Me$_2$), 0.90 (m, ^3J = 7.8 Hz, 36H, CH_3). −3.07 (t, J_{HD} = 34.7 Hz, Ni-*H*D,). ^{31}P{^{1}H} NMR (162 MHz, C_6D_6, –62 °C): δ 48.8.

In situ* generation of (η^2-PhC≡CPh)NiY(^{i}Pr$_2$PCH$_2$NPh)$_3$** (abbreviated as **7–**DPA). A J. Young NMR tube was charged with **7** (0.025 g, 0.031 mmol). A solution of diphenylacetylene (0.027 g, 0.153 mmol) in C_6D_6 or toluene–d_8 (~0.5 mL) was then added to the J. Young NMR tube. The tube was then heated at 60 °C until the solution became homogeneous (~5 min). ^{1}H{^{31}P} NMR (400 MHz C_6D_6): δ 7.52 (dt, ^3J = 7.5, 1.7 Hz, 4H, alkyne aryl CH), 7.31 (t, ^3J = 7.6 Hz, 4H, aryl CH), 7.24 (t, ^3J = 7.6 Hz, 4H, aryl CH), 7.10 (d, ^3J = 8.9 Hz, 2H, aryl CH), 7.06 (d, ^3J = 7.5 Hz, 2H, aryl CH), 6.98 (q, ^3J = 6.5 Hz, 6H, alkyne aryl CH), 6.78 (t, ^3J = 7.2 Hz, 2H, aryl CH), 6.60 (t, ^3J = 7.2 Hz, 1H, aryl CH), 3.90 (m, 4H, CH_2P^{i}Pr$_2$), 3.34 (s, 2H, CH_2P^{i}Pr$_2$), 2.24 (h, ^3J = 6.9 Hz, 2H, C*H*Me$_2$), 2.10 (h, ^3J = 6.8 Hz, 2H, C*H*Me$_2$), 1.71 (h, ^3J = 7.1 Hz, 2H, C*H*Me$_2$), 1.11 (d, ^3J = 7.4 Hz, 36H, CH_3), 1.00 (t, ^3J = 7.2 Hz, 12H, CH_3), 0.94 (dd, ^3J = 11.8, 7.1 Hz, 6H, CH_3) 0.91 (dd, ^3J = 7.1, 5.3 Hz, 6H, CH_3), 0.71 (dd, ^3J = 7.2, 2.7 Hz, 6H, CH_3). ^{31}P NMR (162 MHz, C_6D_6): δ 30.4 (s, 2P), –11.5 (d, $^1J_{P\text{-}Y}$ = 48.4 Hz, 1P). ***Crystallization of 7–DPA. In a 20–mL scintillation vial, a solution of diphenylacetylene (0.109 g, 0.613 mmol) in toluene (~3 mL) was added to a stirring solution of $NiYL_3$ (0.050 g, 0.061 mmol) in toluene (~5 mL) at room temperature. The solution was then heated at 60 °C until the solution became homogeneous (~5 min). During heating, the solution changed color from red to light yellow. The reaction was then cooled to room temperature and filtered through a Celite pad to remove any unreacted **7**. The filtrate was then concentrated to ~1 mL under vacuum and layered with hexanes (2 mL) to obtain **7–**DPA as yellow crystals.

Standard catalytic procedure for alkyne semihydrogenation.
Catalyst stock solutions were prepared in toluene–d_8 to make enough individual aliquots of 5.6 μmol of catalyst (**1** and **6**–**9**), 40 equiv alkyne (0.45 M in 0.5 mL toluene–d_8) and 1,3,5-trimethoxybenzene (0.02 mmol) as an internal integration standard. If the catalyst did not fully dissolve, then the stock solution was heated at 70 °C until homogenous. All catalytic runs were performed in J. Young NMR tubes and in triplicate, unless otherwise indicated. The reaction tubes were subjected to a single freeze–pump–thaw cycle to evacuate the headspace, cooled in a LN_2 bath, and backfilled with 1 atm of H_2 1 atm at 77 K. The mixture was allowed to warm to room temperature, resulting in 4 atm of H_2 gas.[3] The reaction was mixed by inverting the NMR tube 3 times, and then heated to 70 °C in an oil bath. Conversion was monitored via ^{1}H NMR spectroscopy by integration of the aryl protons of the alkyne against those of the internal standard (recycle delay = 20s). For catalytic runs with **7**–THF, THF-d_8 was used as the solvent.

General procedure for initial rate studies.
Catalyst stock solutions were prepared according to the procedure described above using either diphenylacetylene or (*Z*)-stilbene as the substrate. After H_2 was added, the J. Young NMR reaction tube was placed inside a Bruker AM 400 NMR instrument that was preheated to 344 K. ^{1}H NMR data was collected every 30 to 180 seconds until either 10 % conversion was reached or for 45-60 min. All kinetic experiments were performed in triplicate. Kinetic data was analyzed and fit to a straight line, yielding adjusted R^2 values ≥0.99 using Mestrenova Reaction Monitoring software and OriginLab.

Standard catalytic procedure for (*Z*)-stilbene isomerization.
Catalyst stock solutions were prepared according to the procedure described above using (*Z*)-stilbene as the substrate. The procedure was also identical to that described for alkyne semihydrogenation, except that conversion was monitored via ^{1}H NMR spectroscopy by integration of the vinylic protons of (*Z*)-stilbene against those of the internal standard (recycle delay = 20s).

X–ray Crystallographic and Structure Refinement Details

A yellow plate of **2** (0.130 x 0.110 x 0.080 mm), colorless plate of **3** (0.12 x 0.08 x 0.04 mm) and **4** (0.15 x 0.15 x 0.05 mm), a red plate of **5** (0.12 x 0.04 x 0.02 mm), red blocks of **6** (0.1 x 0.08 x 0.04 mm), **7** (0.12 x 0.11 x 0.05 mm), **8** (0.12 x 0.12 x 0.08 mm), **8'** (0.13 x 0.13 x 0.08 mm), and **9** (0.12 x 0.10 x 0.07 mm), an orange block of **7–**THF (0.12 x 0.06 x 0.02 mm), and a yellow plate of **7**–DPA(0.13 x 0.08 x 0.05 mm) were mounted on a 200 μm MiTeGen microloop and placed on a Bruker PHOTON-II CMOS or Bruker APEX-II CCD diffractometer for data collection at either 100(2) or 123(2)K. The data collection was carried out using Mo Kα radiation (graphite monochromator). The data intensity was corrected for absorption and decay (SADABS).[4] Final cell constants were obtained from least–squares fits of all measured reflections. The structure was solved using SHELXT–2014/5[5] and refined using refined using SHELXL-2016/6.[6-7] A direct–methods solution was calculated which provided most non–hydrogen atoms from the E–map. Full matrix least–squares/difference Fourier cycles were performed to locate the remaining non–hydrogen atoms. All non–hydrogen atoms were refined with anisotropic displacement parameters. Hydrogen atoms were placed in ideal positions and refined as riding atoms with relative isotropic displacement parameters. Disordered solvent molecules that were unmodelable were removed from the unit cells of **6**, **8**, **7–**THF, and **7–**DPA using the SQUEEZE function of PLATON.[8-9]

Three reflections for **3** and two reflections for **7**–DPA were found to have been affected by the beamstop and were removed in their final refinement. The crystal structure of **4** contained a disordered isopropyl group and was modeled using the SAME restraint and EADP constraint. Complex **6** crystallized in the space group $R\bar{3}$ and contained a disordered toluene solvent molecule on a 3-fold rotation axis and adjacent to an inversion center. All attempts to model this solvent were unsuccessful. The SQUEEZE function removed 155 electrons from a void-space volume of 849 Å. This value is consistent with the presence of approximately three toluene molecules in the unit cell. The structure of **7** contained a toluene solvent molecule that was disordered over an inversion center. Each carbon atom was refined with 50% occupancy and modeled using the SAME restraint and EADP constraint. Complex **8** crystallized in the space group $Pa\bar{3}$ and contained a *p*–xylene solvent molecule on the 3-fold rotation axis and adjacent to an inversion center. Attempts to model this solvent were unsuccessful. The SQUEEZE function removed 325 electrons from a void-space volume of 1472 Å. This value is consistent with the presence of approximately six *p*–xylene molecules in the unit cell. Complex **7**–THF crystallized in the space group $P\bar{1}$ and contained a disordered THF solvent molecule on an inversion axis. Attempts to model this solvent were unsuccessful. The SQUEEZE function removed 93 electrons from a void-space volume of 371 Å. This value is consistent with the presence of approximately two THF molecules in the unit cell. In addition, a disordered aryl group was modeled using the EXYZ and EADP constraint. Complex **7**–DPA contained a disordered aryl group which was modeled using the SAME restraint and EADP constraint. Additionally, **7**–DPA had two disordered isopropyl groups which were modeled using the EADP constraint. Complex **7**–DPA crystallized in the space group $P2_1/n$ and contained a channel of hexanes along the crystallographic *b* axis. Attempts to model this solvent were unsuccessful. The SQUEEZE function removed 158 electrons from a void-space volume of 834 Å. This value is consistent with the presence of approximately three hexane molecules in the unit cell. Complex **8'** contained a disordered $[^{i}Pr_2PCH_2NPh]^{-}$ ligand which was modeled using the SAME restraint and EADP constraint. Additionally, a toluene solvent molecule was disordered over an inversion center. Each carbon atom was placed into a PART -1 and refined using the SAME restraint.

Table S1. **Crystallographic Details for Monometallic Complexes 2–4, and 5.**

	2 (ScL_3)	**3 (YL_3)**	**4 (LaL_3)**	**5 ($Li_3{\cdot}NiL_3$)**
chemical formula	$C_{39}H_{63}N_3P_3Sc$	$C_{39}H_{63}N_3P_3Y$	$C_{39}H_{63}N_3P_3La$	$C_{39}H_{63}N_3P_3Li_3Ni$
CCDC No.	1979226	1979224	1979228	1979223
fw	711.79	755.74	805.74	746.36
cryst syst	triclinic	triclinic	triclinic	trigonal
space group	$P\bar{1}$	$P\bar{1}$	$P\bar{1}$	$P\bar{3}c1$
a (Å)	10.730(2)	10.7947(9)	10.4219(3)	13.807(5)
b (Å)	11.645(3)	11.3362(11)	11.1063(3)	13.807(5)
c (Å)	17.343(3)	18.6897(19)	19.6256(6)	25.285(9)
α (°)	92.598(7)	91.847(3)	83.9500(10)	90
β (°)	95.124(7)	92.356(2)	82.0920(10)	90
γ (°)	109.713(8)	117.344(2)	65.7240(10)	120
V(Å^3)	2025.2(7)	2026.4(3)	2048.08(10)	4175(3)
Z	2	2	2	4
D_{cald} (g cm^{-3})	1.167	1.239	1.307	1.188
λ (Å), μ (mm^{-1})	0.71073, 0.330	0.71073, 1.587	0.71073, 1.189	0.71073, 0.609
T	100(2)	100(2)	100(2)	100(2)
θ (°)	2.286 – 26.371	2.185 – 26.732	2.221 – 28.279	2.344 – 26.369
relns collected	28298	54483	39583	53542
unique relfns	6749	7167	9422	2293
data/restraint/parameters	8237/0/427	8624/0/427	10149/7/450	2858/0/152
R_1, wR_2 (I>2σ (I))	0.0344, 0.0725	0.0399, 0.0917	0.0209, 0.0459	0.0380, 0.0750

Table S2. Crystallographic Details for Heterobimetallic Complexes 6–9, 7–DPA, 7–THF and 8'.

	6 (NiScL$_3$)	**7 (NiYL$_3$)**	**8 (NiLaL$_3$)**	**9 (NiGaL$_3$)**	**7**–DPA	**7**–THF	**8'**[a]
chemical formula	$C_{39}H_{63}N_3P_3ScNi$	$C_{39}H_{63}N_3P_3YNi\cdot C_7H_8$	$C_{39}H_{63}N_3P_3LaNi$	$C_{39}H_{63}N_3P_3GaNi$	$C_{53}H_{73}N_3P_3YNi$	$C_{43}H_{71}N_3P_3OYNi$	$C_{39}H_{63}N_3P_3LaNi\cdot C_7H_8$
CCDC No.	1979230	1979221	1979229	1979222	1979225	1979220	1979227
Fw	770.5	906.58	864.45	795.26	992.67	886.55	910.52
cryst syst	trigonal	monoclinic	cubic	triclinic	monoclinic	triclinic	monoclinic
space group	$R\bar{3}$	$P2_1/c$	$Pa\bar{3}$	$P\bar{1}$	$P2_1/n$	$P\bar{1}$	C2/c
a (Å)	14.7276(6)	12.8967(5)	20.8114(5)	12.600(8)	19.7163(5)	10.9384(4)	21.2562(12)
b (Å)	14.7276(6)	14.0478(5)	20.8114(5)	18.048(7)	11.1180(3)	12.4594(4)	10.0180(6)
c (Å)	34.9107(17)	25.5457(9)	20.8114(5)	19.885(7)	49.2039(13)	20.0961(7)	39.979(2)
α (°)	90	90	90	65.539(6)	90	93.4220(10)	90
β (°)	90	95.0170(10)	90	88.58(2)	98.2860(10)	92.5660(10)	90.336(2)
γ (°)	90	90	90	79.34(2)	90	114.5710(10)	90
V(Å^3)	120	4610.4(3)	9013.7(6)	4038(3)	10673.2(5)	2479.05(15)	8513.2(9)
Z	6	4	8	4	8	2	8
D_{cald} (g cm^{-3})	1.171	1.306	1.274	1.308	1.236	1.188	1.421
λ (Å), μ (mm^{-1})	0.71073, 0.723	0.71073, 1.799	0.71073, 1.486	0.71073, 1.282	0.71073, 1.560	0.71073, 1.672	0.71073, 1.578
T	123(2)	123(2)	125(2)	100(2)	100(2)	126(2)	100(2)
θ (°)	2.766 – 28.282	2.148 – 32.576	2.188– 30.548	2.1231 – 34.337	2.120 – 27.484	2.221 – 26.731	2.165– 30.600
reflns collected	41541	78598	284172	107105	185917	91591	127265
unique relfns	2944	10275	4622	25564	20031	8380	11429
data/restraint/ parameters	3614/0/146	16776/15/523	4622/0/146	33782/0/871	24509/110/1170	10522/0/494	13087/42/598
R_1, wR_2 (I>2σ (I))	0.0348, 0.0794	0.0465, 0.0753	0.0301, 0.0613	0.0336, 0.0738	0.0426, 0.0838	0.0287, 0.0626	0.0248, 0.0455

[a] Complex **8'** is another solid-state conformer of **8**, which has a η^2-(N-C$_{ipso}$) interaction between the NPh group and the La center.

^{31}P, ^{1}H, and ^{13}C NMR Characterization Spectra of Synthesized Complexes

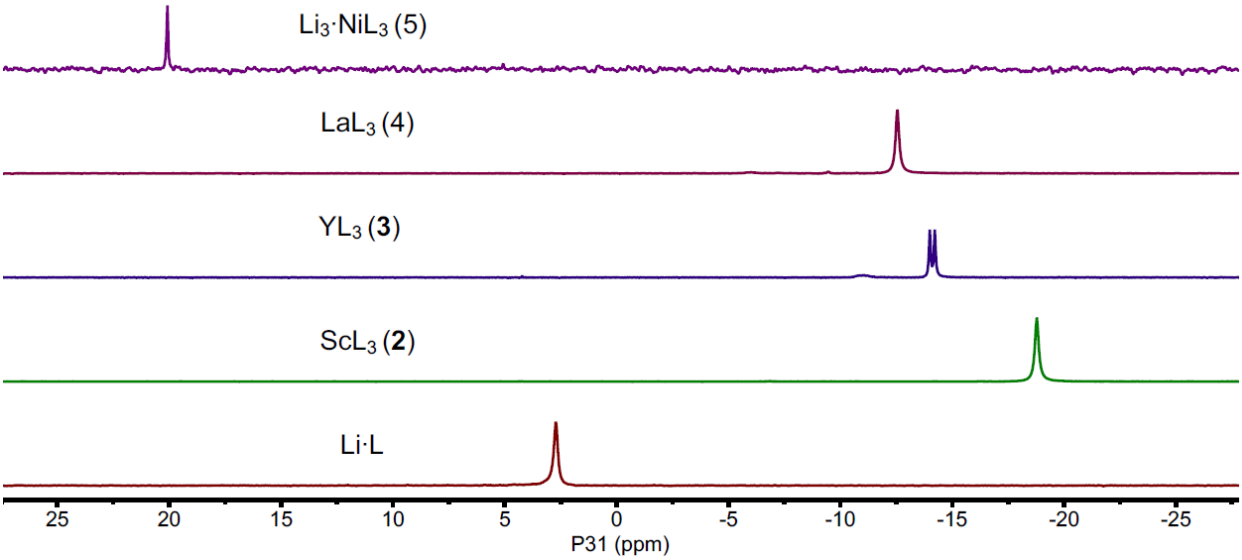

Figure S1. $^{31}P\{^{1}H\}$ NMR (162 MHz, C_6D_6) spectra of **^{i}Pr$_2$PCH$_2$NLiPh** and monometallic complexes **2–5**.

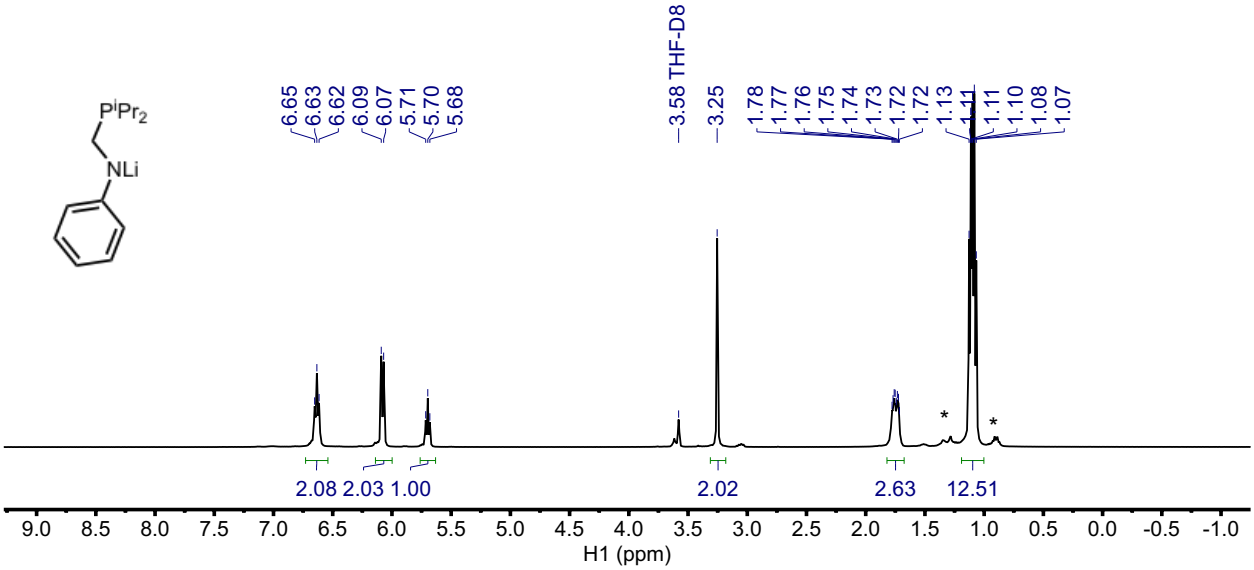

Figure S2. $^1H\{^{31}P\}$ NMR (400 MHz, THF–d_8) spectrum of **Li(iPr_2PCH_2NPh)**. Hexanes solvent is marked by an asterisk (*).

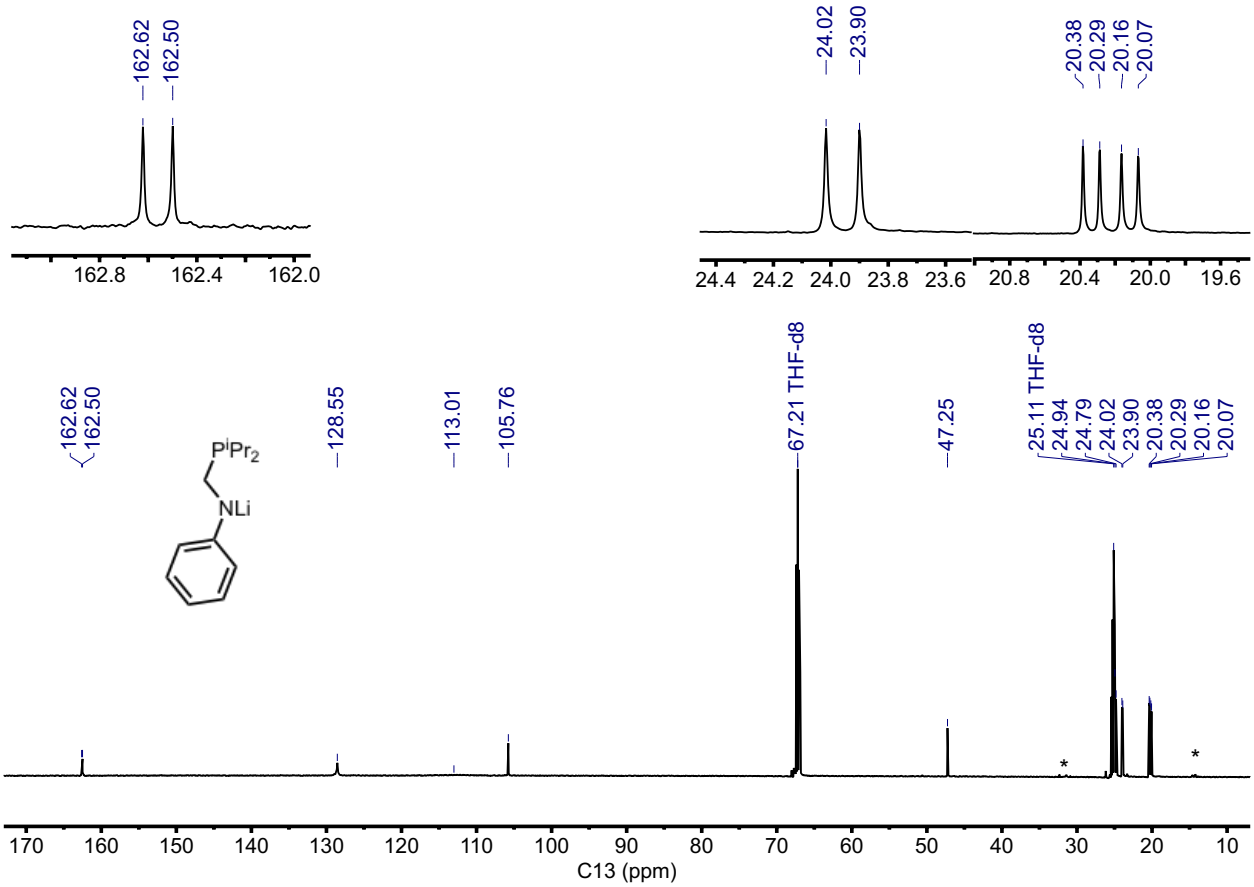

Figure S3. $^{13}C\{^1H\}$ NMR (126 MHz, THF–d_8) spectrum of **Li(iPr_2PCH_2NPh)**. Hexanes solvent is marked by an asterisk (*).

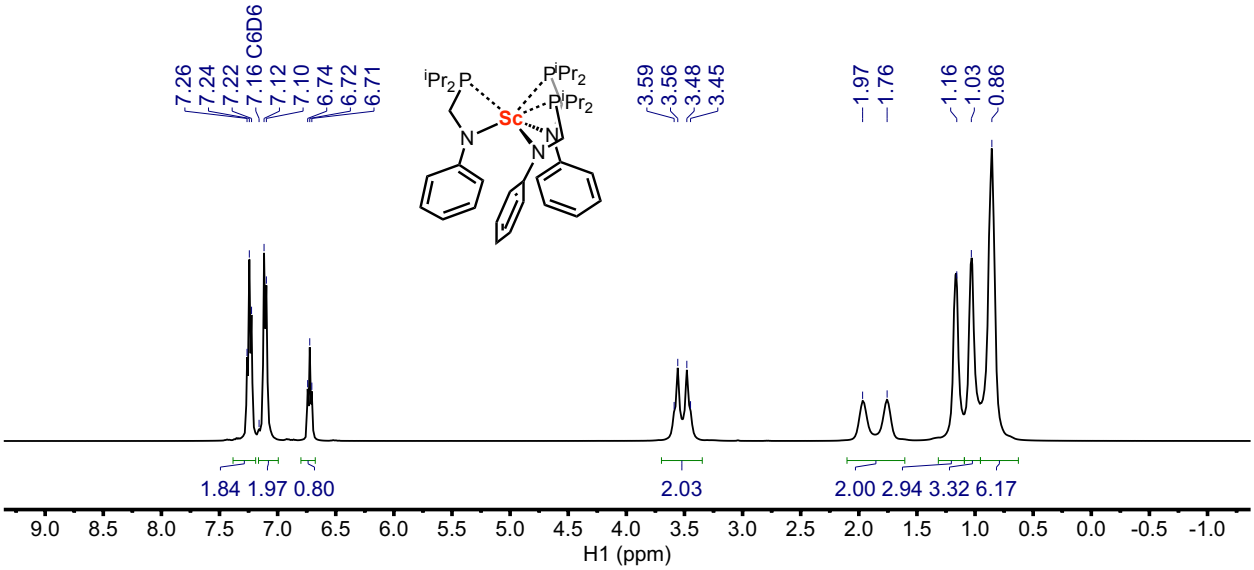

Figure S4. $^{1}H\{^{31}P\}$ NMR (400 MHz, C_6D_6) spectrum of $Sc(^{i}Pr_2PCH_2NPh)_3$ (**2**).

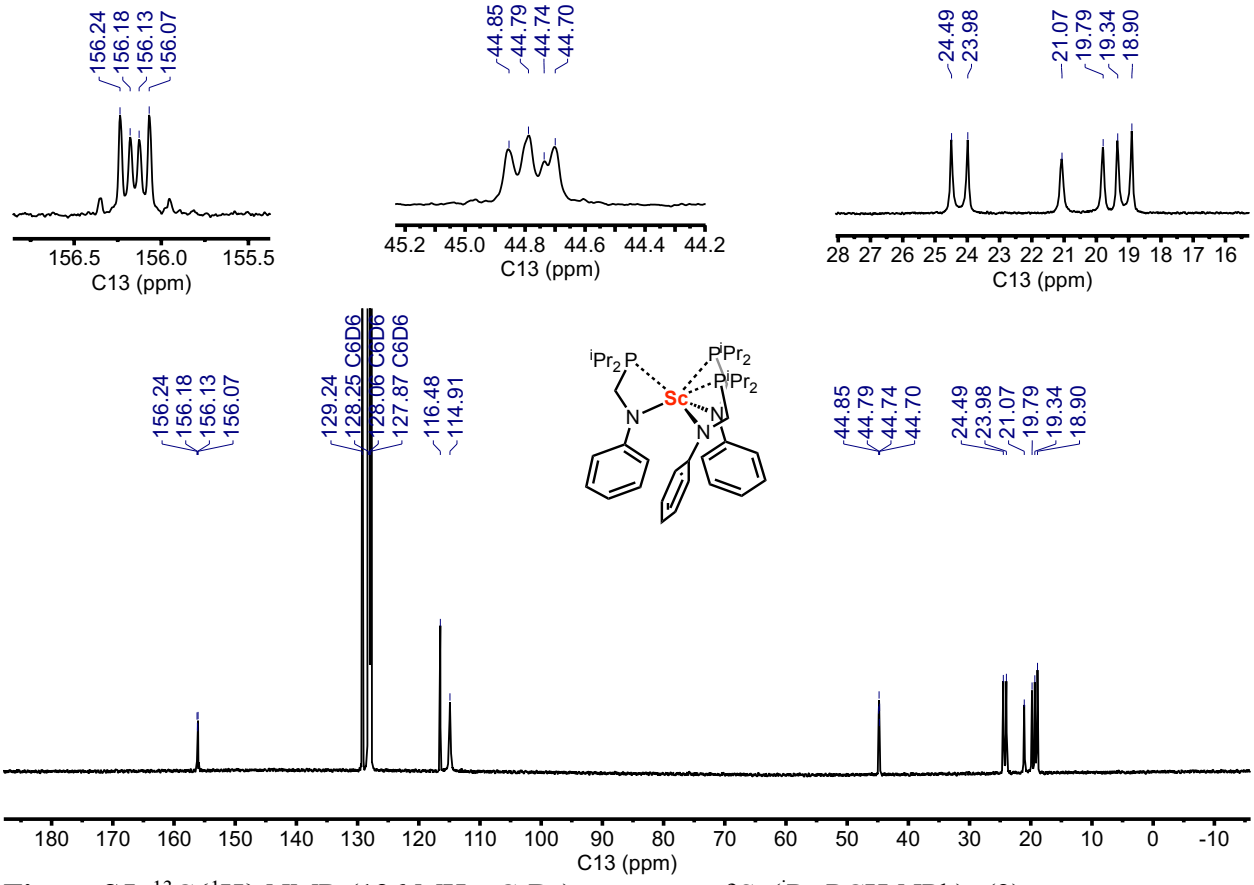

Figure S5. $^{13}C\{^{1}H\}$ NMR (126 MHz, C_6D_6) spectrum of $Sc(^{i}Pr_2PCH_2NPh)_3$ (**2**).

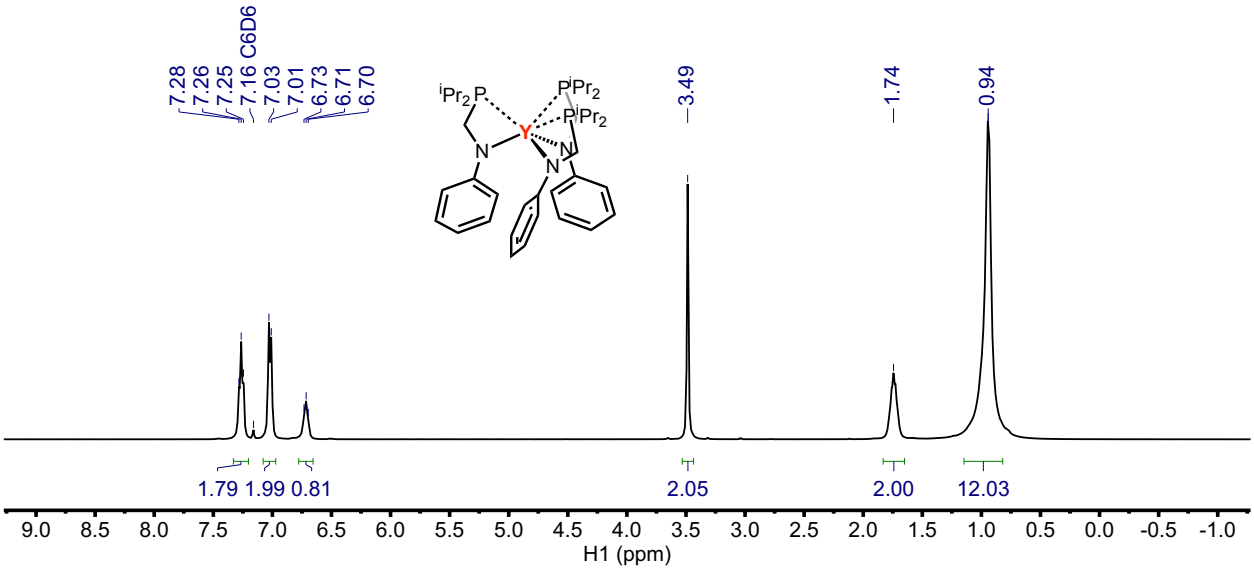

Figure S6. $^{1}H\{^{31}P\}$ NMR (400 MHz, C_6D_6) spectrum of $Y(^{i}Pr_2PCH_2NPh)_3$ (**3**).

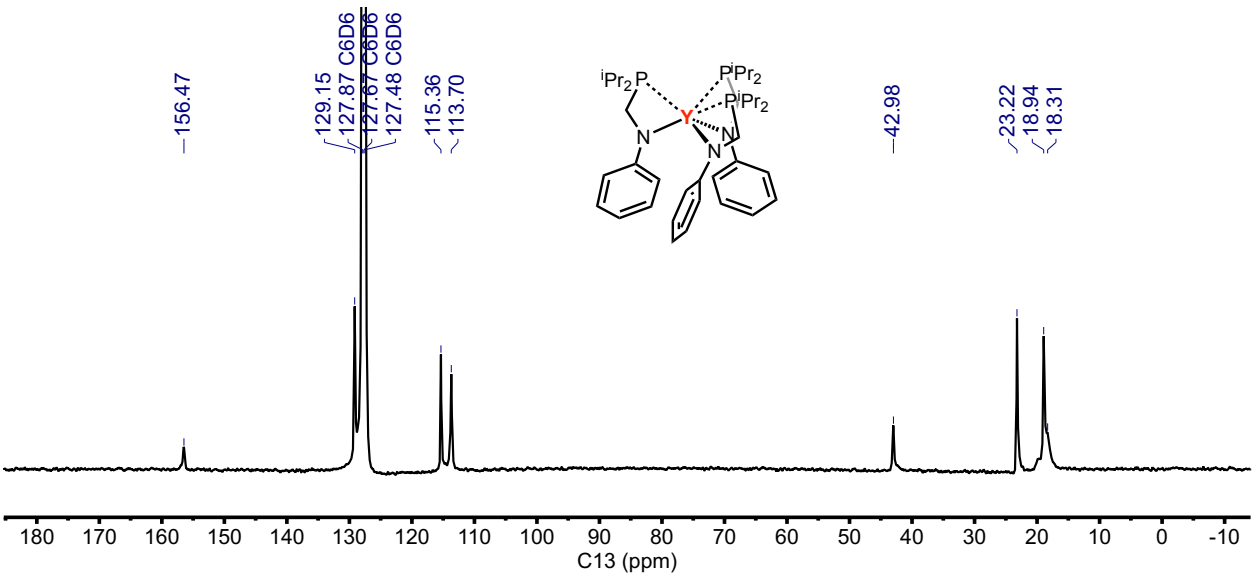

Figure S7. $^{13}C\{^{1}H\}$ NMR (126 MHz, C_6D_6) spectrum of $Y(^{i}Pr_2PCH_2NPh)_3$ (**3**).

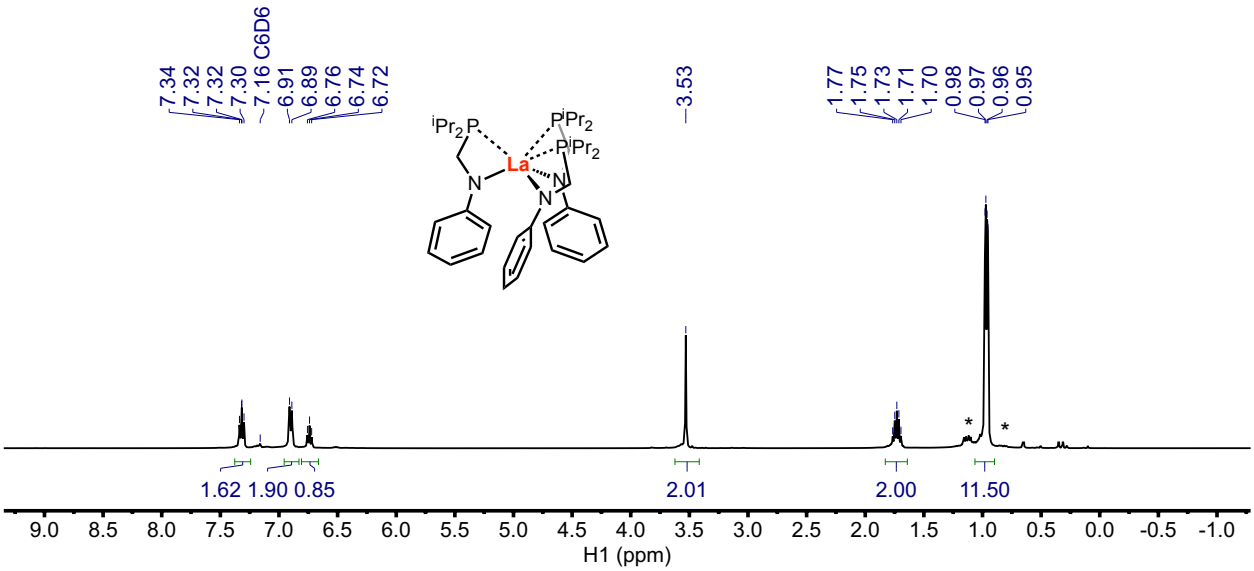

Figure S8. $^{1}H\{^{31}P\}$ NMR (400 MHz, C_6D_6) spectrum of La($^{i}Pr_2PCH_2NPh)_3$ (**4**). Hexanes solvent is marked by an asterisk (*).

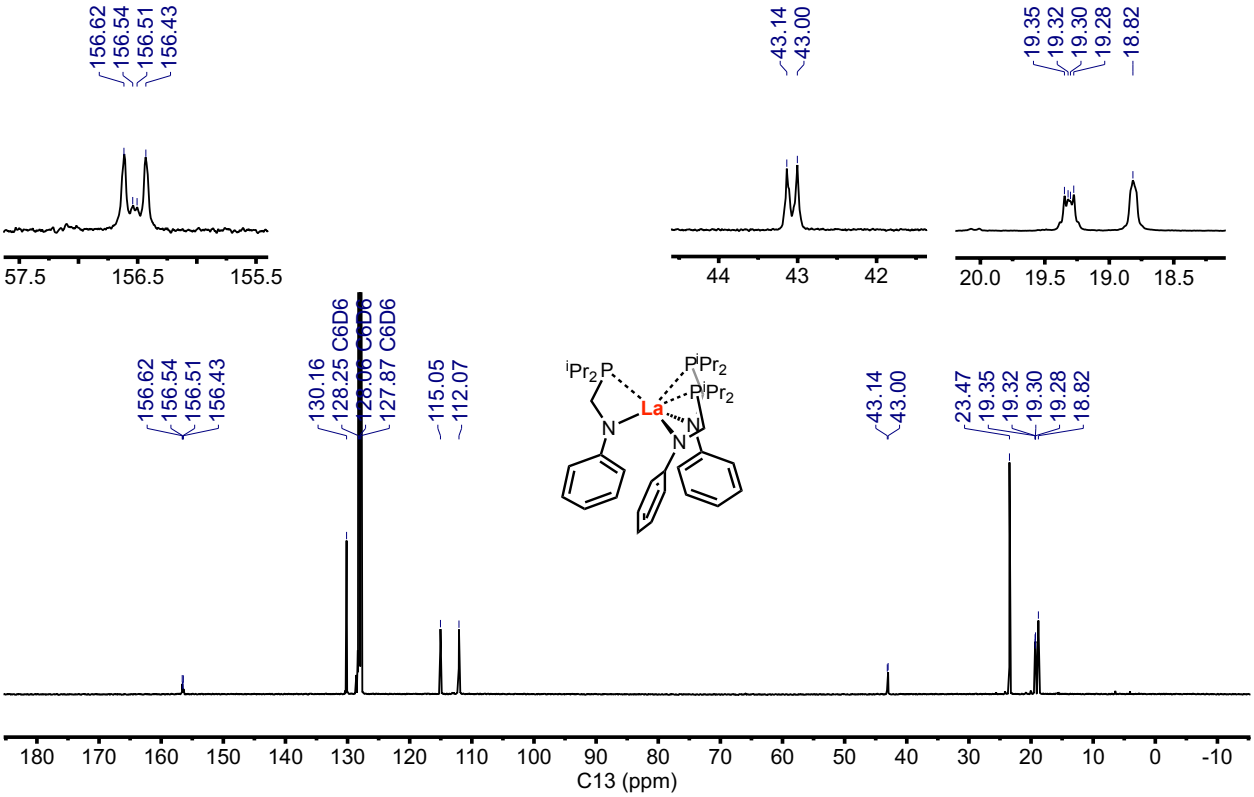

Figure S9. $^{13}C\{^{1}H\}$ NMR (126 MHz, C_6D_6) spectrum of La($^{i}Pr_2PCH_2NPh)_3$ (**4**).

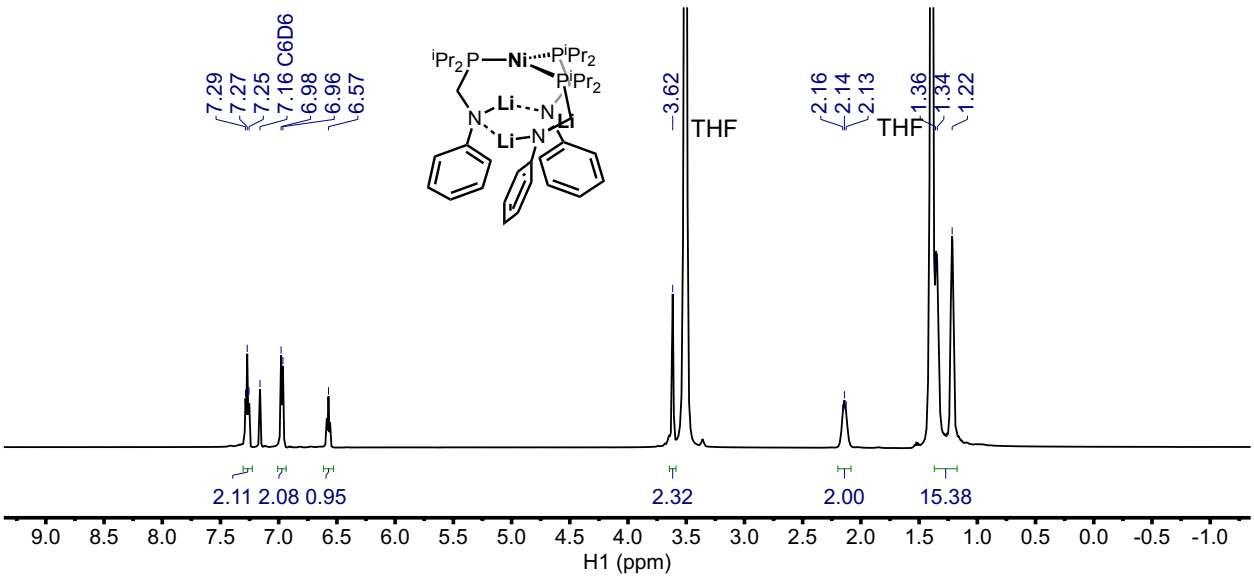

Figure S10. $^{1}H\{^{31}P\}$ NMR (400 MHz, C_6D_6+THF) spectrum of $Li_3{\cdot}Ni(^{i}Pr_2PCH_2NPh)_3$ (**5**).

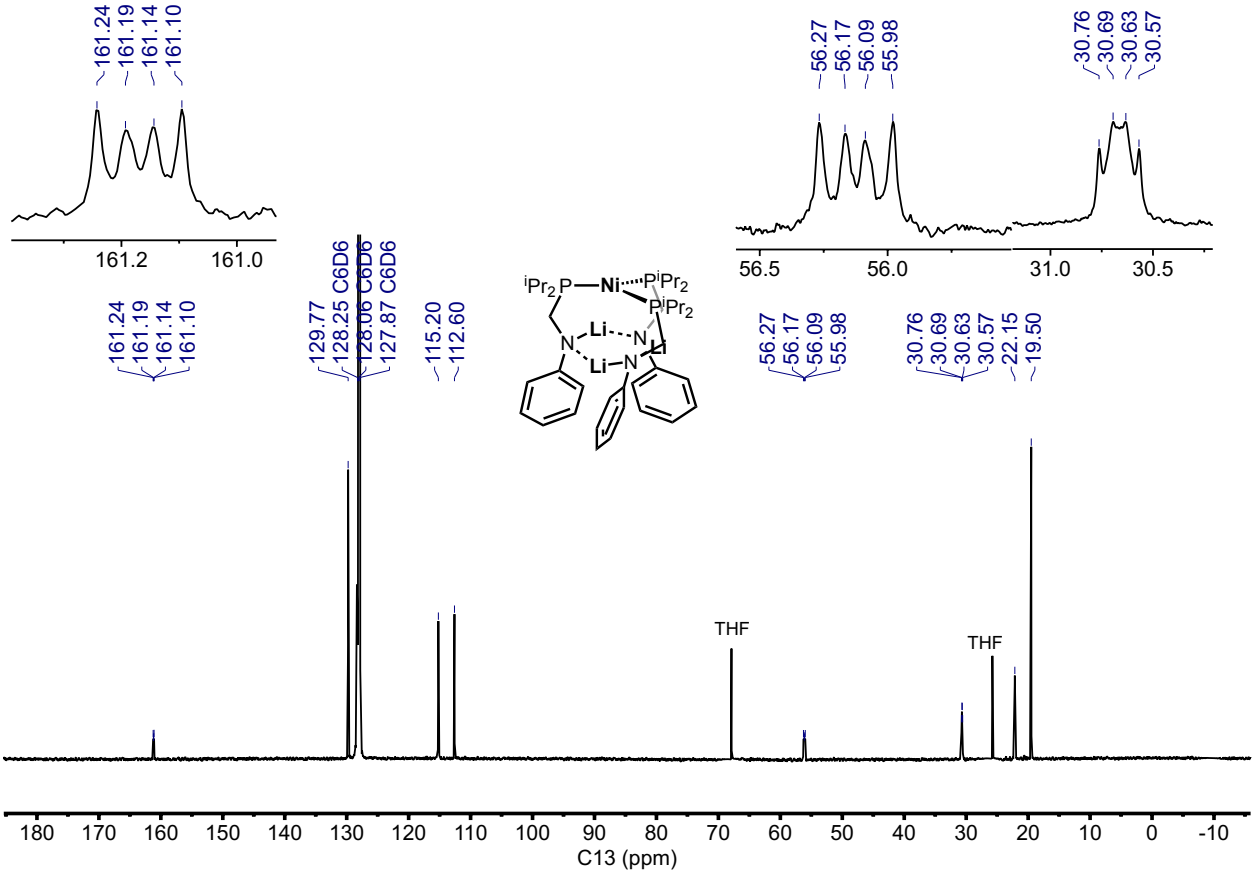

Figure S11. $^{13}C\{^{1}H\}$ NMR (126 MHz, C_6D_6 +THF) spectrum of $Li_3{\cdot}Ni(^{i}Pr_2PCH_2NPh)_3$ (**5**).

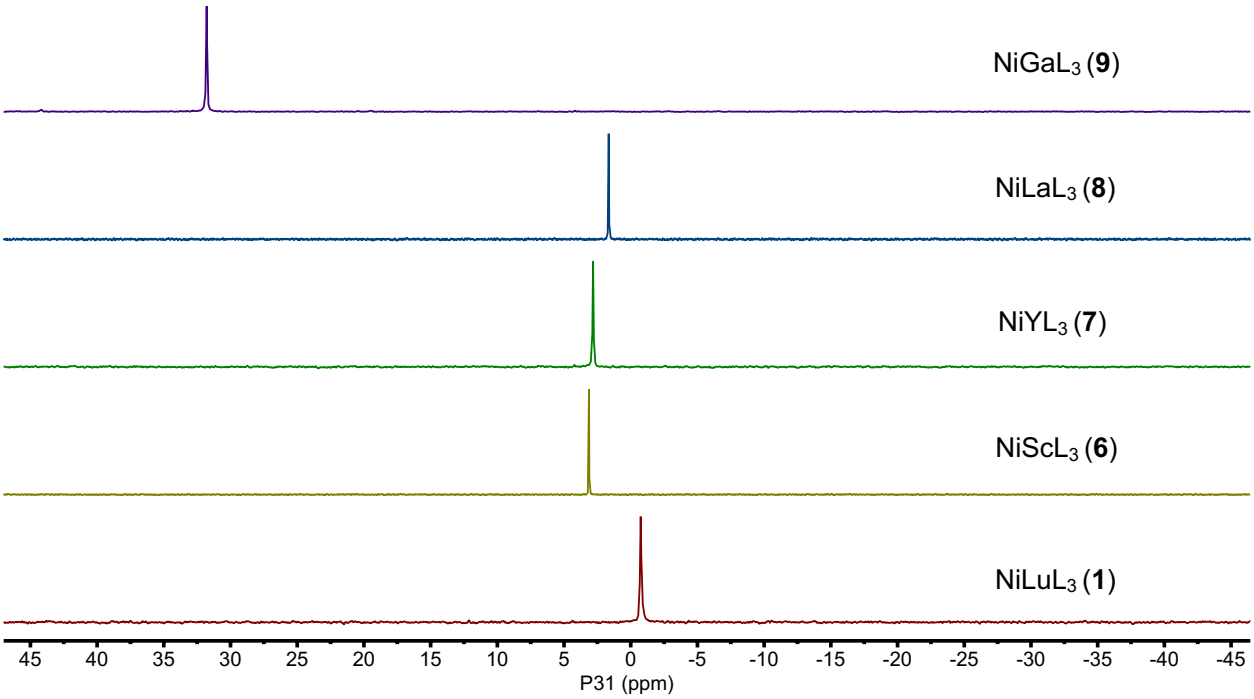

Figure S12. $^{31}P\{^{1}H\}$ NMR (162 MHz, toluene–d_8 (**6**–**8**) or C_6D_6 (**9**)) spectra of heterobimetallic complexes**.**

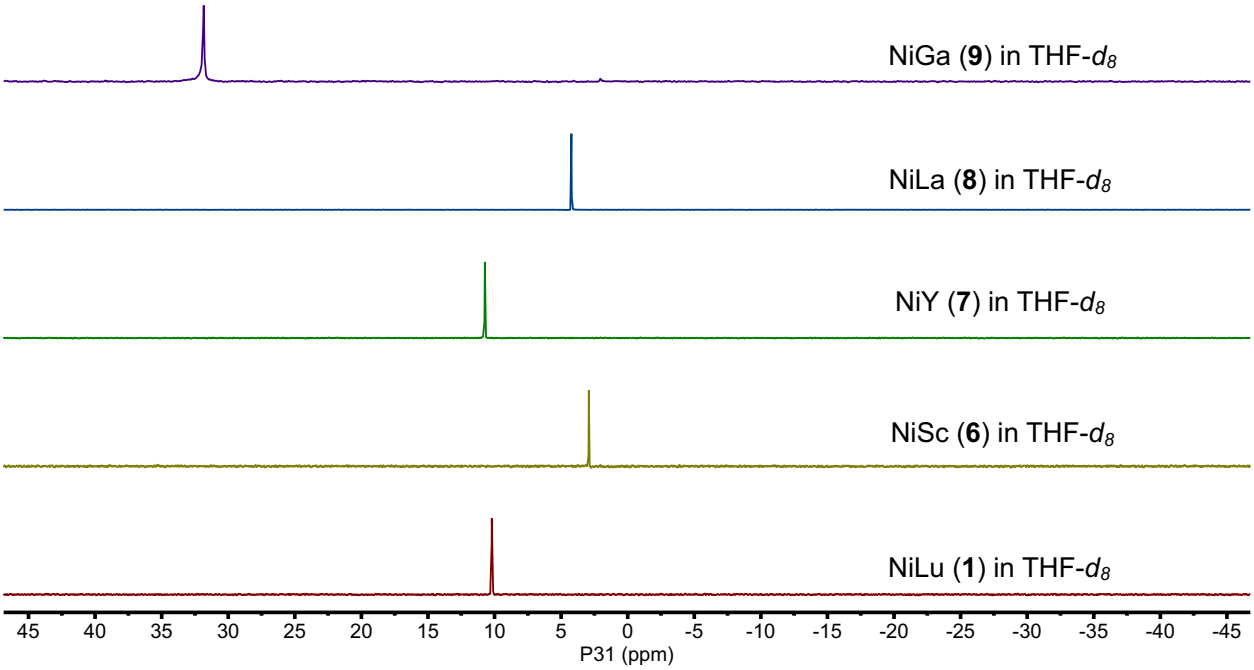

Figure S13. $^{31}P\{^{1}H\}$ NMR (162 MHz, THF–d_8) spectra of complexes **6**–**8** in coordinating solvent THF–d_8.

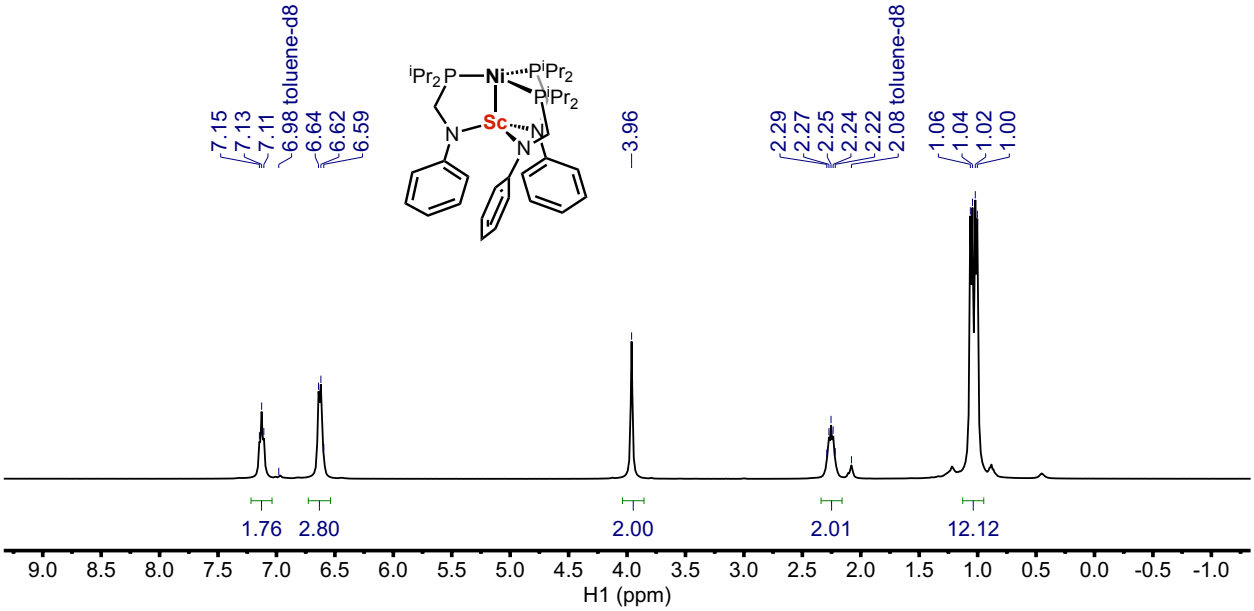

Figure S14. $^{1}H\{^{31}P\}$ NMR (400 MHz, toluene–d_8) spectrum of NiSc($^{i}Pr_2PCH_2NPh)_3$ (**6**).

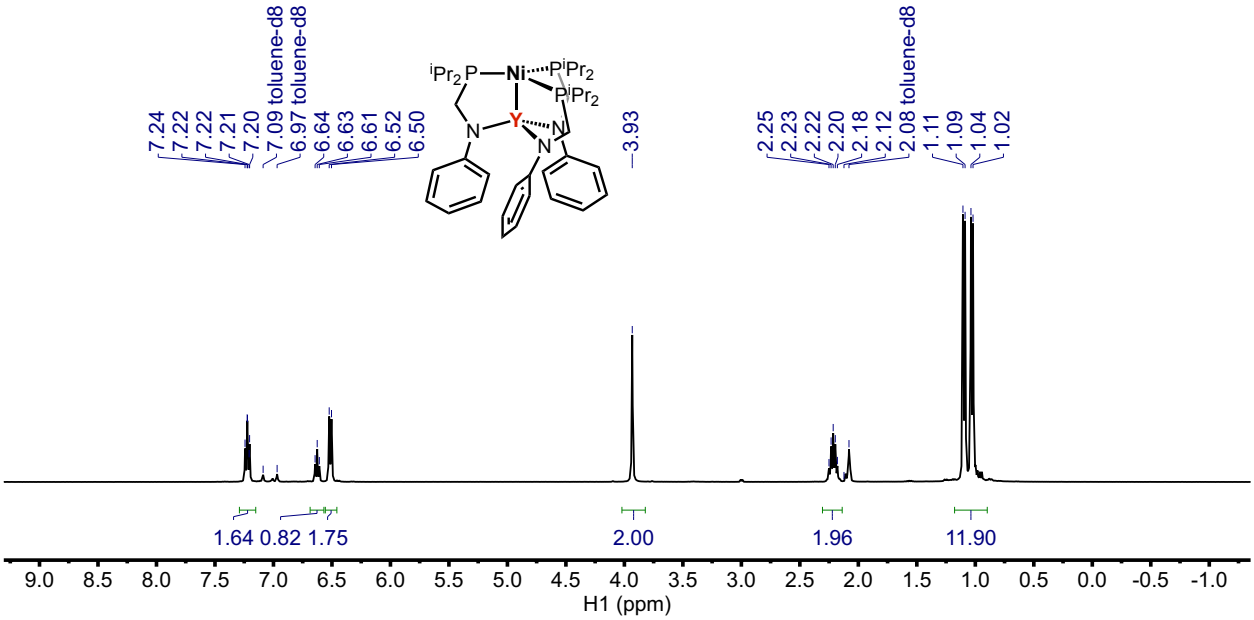

Figure S15. $^{1}H\{^{31}P\}$ NMR (400 MHz, toluene–d_8) spectrum of NiY($^{i}Pr_2PCH_2NPh)_3$ (**7**).

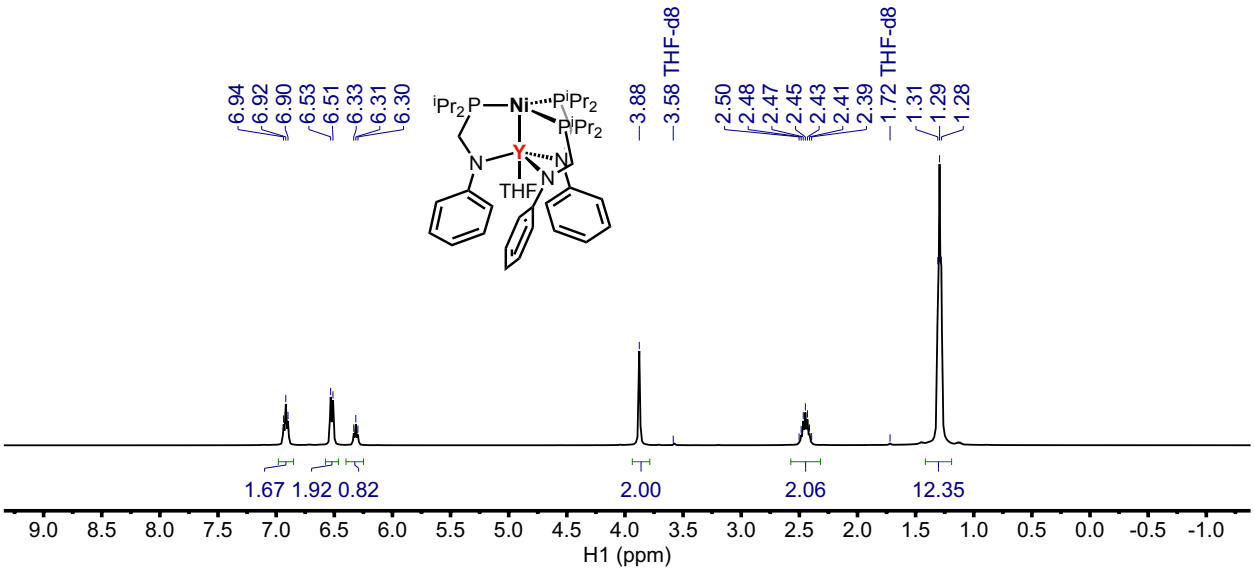

Figure S16. $^{1}H\{^{31}P\}$ NMR (400 MHz, THF–d_8) spectrum of **7**–**THF**.

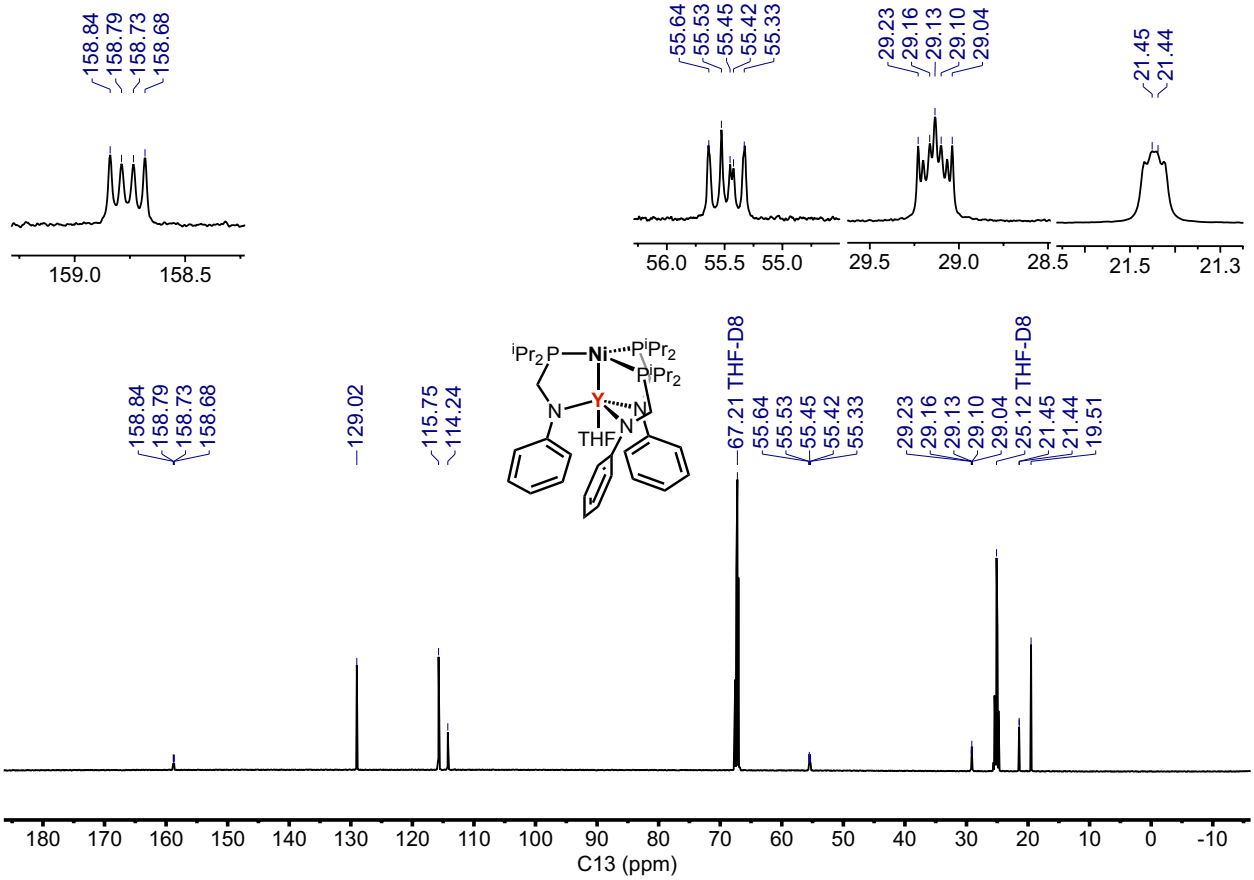

Figure S17. $^{13}C\{^{1}H\}$ NMR (126 MHz, THF–d_8) spectrum of **7**–**THF**.

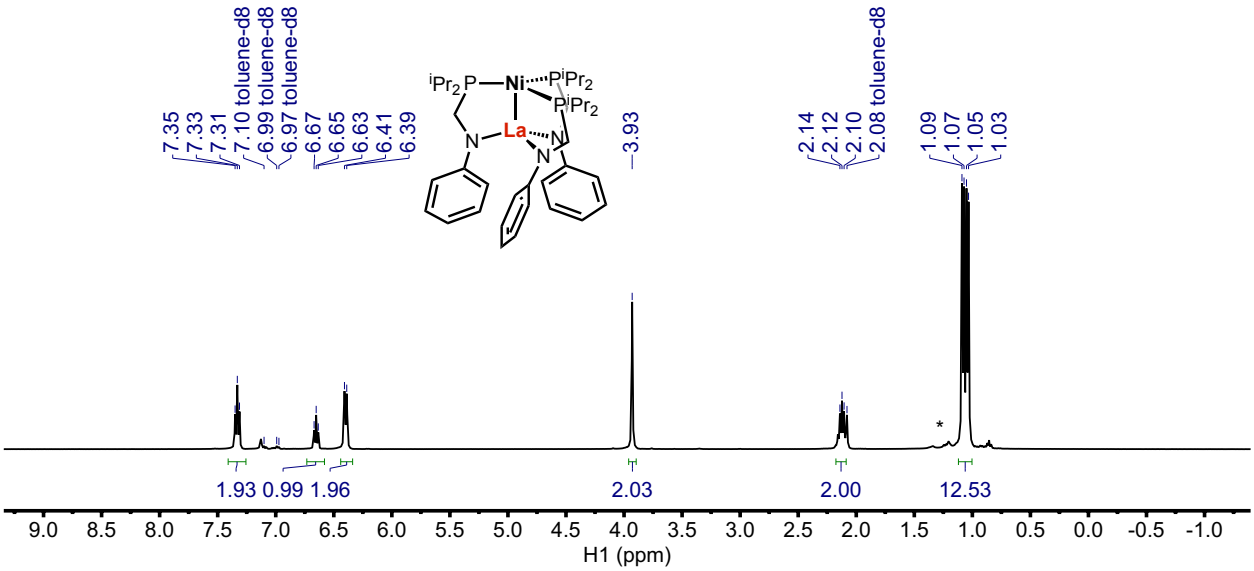

Figure S18. $^{1}H\{^{31}P\}$ NMR (400 MHz, toluene–d_8) spectrum of NiLa($^{i}Pr_2PCH_2NPh)_3$ (**8**). Hexanes solvent is marked by an asterisk (*).

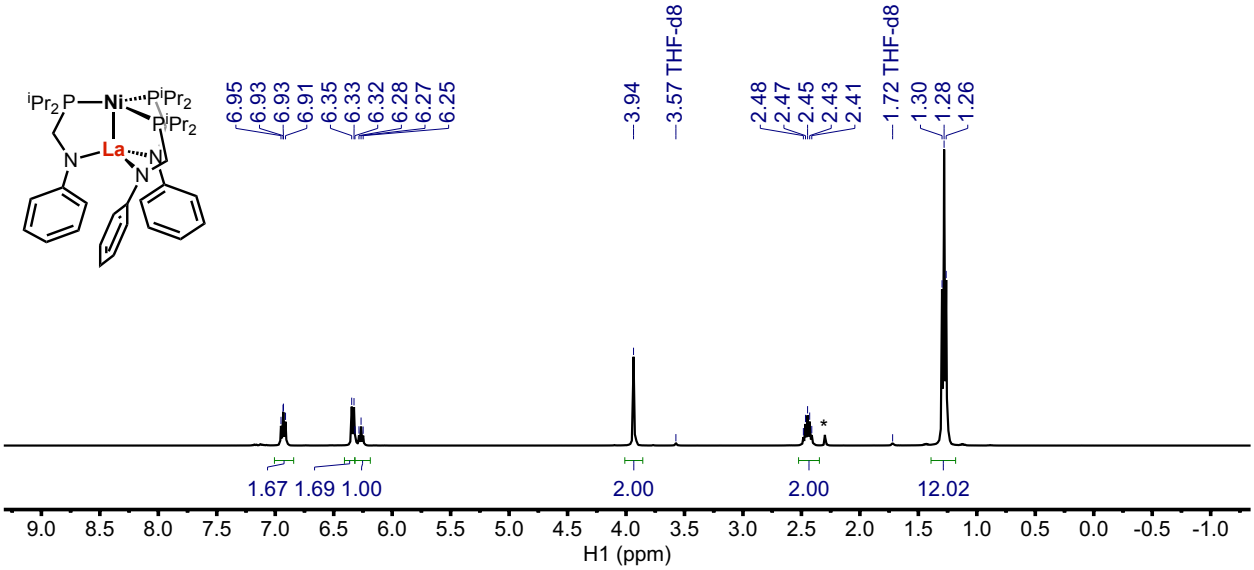

Figure S19. $^{1}H\{^{31}P\}$ NMR (400 MHz, THF–d_8) spectrum of **8**. Toluene solvent is marked by an asterisk (*).

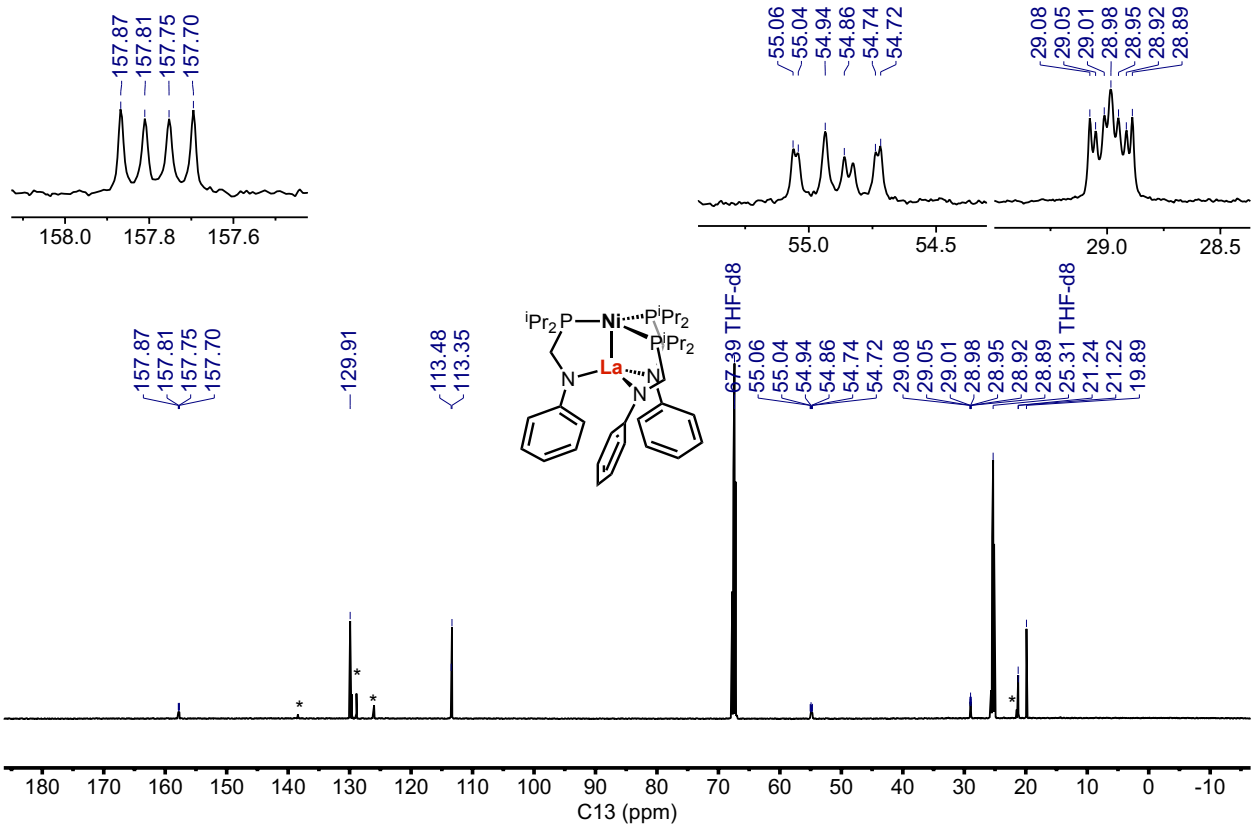

Figure S20. $^{13}C\{^{1}H\}$ NMR (126 MHz, THF–d_8) spectrum of **8**. Toluene solvent is marked by an asterisk (*).

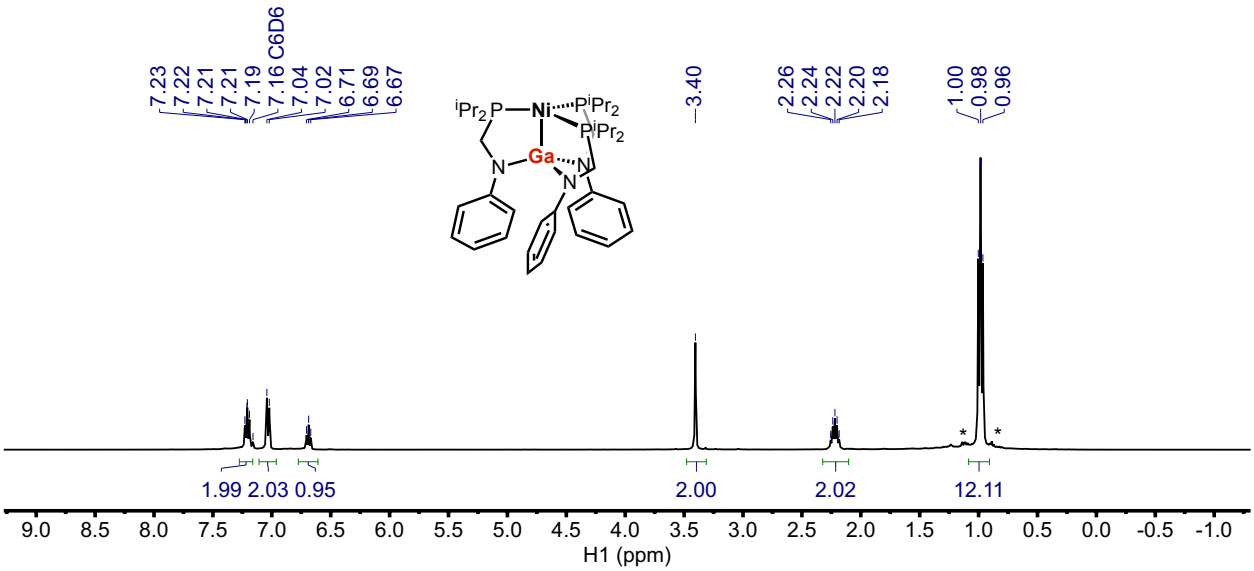

Figure S21. $^{1}H\{^{31}P\}$ NMR (400 MHz, C_6D_6) spectrum of NiGa($^{i}Pr_2PCH_2NPh)_3$ (**9**). Hexanes is marked by an asterisk (*).

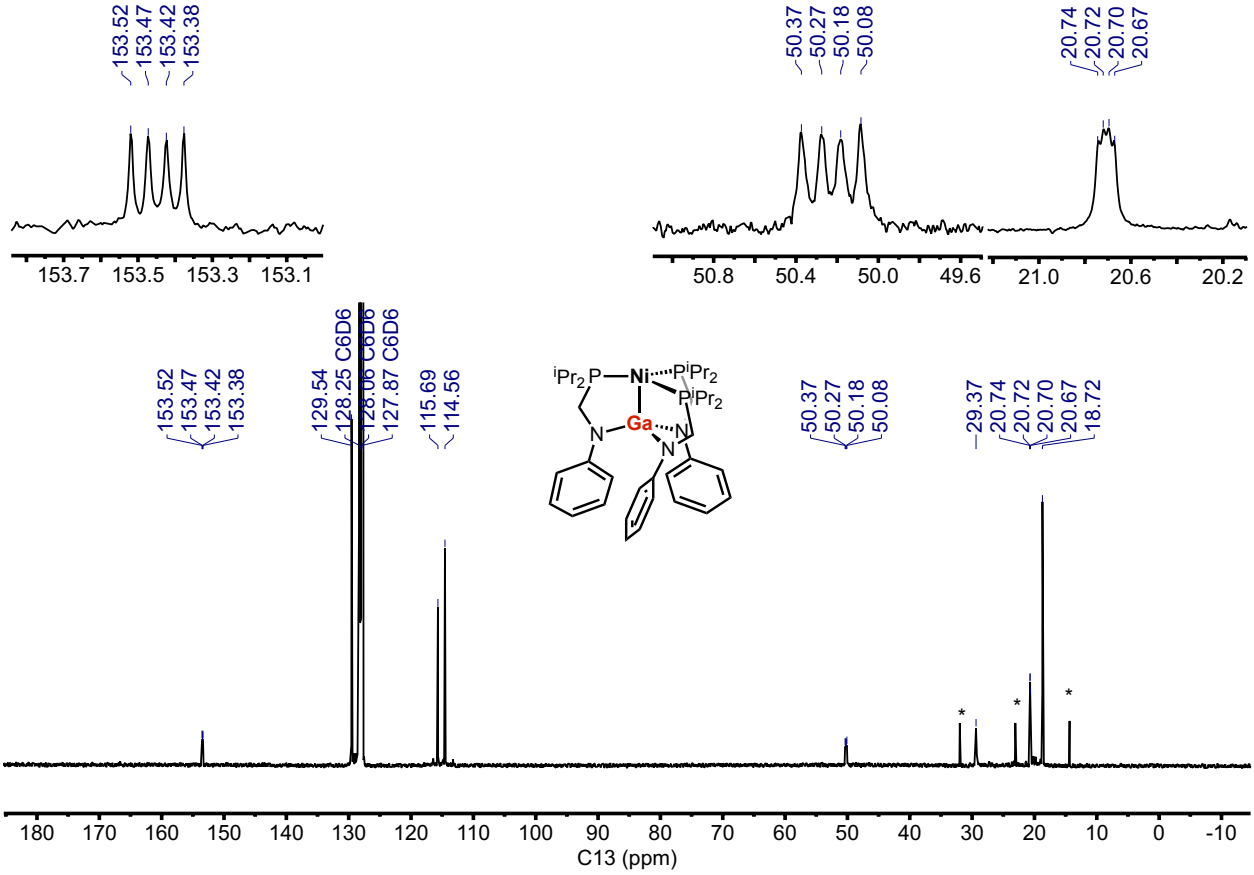

Figure S22. $^{13}C\{^{1}H\}$ NMR (126 MHz, C_6D_6) spectrum of NiGa($^{i}Pr_2PCH_2NPh)_3$ (**9**). Hexanes is marked by an asterisk (*).

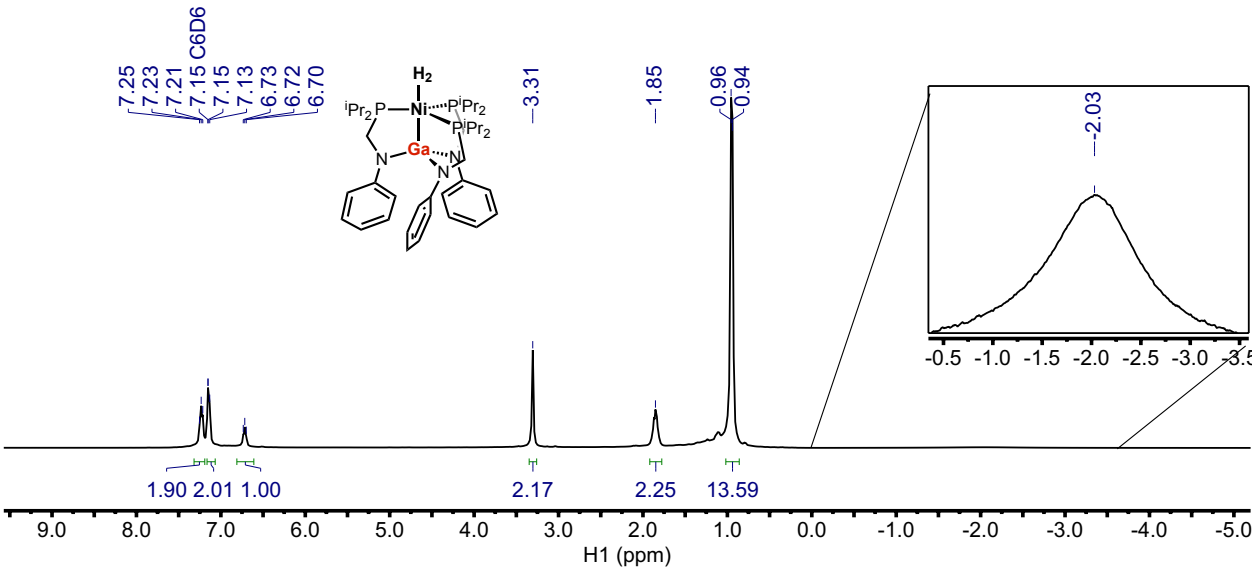

Figure S23. ^{1}H NMR (400 MHz, C_6D_6) spectrum of *in situ* generated **9**–H_2 from exposing NiGa **9** to 1 atm of H_2.

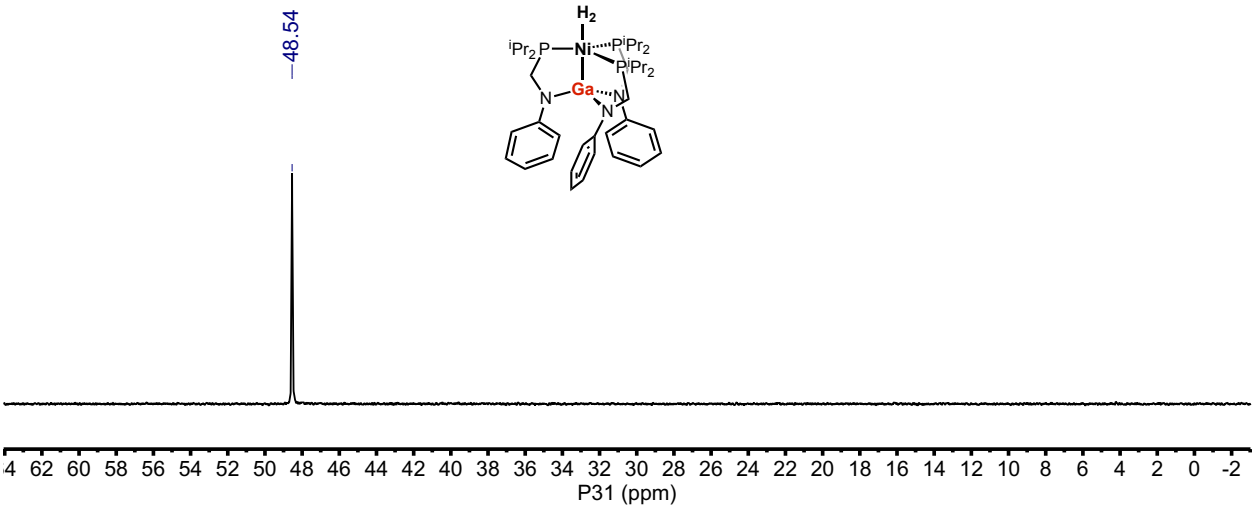

Figure S24. ^{31}P{^{1}H} NMR (162 MHz, C_6D_6) spectrum of *in situ* generated **9**–H_2 from exposing NiGa **9** to 1 atm of H_2.

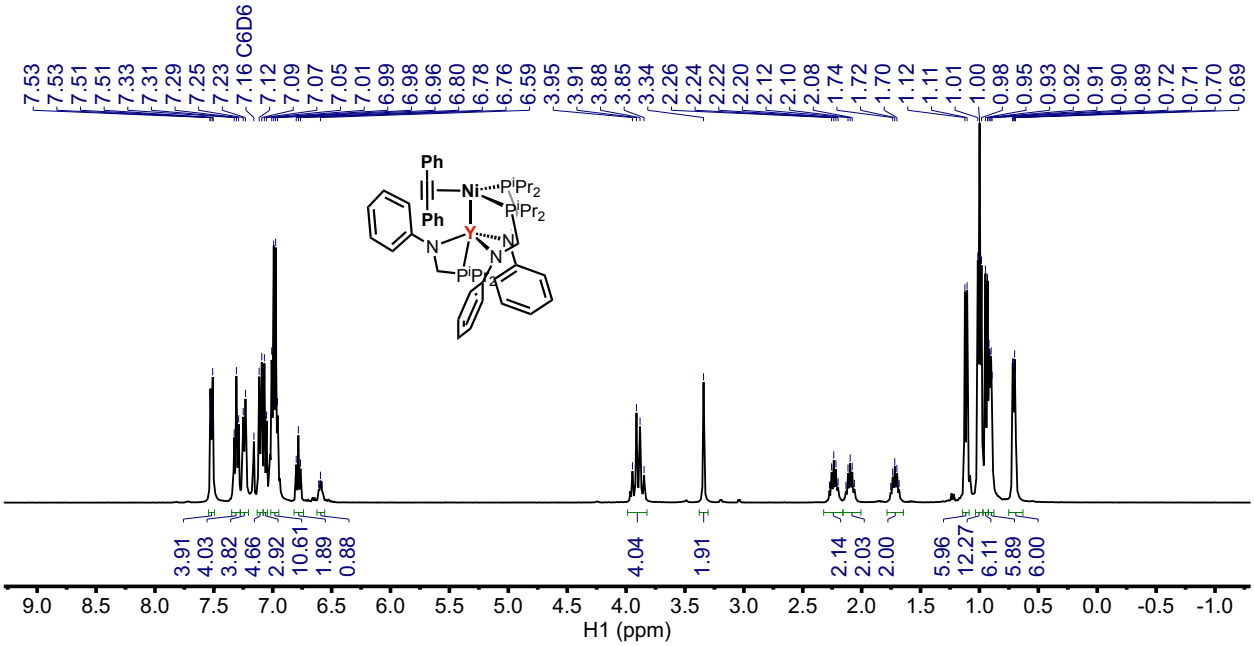

Figure S25. $^{1}H\{^{31}P\}$ NMR (400 MHz, C_6D_6) spectrum of *in situ* generated **7**–DPA from exposing NiY **7** to 5 equiv. of diphenylacetylene.

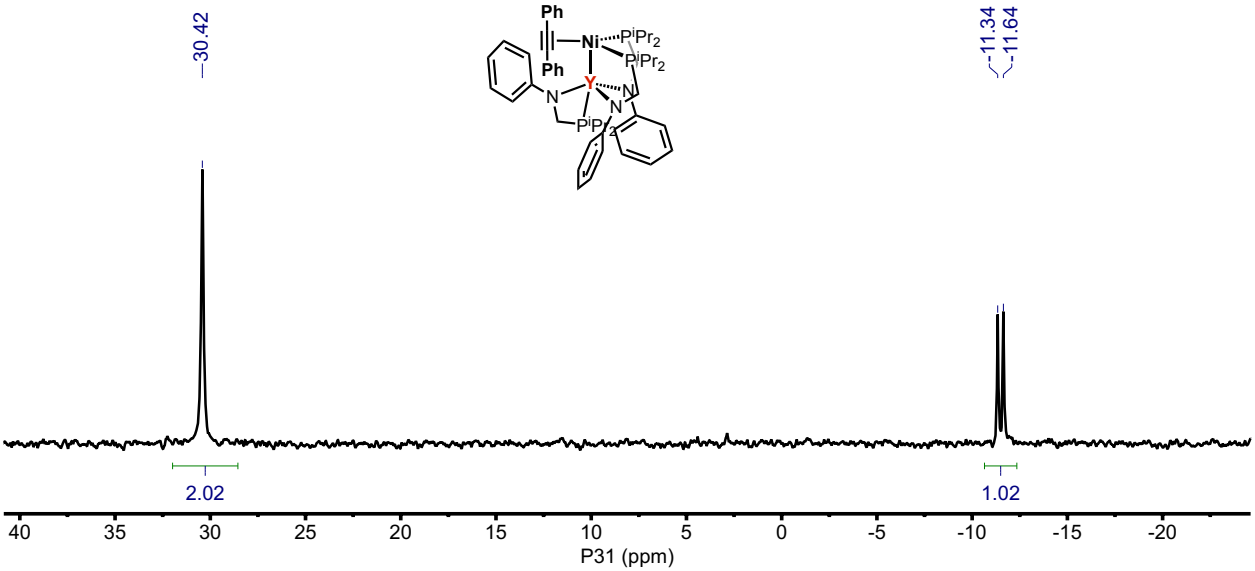

Figure S26. $^{31}P\{^{1}H\}$ NMR (162 MHz, C_6D_6) spectrum of *in situ* generated **7**–DPA from exposing NiY **7** to 5 equiv. of diphenylacetylene.

Cyclic Voltammetry Studies of Heterobimetallic Complexes 6–9

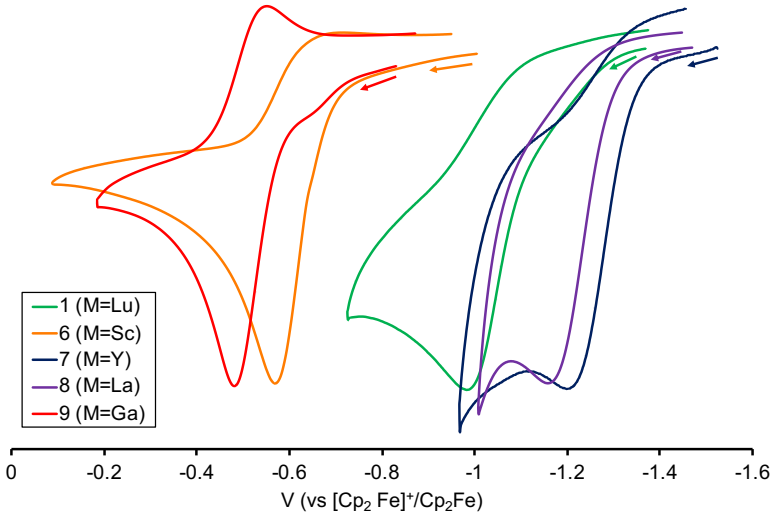

Figure S27. Cyclic voltammogram overlay of the $NiML_3$ oxidation event for complexes **1** and **6**–**9** in 0.1 M [^{n}Pr$_4$N][BAr$^F_4$] in 1,2-difluorobenzene under Ar at 100mV/s.

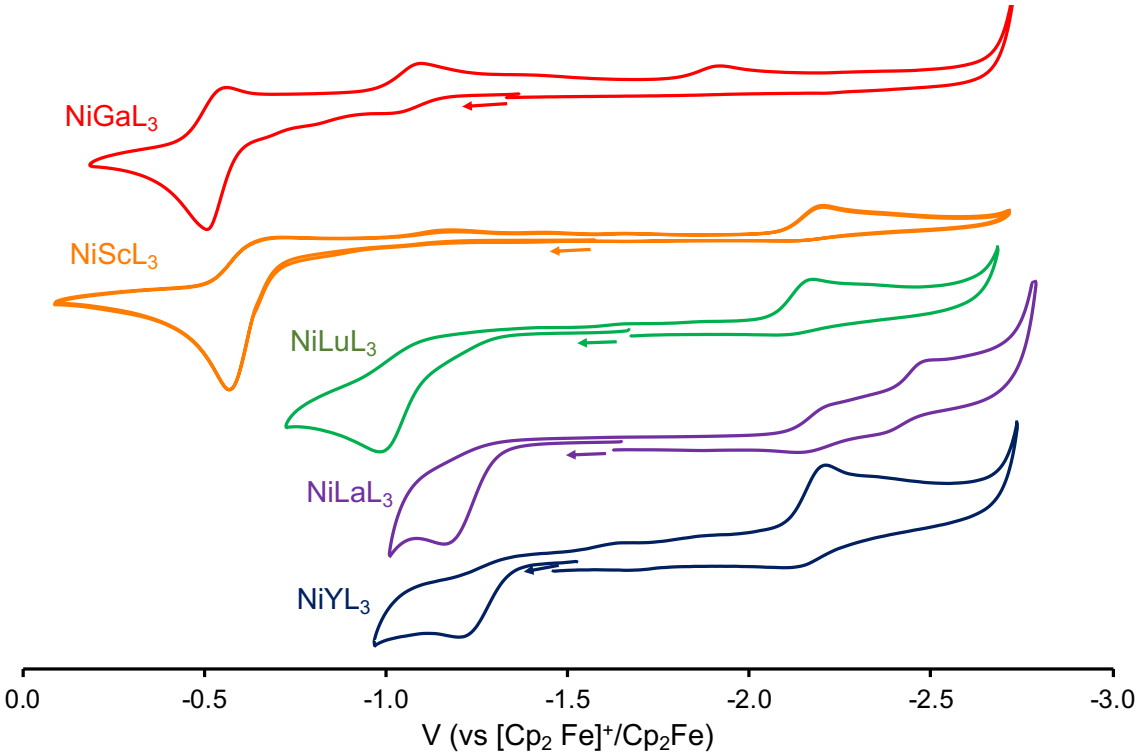

Figure S28. Cyclic voltammogram overlay of Ni–M complexes **1** and **6**–**9** in 0.1 M [^{n}Pr$_4$N][BAr$^F_4$] in 1,2-difluorobenzene under Ar at 100mV/s.

Table S3. R^2_{adj} correlation values between E_{pa} (V) of $NiML_3$ complexes (1 and 6–9) and various M(III) parameters.

$NiML_3$	E_{pa} (V)	M^{3+} Ionic Radii (Å)[a]	Pyykko Covalent Radii (Å)[b]	Pauling Metallic Radii (Å)[c]	Codero Covalent Radii (Å)[d]	Pauling Electronegativity [e]	p*K*a of $M(H_2O)_n^{3+}$ ion[f]	Charge Density (mm^3)
6 (M=Sc)	-0.57	0.745	1.48	1.429	1.7	1.36	5.11	277
7 (M=Y)	-1.23	0.9	1.63	1.616	1.9	1.22	8.43	157
1 (M=Lu)	-1.01	0.861	1.62	1.557	1.87	1.27	7.9	180
8 (M=La)	-1.17	1.032	1.8	1.69	2.07	1.1	9.06	104
9 (M=Ga)	-0.48	0.62	1.24	1.245	1.22	1.81	2.95	481
R^2_{adj}		0.77	0.70	0.83	0.66	0.60	**0.91**	0.73

[a]Ionic radii for six-coordinate species. Ref. 11, [b]single–bond radii for a coordination number of three. Ref. 12&13, [c]Ref. 14, [d]Ref. 15, [e]Ref. 16, [f]Ref. 10.

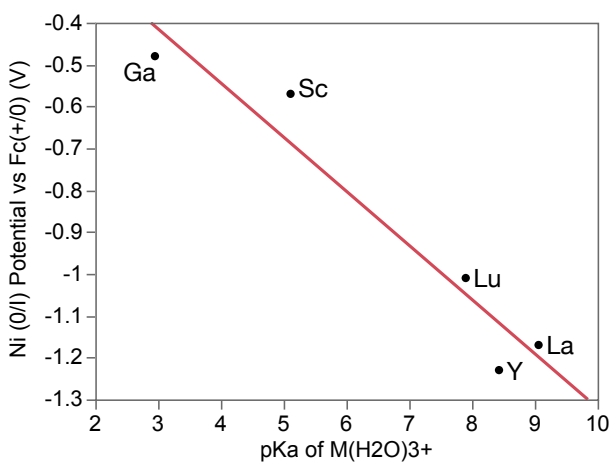

Linear Fit

Ni (0/I) Potential vs Fc(+/0) (V) = -0.026737 - 0.1293367*pKa of M(H2O)3+

Summary of Fit

RSquare	0.928919
RSquare Adj	0.905225
Root Mean Square Error	0.10652
Mean of Response	-0.892
Observations (or Sum Wgts)	5

Analysis of Variance

Source	DF	Sum of Squares	Mean Square	F Ratio
Model	1	0.44484076	0.444841	39.2054
Error	3	0.03403924	0.011346	Prob > F
C. Total	4	0.47888000		0.0082*

Parameter Estimates

Term	Estimate	Std Error	t Ratio	Prob>|t|
Intercept	-0.026737	0.14617	-0.18	0.8665
pKa of M(H2O)3+	-0.129337	0.020656	-6.26	0.0082*

Figure S29. Plot of Ni(I/0) anodic peak potentials (E_{pa}) versus pK_a of $[M(H_2O)_6]^{3+}$ ion for complexes **1** and **6**–**8**.

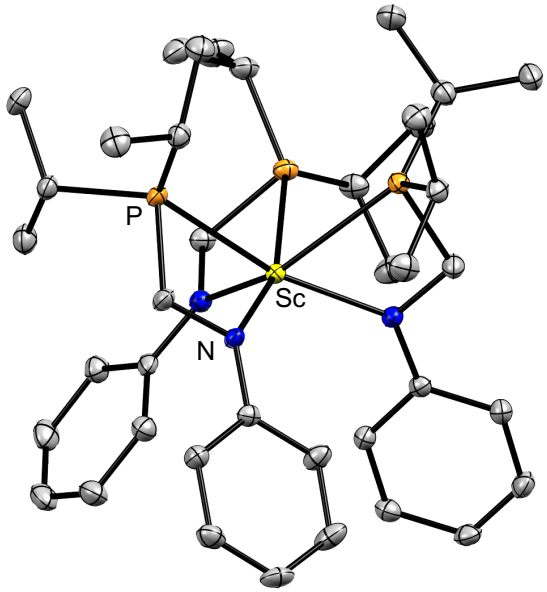

Figure S30. Molecular structure of **2** shown at 50% thermal ellipsoid probability. Hydrogen atoms and non-coordinating solvent molecules have been omitted for clarity. Atom colors: Sc, yellow; P, orange; N, blue; O, red; C, gray.

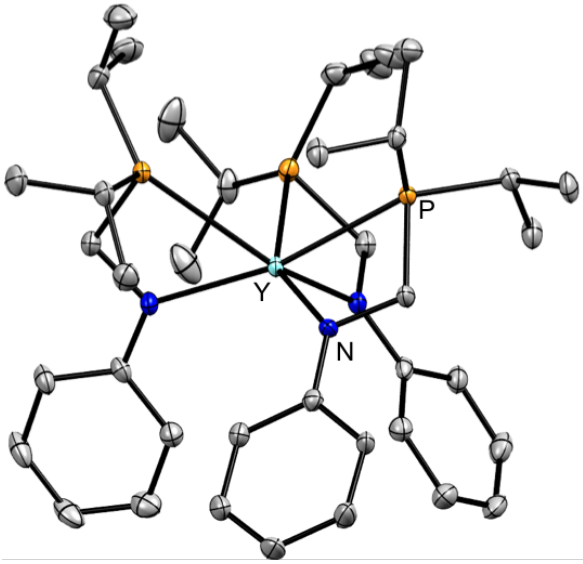

Figure S31. Molecular structure of **3** shown at 50% thermal ellipsoid probability. Hydrogen atoms and non-coordinating solvent molecules have been omitted for clarity. Atom colors: Y, light blue; P, orange; N, blue; O, red; C, gray.

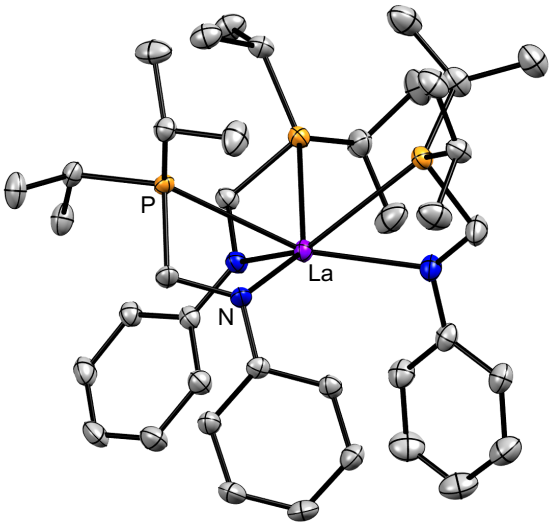

Figure S32. Molecular structure of **4** shown at 50% thermal ellipsoid probability. Hydrogen atoms and non-coordinating solvent molecules have been omitted for clarity. Atom colors: La, purple; P, orange; N, blue; O, red; C, gray.

Table S4. **Full table of Geometrical Parameters, Including Bond Lengths (Å) and Angles (deg) for Monometallic Complexes 2–4.**

	2 (ScL_3)	**3 (YL_3)**	**4 (LaL_3)**
	2.7807(7)	2.9595(7)	3.1829(4)
M–P	2.8465(6)	2.9644(7)	3.2414(4)
	2.8674(7)	3.0053(7)	3.2028(4)
avg. M–P	**2.8315(4)**	**2.9764(4)**	**3.2090(2)**
	2.1063(14)	2.258(2)	2.4181(13)
M–N	2.1165(15)	2.273(2)	2.3991(13)
	2.1064(14)	2.282(2)	2.4314(13)
avg. M–N	**2.1097(8)**	**2.271(1)**	**2.4162(8)**
	92.595(19)	97.15(2)	92.642(10)
P–M–P	87.15(2)	93.19(2)	99.006(11)
	102.38(2)	100.38(2)	89.605(11)
Σ(P–M–P)	**282.13(3)**	**290.72(3)**	**281.25(2)**
	105.01(5)	114.38(8)	112.31(4)
N–M–N	110.17(6)	101.95(7)	119.22(4)
	108.28(5)	111.00(7)	116.70(4)
Σ(N–M–N)	**324.46(9)**	**327.33(13)**	**348.22(7)**

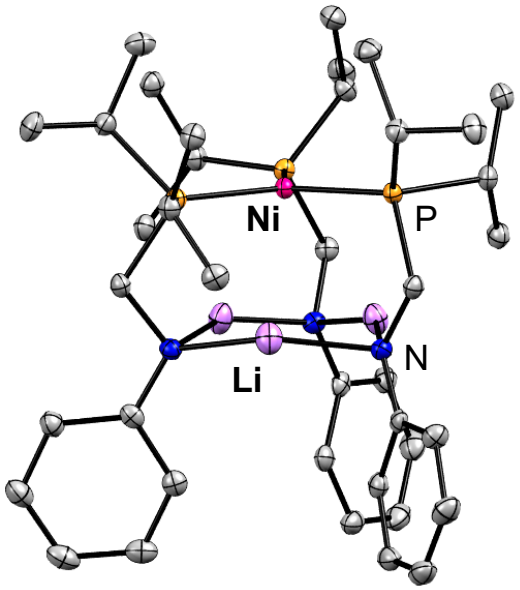

avg. Ni–M (Å):	2.927(4)
avg. Ni–P (Å):	2.2008(9)
avg. Li–N (Å):	1.987(4)
Σ(P–Ni–P) (deg):	359.993(1)
avg. Li to N_3–plane:	0.268(5)
Ni to P_3–plane:	0.0101(7)

Figure S33. Molecular structure of **5** shown at 50% thermal ellipsoid probability. Hydrogen atoms and non-coordinating solvent molecules have been omitted for clarity. Atom colors: Li, light purple; Ni, pink; P, orange; N, blue; O, red; C, gray.

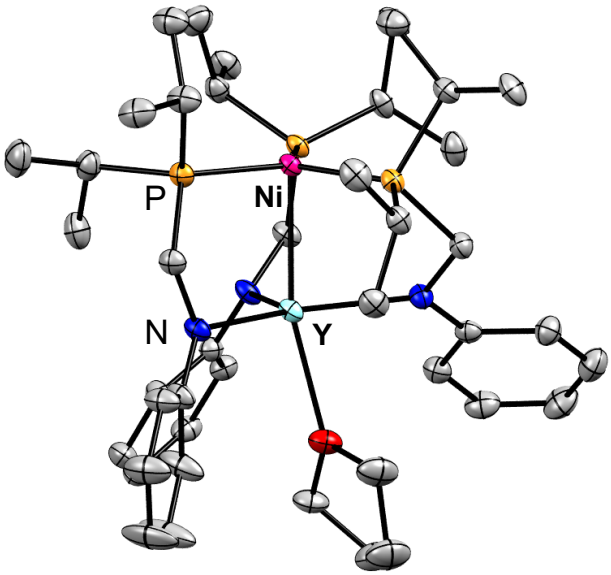

Figure S34. Molecular structure of **7**–THF shown at 50% thermal ellipsoid probability. Hydrogen atoms and non-coordinating solvent molecules have been omitted for clarity. Atom colors: Y, light blue; Ni, pink; P, orange; N, blue; O, red; C, gray.

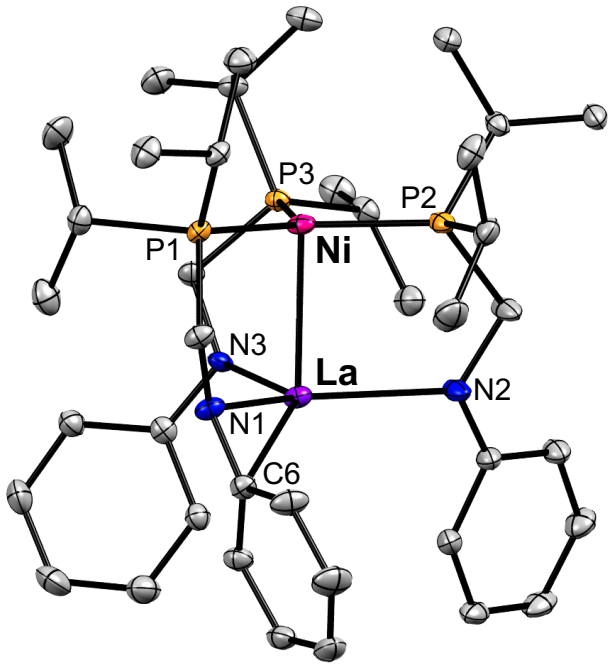

Figure S35. A different solid-state conformer of $NiLaL_3$, **8**', that features a η^2-(N-C_{ipso}) interaction between the NPh group and the La center. Crystals of **8**' were isolated from hot toluene recrystallization. Thermal ellipsoids shown at 50% probability. Hydrogen atoms and non-coordinating solvent molecules have been omitted for clarity. Atom colors: La, purple; P, orange; N, blue; O, red; C, gray.

Table S5. Table of X–ray Structural Parameters, Bond Lengths (Å) and Angles (deg), for Heterobimetallic Complexes 6–9.

	6 ($NiScL_3$)	7 ($NiYL_3$)	8 ($NiLaL_3$)	9 ($NiGaL_3$)
Ni–M	**2.3569(7)**	**2.4823(3)**	2.5732(4)	**2.3342(11); 2.3448(12)**
$r_{Pyykkö}$	**0.91**	**0.91**	**0.89**	**1.00; 1.00**
	2.2184(4)	2.2167(6)	2.2352(5)	2.2116(9); 2.1920(10)
Ni–P	2.2184(4)	2.2274(6)	2.2352(5)	2.2154(8); 2.1993(7)
	2.2184(4)	2.2362(6)	2.2352(5)	2.2048(9); 2.1933(7)
avg. Ni−P	**2.2184(2)**	**2.2268(3)**	**2.2352(3)**	**2.2106(5); 2.1949(5)**
	2.1021(14)	2.2503(17)	2.4288(18)	1.9188(13); 1.9234(13)
M–N	2.1021(14)	2.2591(17)	2.4288(18)	1.9045(13); 1.9159(12)
	2.1021(14)	2.2639(17)	2.4288(18)	1.9208(13); 1.9254(13)
avg. M–N	**2.1021(8)**	**2.2578(9)**	**2.4288(10)**	**1.9147(8); 1.9216(7)**
	119.844(2)	121.11(2)	119.913(2)	119.89(3); 119.76(2)
P–Ni–P	119.845(2)	118.34(2)	119.913(2)	120.61(2); 119.39(3)
	119.843(2)	120.30(2)	119.913(2)	116.80(2); 118.69(2)
Σ(P–Ni–P)	**359.532(2)**	**359.75(4)**	**359.739(3)**	**357.30(4); 357.84(4)**
	115.69(3)	116.28(6)	119.943(3)	115.69(5); 117.18(5)
N–M–N	115.69(3)	120.03(6)	119.943(3)	116.95(5): 114.78(5)
	115.69(3)	118.50(6)	119.943(3)	112.81(6); 114.07(5)
Σ(N–M–N)	**347.07(5)**	**354.81(10)**	**359.829(5)**	**345.45(9); 346.03(9)**
M to N_3–plane	0.4427(15)	0.2994(10)	–0.058(60)	0.4280(7); 0.4207(7)
Ni to P_3–plane	0.0881(6)	0.0645(4)	–0.066(18)	0.2108(3); 0.1873(3)

Table S6. Table of X–ray Structural Parameters, Bond Lengths (Å) and Angles (deg), for Heterobimetallic Complexes 7–DPA, 7–THF, and 8'

	7–DPA	7–THF	8'[a]
Ni–M	**2.6799(4); 2.7263(4)**	**2.5905(3)**	**2.6602(2)**
$r_{Pyykkö}$	**0.98; 1.0**	**0.95**	**0.92**
	2.2168(7); 2.2417(7)	2.1856(6)	2.2272(4)
Ni–P	2.2278(7); 2.2100(8)	2.1885(6)	2.2208(5)
	–	2.2111(5)	2.1934(16)
avg. Ni−P	**2.2222(5); 2.2259(5)**	**2.1951(3)**	**2.2138(6)**
	2.239(2); 2.221(2)	2.2330(15)	2.4217(13)
M–N	2.2892(19); 2.299(2)	2.3181(16)	2.4319(14)
	2.293(2); 2.293(3)	2.3438(16)	2.4212(5)
avg. M–N	**2.274(1); 2.271(2)**	**2.2983(9)**	**2.4249(7)**
	107.88(3); 107.35(3)	116.81(2)	119.616(17)
P–Ni–P	–	121.88(2)	118.71(3)
	–	121.23(2)	121.33(4)
Σ(P–Ni–P)	**–**	**359.92(3)**	**359.66(5)**
N–M–N	118.97(7); 116.48(7)	104.13(5)	120.15(5)
	99.75(7); 101.47(7)	115.23(6)	113.94(4)
	131.87(7); 134.27(8)	140.47(5)	125.84(4)
Σ(N–M–N)	**350.59(12); 352.22(13)**	**359.83(9)**	**359.93 (12)**
M to N_3–plane	–	0.0487(8)	–0.118(2)
Ni to P_3–plane	–	0.0369(3)	–0.071(3)
Y–O	–	2.3984(13)	–
Y–P	2.9894(7); 2.9897(7)	–	–
$C_{DPA}{\equiv}C_{DPA}$	1.286(3); 1.276(4)	–	–
Ph–C≡C	142.9(2)/136.4(2); 148.5(3)/142.1(3)	–	–

[a] A different solid-state conformer of $NiLaL_3$, **8'**, that features a η^2-(N-C_{ipso}) interaction between the NPh group and the La center.

Table S7. R^2_{adj} correlation values for M-N, Ni-P, Ni-M bond lengths (Å) of complexes 1 and 6–9 vs different M(III) parameters.

$NiML_3$	M-N bond length (Å)	Ni-P bond length (Å)	Ni-M bond length (Å)	M^{3+} Ionic Radii (Å)[a]	Pyykkö Covalent Radii (Å)[b]	Pauling Metallic Radii (Å)[c]	Codero Covalent Radii (Å)[d]	Pauling Electronegativity[e]	p*Ka* of $M(H_2O)_n^{3+}$ ion[f]	Charge Density (mm^3)
6 (M=Sc)	2.102	2.2184	2.3569	0.745	1.48	1.429	1.7	1.36	5.11	277
7 (M=Y)	2.258	2.2268	2.4823	0.9	1.63	1.616	1.9	1.22	8.43	157
1 (M=Lu)	2.213	2.2188	2.4644	0.861	1.62	1.557	1.87	1.27	7.9	180
8 (M=La)	2.429	2. 2352	2.5732	1.032	1.8	1.69	2.07	1.1	9.06	104
9 (M=Ga)	1.918	2.2027	2.3395	0.62	1.24	1.245	1.22	1.81	2.95	481
M-N bond length R^2_{adj}				**0.99**	**0.99**	0.96	0.93	0.90	0.88	0.92
Ni-P bond length R^2_{adj}				0.91	0.93	0.93	0.92	0.92	0.78	0.90
Ni-M bond length R^2_{adj}				**0.93**	0.83	0.83	0.68	0.60	0.83	0.70

[a]Ionic radii for six-coordinate species. Ref. 11, [b]single–bond radii for a coordination number of three. Ref. 12&13, [c]Ref. 14, [d]Ref. 15, [e]Ref. 16, [f]Ref. 10. .

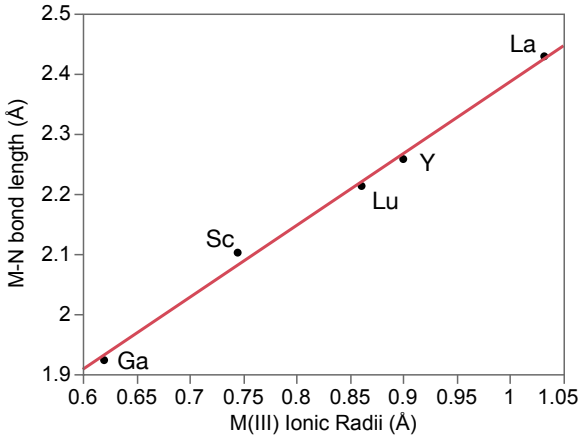

Linear Fit

M-N bond length (Å) = 1.1797355 + 1.2075812*M(III) Ionic Radii (Å)

Summary of Fit

RSquare	0.994782
RSquare Adj	0.993043
Root Mean Square Error	0.015805
Mean of Response	2.18396
Observations (or Sum Wgts)	5

Analysis of Variance

Source	DF	Sum of Squares	Mean Square	F Ratio
Model	1	0.14287547	0.142875	571.9435
Error	3	0.00074942	0.000250	Prob > F
C. Total	4	0.14362489		0.0002*

Parameter Estimates

Term	Estimate	Std Error	t Ratio	Prob>|t|
Intercept	1.1797355	0.042582	27.71	0.0001*
M(III) Ionic Radii (Å)	1.2075812	0.050494	23.92	0.0002*

Figure S36. Plot of M–N bond length vs ionic radii of M(III) ion for heterobimetallic complexes **1** and **6**–**9**.

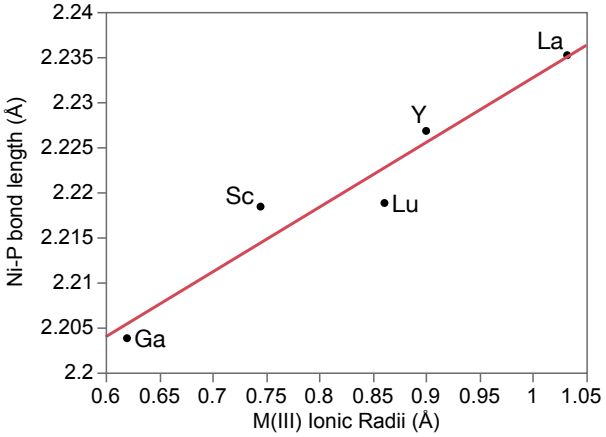

Linear Fit

Ni-P bond length (Å) = 2.1586307 + 0.0742536*M(III) Ionic Radii (Å)

Summary of Fit

RSquare	0.931635
RSquare Adj	0.908847
Root Mean Square Error	0.003635
Mean of Response	2.22038
Observations (or Sum Wgts)	5

Analysis of Variance

Source	DF	Sum of Squares	Mean Square	F Ratio
Model	1	0.00054021	0.000540	40.8823
Error	3	0.00003964	0.000013	Prob > F
C. Total	4	0.00057985		0.0077*

Parameter Estimates

Term	Estimate	Std Error	t Ratio	Prob>|t|
Intercept	2.1586307	0.009793	220.42	<.0001*
M(III) Ionic Radii (Å)	0.0742536	0.011613	6.39	0.0077*

Figure S37. Plot of Ni–P bond length vs ionic radii of M(III) ion for heterobimetallic complexes **1** and **6**–**9**.

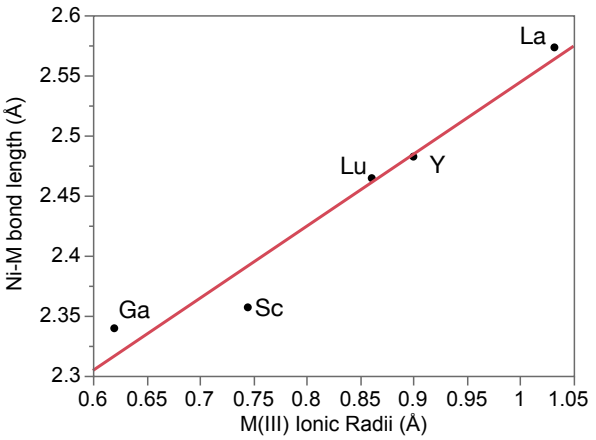

Linear Fit

Ni-M bond length (Å) = 1.9444706 + 0.5997949*M(III) Ionic Radii (Å)

Summary of Fit

RSquare	0.950595
RSquare Adj	0.934126
Root Mean Square Error	0.024711
Mean of Response	2.44326
Observations (or Sum Wgts)	5

Analysis of Variance

Source	DF	Sum of Squares	Mean Square	F Ratio
Model	1	0.03524768	0.035248	57.7220
Error	3	0.00183194	0.000611	Prob > F
C. Total	4	0.03707961		0.0047*

Parameter Estimates

Term	Estimate	Std Error	t Ratio	Prob>|t|
Intercept	1.9444706	0.066575	29.21	<.0001*
M(III) Ionic Radii (Å)	0.5997949	0.078946	7.60	0.0047*

Figure S38. Plot of Ni–M bond length vs ionic radii of M(III) ion of heterobimetallic complexes **1** and **6**–**9**.

Alkyne Semihydrogenation Catalytic Data

Catalysis was monitored via ^{1}H NMR spectroscopy by integrating selected peaks for various (by)products relative to those of the internal standard (1,3,5-trimethoxybenzene (TMB), recycle delay = 20s).

^{1}H NMR proton resonances used in quantification of diphenylacetylene starting material conversion and product yields (toluene–d_8, 400 MHz):
diphenylacetylene: 7.45 (m, 4H)
(*E*)–stilbene: 7.29 (dd, J = 8.3, 1.3 Hz, 4 H)
(Z)–stilbene: 6.43 (s, 2 H)
1, 2–diphenylethane: 2.71 (s, 4H)
1,2,3,4-tetraphenyl-1,3-butadiene: 6.53 (s, 2H)
1,3,5-trimethoxybenzene (internal standard, TMB): 6.14 (s, 3H)

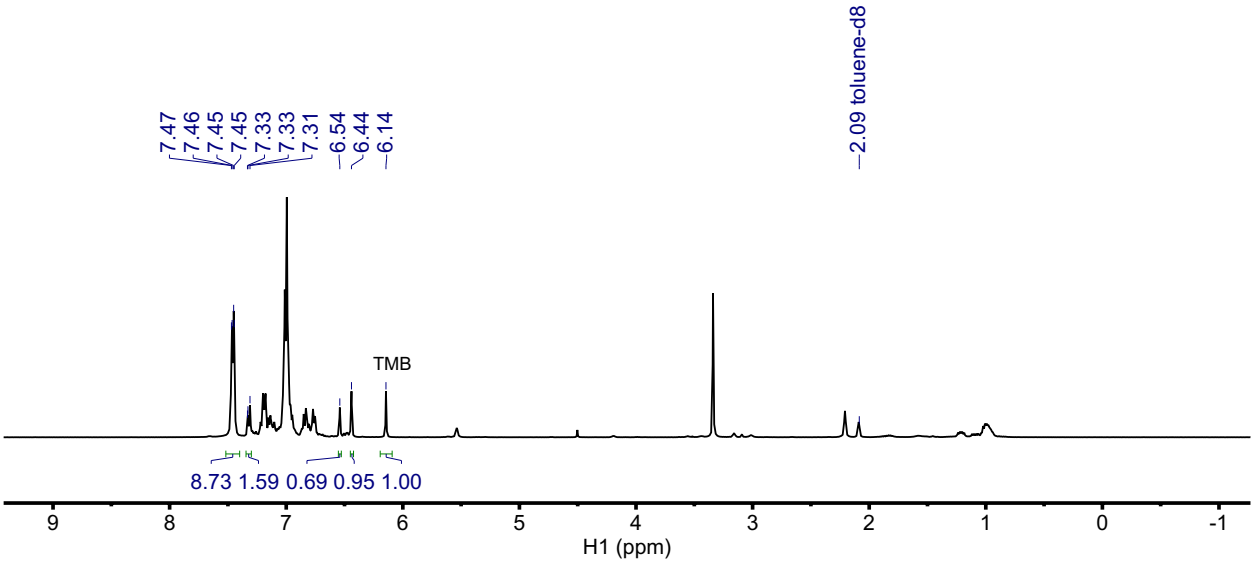

Figure S39. Representative ^{1}H NMR spectrum (400 MHz, toluene–d_8) of the catalytic semihydrogenation of diphenylacetylene by **Ni(COD)$_2$ + HL$_3$** (Table 1, entry 1: 2.5 mol %, 70°C, 24 h). Integrations used to quantify conversion are labeled.

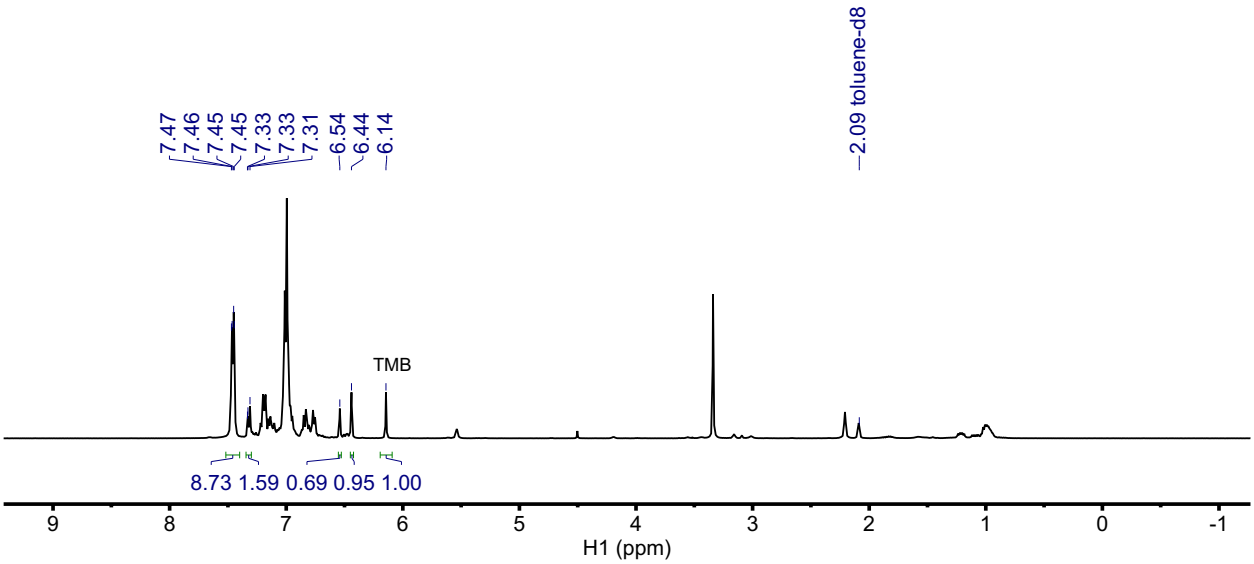

Figure S40. Representative ^{1}H NMR spectrum (400 MHz, toluene–d_8) of the catalytic semihydrogenation of diphenylacetylene by **5** (Table 1, entry 2: 2.5 mol %, 70°C, 24 h). Integrations used to quantify conversion are labeled.

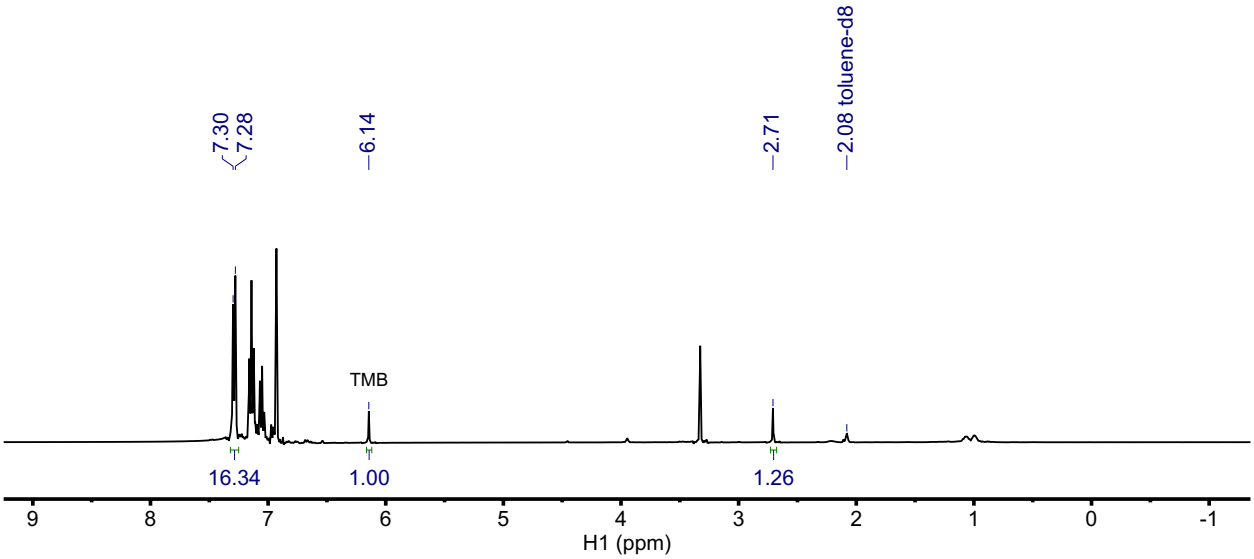

Figure S41. Representative ^{1}H NMR spectrum (400 MHz, toluene–d_8) of the catalytic semihydrogenation of diphenylacetylene by **1** (Table 1, entry 3: 2.5 mol %, 70°C, 24 h). Integrations used to quantify conversion are labeled.

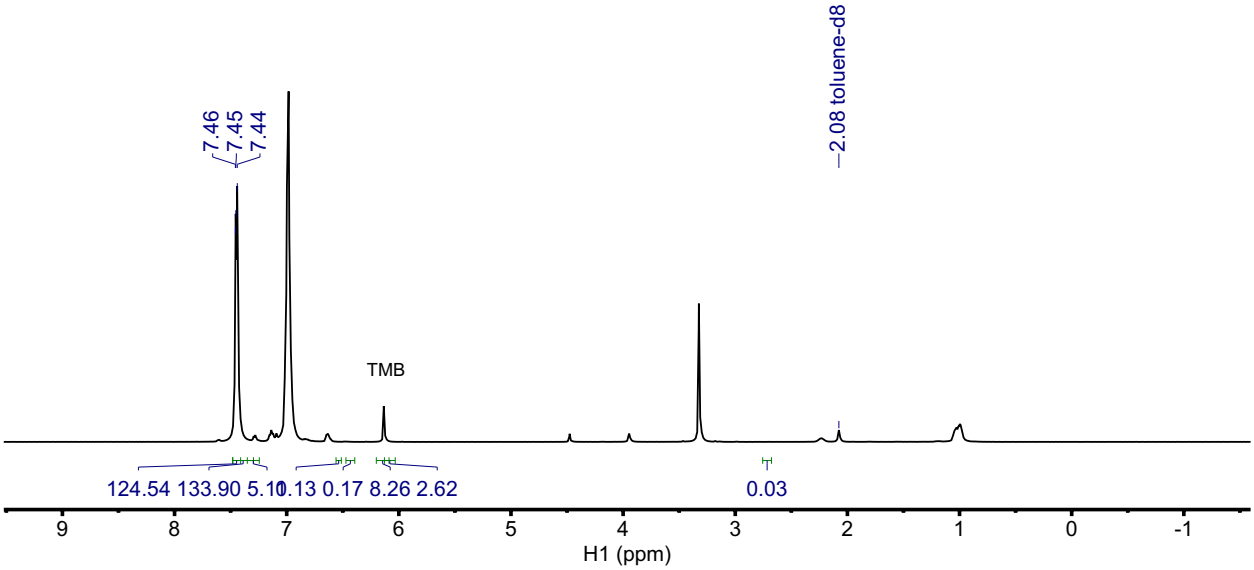

Figure S42. Representative ^{1}H NMR spectrum (400 MHz, toluene–d_8) of the catalytic semihydrogenation of diphenylacetylene by **6** (Table 1, entry 4: 2.5 mol %, 70°C, 24 h). Integrations used to quantify conversion are labeled.

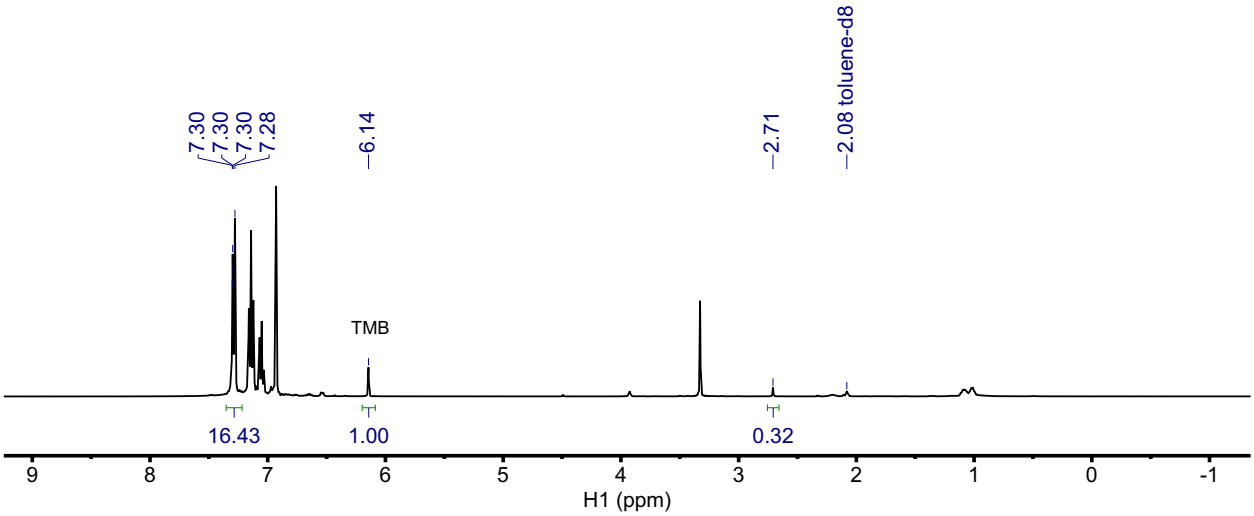

Figure S43. Representative ^{1}H NMR spectrum (400 MHz, toluene–d_8) of the catalytic semihydrogenation of diphenylacetylene by **7** (Table 1, entry 5: 2.5 mol %, 70°C, 24 h). Integrations used to quantify conversion are labeled.

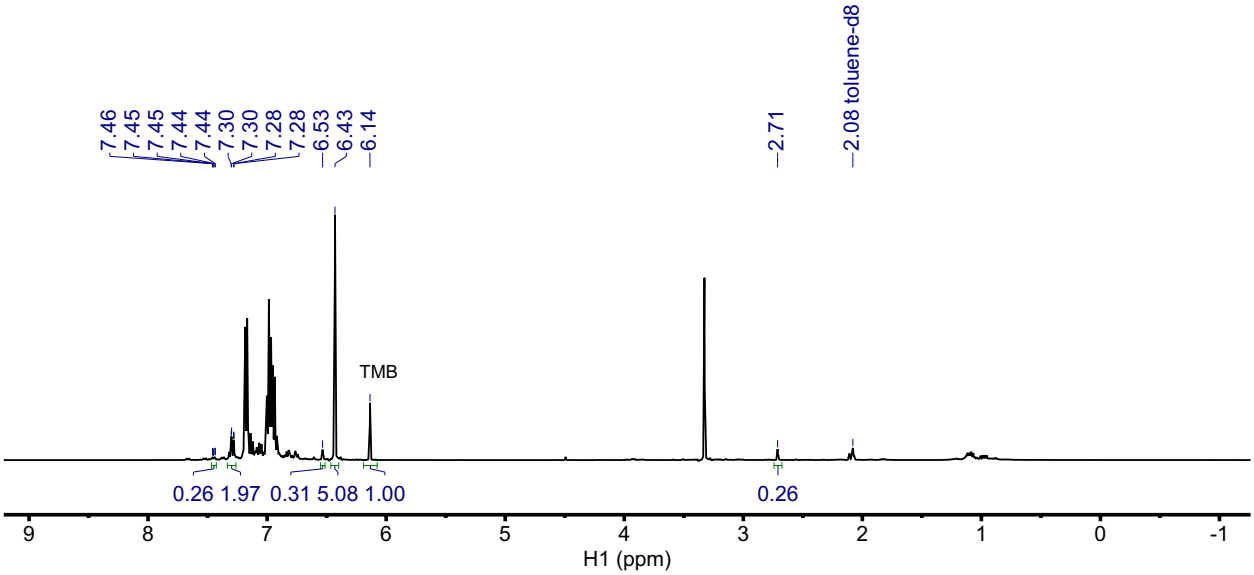

Figure S44. Representative ^{1}H NMR spectrum (400 MHz, toluene–d_8) of the catalytic semihydrogenation of diphenylacetylene by **8** (Table 1, entry 6: 2.5 mol %, 70°C, 24 h). Integrations used to quantify conversion are labeled.

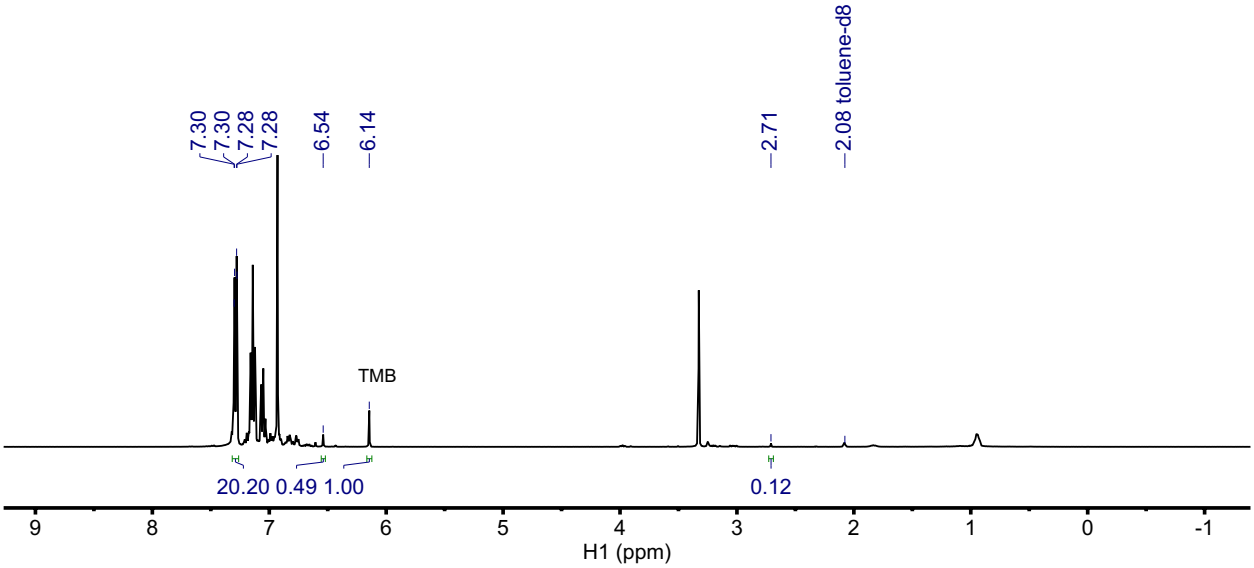

Figure S45. Representative ^{1}H NMR spectrum (400 MHz, toluene–d_8) of the catalytic semihydrogenation of diphenylacetylene by **9** (Table 1, entry 7: 2.5 mol %, 70°C, 24 h). Integrations used to quantify conversion are labeled.

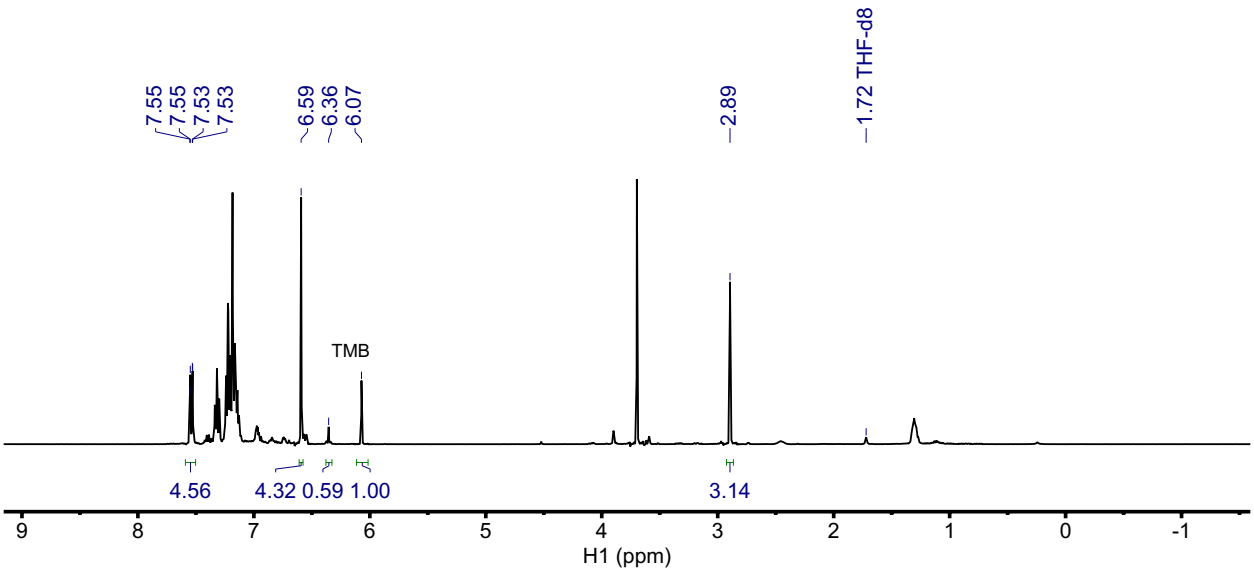

Figure S46. Representative ^{1}H NMR spectrum (400 MHz, THF–d_8) of the catalytic semihydrogenation of diphenylacetylene by **7**–THF (Table 1, entry 8: 2.5 mol %, 70°C, 24 h). Integrations used to quantify conversion are labeled.

Initial Rate Studies

Initial rate studies of syn-hydrogenation of diphenylacetylene

Kinetic data was collected every 180 seconds at 344 K until either 10 % conversion of diphenylacetylene or for 1 h. The conversion of diphenylacetylene was monitored via ^{1}H NMR spectroscopy by quantitative integration of the aryl proton at 7.42 ppm (m, 4H) against that of the internal 1,3,5-trimethoxybenzene standard. With the single exception of **6**, *Z*-stilbene was the only observed product during the initial rate studies, so that:

$$\text{Rate of DPA } \textit{syn}\text{-hydrogenation} = \frac{d[Z\text{–}stilbene]}{dt} = -\frac{d[\text{DPA}]_{observed}}{dt} \quad \text{(eq. 1)}$$

However, for **6**, competitive formation of the 1,2,3,4-tetraphenyl-1,3-butadiene (referred to as the *Z*,*Z*-diene) and *E*-stilbene (derived from *Z*-stilbene isomerization) was observed. Since the Z,Z-diene is the product of 1 mol H_2 and 2 mol DPA, then the observed rate with respect to [DPA] is equivalent to:

$$-\frac{d[\text{DPA}]_{observed}}{dt} = \frac{d[Z\text{–}stilbene]}{dt} + \frac{d[E\text{–}stilbene]}{dt} + 2\,\frac{d[Z,Z\text{–}diene]}{dt} \quad \text{(eq. 2)}$$

On the other hand, DPA *syn*-hydrogenation, which involves the key step of a *single* DPA insertion into Ni−H bond, will also lead to the Z,Z-diene product. Therefore, the rate of DPA syn-hydrogenation is no longer equal to $-\frac{d[\text{DPA}]_{observed}}{dt}$, and is instead:

$$\text{Rate of DPA } \textit{syn}\text{-hydrogenation} = \frac{d[Z\text{–}stilbene]}{dt} + \frac{d[E\text{–}stilbene]}{dt} + \frac{d[Z,Z\text{–}diene]}{dt} \text{ (eq. 3)}$$

Substituting equation 3 into equation 2,

$$\text{Rate of DPA } \textit{syn}\text{-hydrogenation} = -\frac{d[\text{DPA}]_{observed}}{dt} - \frac{d[Z,Z\text{–}diene]}{dt} \quad \text{(eq. 4)}$$

The rate of *Z*,*Z*-diene was monitored via ^{1}H NMR spectroscopy by quantitative integration of the vinylic proton at 6.53 ppm (s, 2H) against that of the internal 1,3,5-trimethoxybenzene standard.

$$\text{Rate of DPA } \textit{syn}\text{-hydrogenation} = -\left(-7.8(4) \times 10^{-6}\,\frac{10^{-6}M}{s}\right) - \left(1.1(1) \times 10^{-6}\,\frac{M}{s}\right) = 6.7(4)\ x\ 10^{-6}M/s$$

Initial rate studies of isomerization of *cis*–stilbene

Kinetic data was collected every 30–60 seconds at 344 K until either 10 % conversion of *cis*–stilbene or for 45 min. The conversion of *cis*–stilbene was monitored via ^{1}H NMR spectroscopy by quantitative integration of the vinyl proton at 6.43 ppm (s, 2H) against that of the internal 1,3,5-trimethoxybenzene standard.

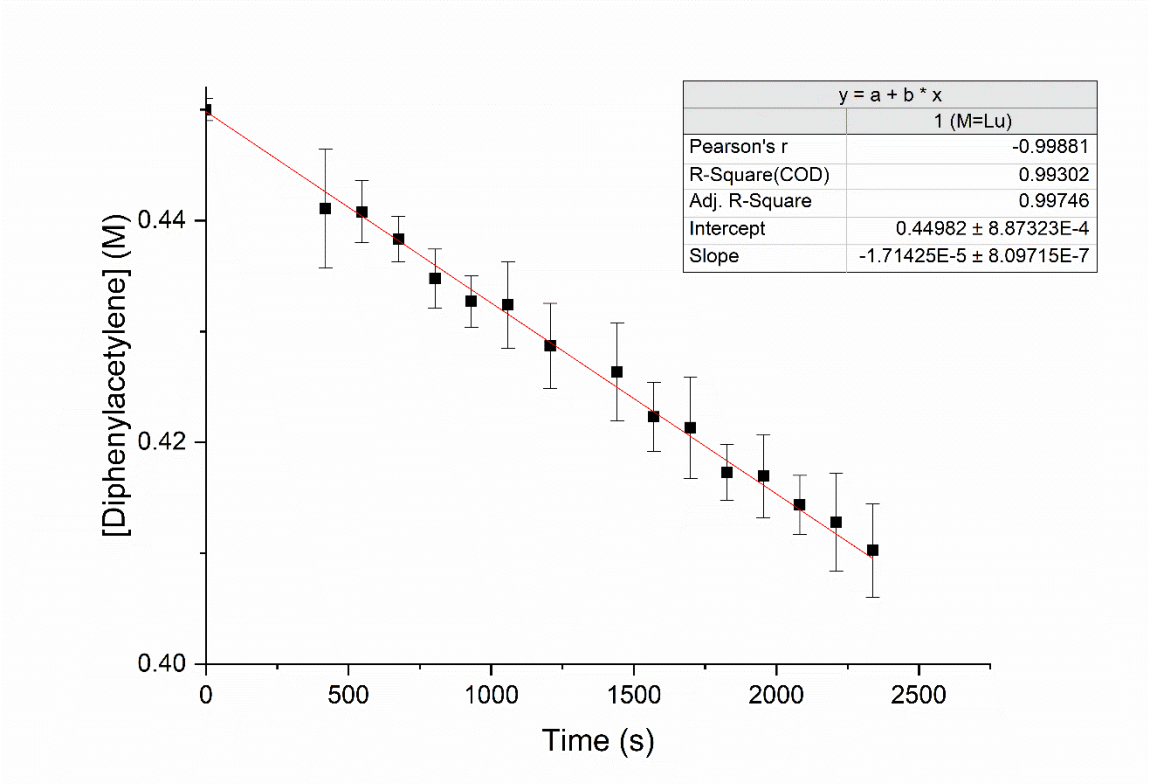

Figure S47. Initial rate kinetic data for the syn-hydrogenation of diphenylacetylene for $NiLuL_3$ **1**. Data is an average of 3 independent runs.

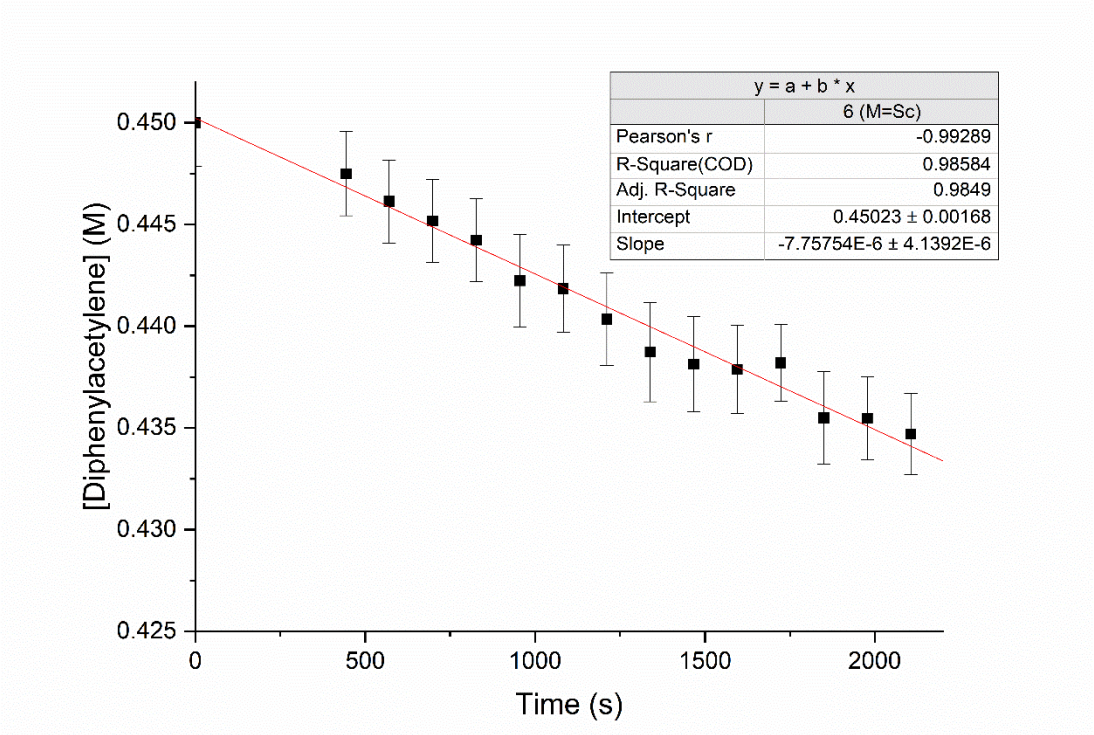

Figure S48. Initial rate kinetic data for the consumption of diphenylacetylene for $NiScL_3$ **6**. Data is an average of 3 independent runs.

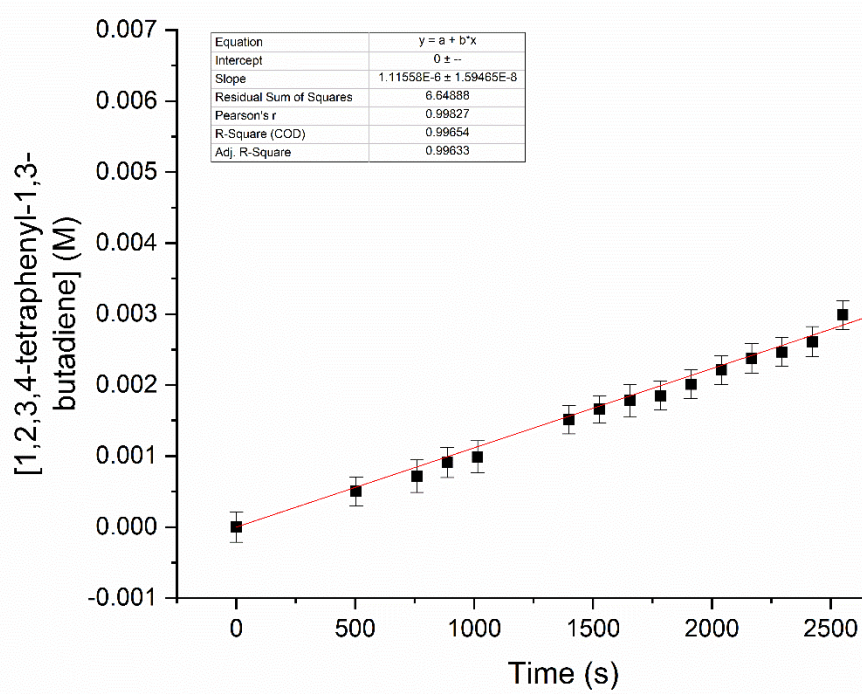

Figure S49. Initial rate kinetic data for the production of 1,2,3,4-tetraphenyl-1,3-butadiene for $NiScL_3$ **6**. Data is an average of 3 independent runs.

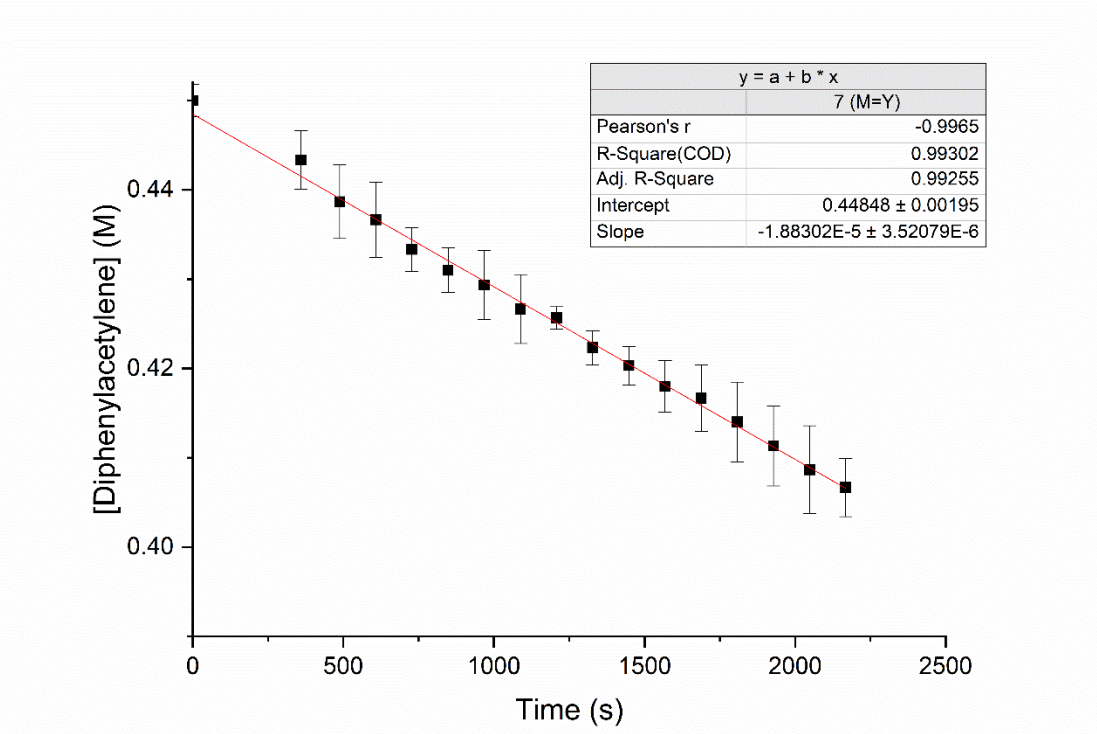

Figure S50. Initial rate kinetic data for the syn-hydrogenation of diphenylacetylene for $NiYL_3$ **7**. Data is an average of 3 independent runs.

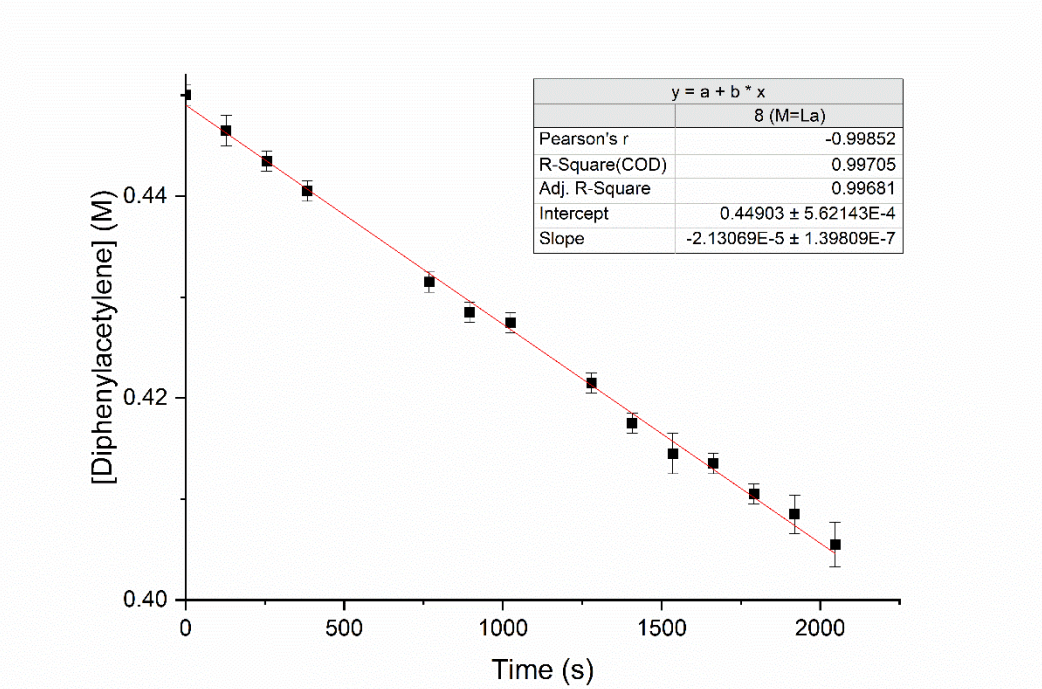

Figure S51. Initial rate kinetic data for the syn-hydrogenation of diphenylacetylene for $NiLaL_3$ **8**. Data is an average of 3 independent runs.

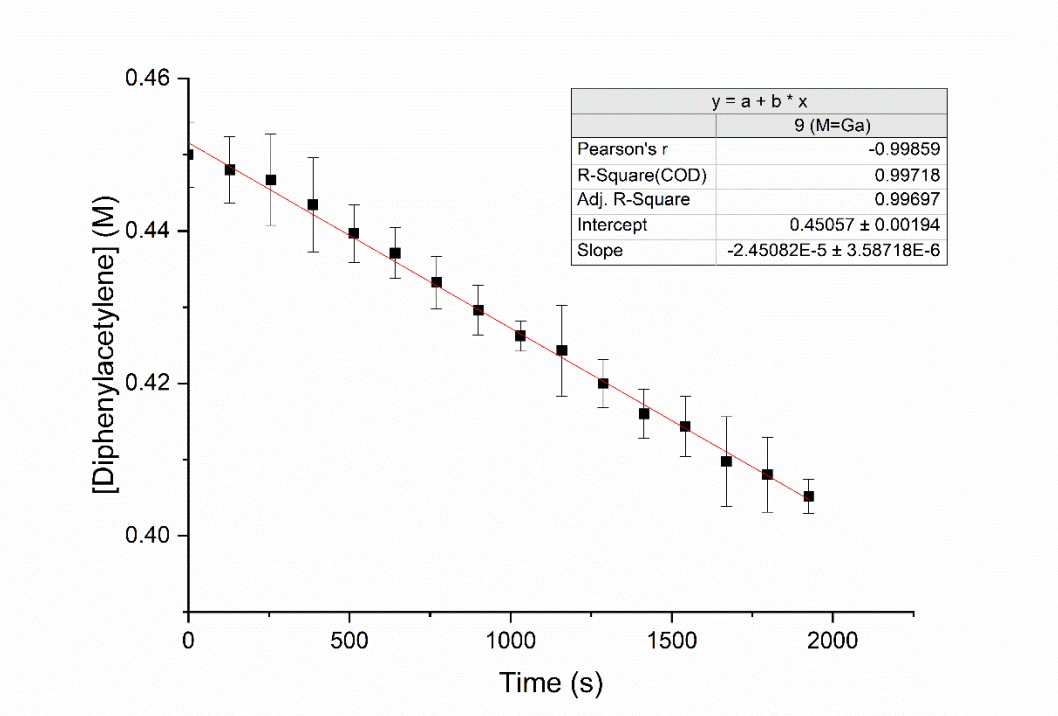

Figure S52. Initial rate kinetic data for the syn-hydrogenation of diphenylacetylene for $NiGaL_3$ **9**. Data is an average of 3 independent runs.

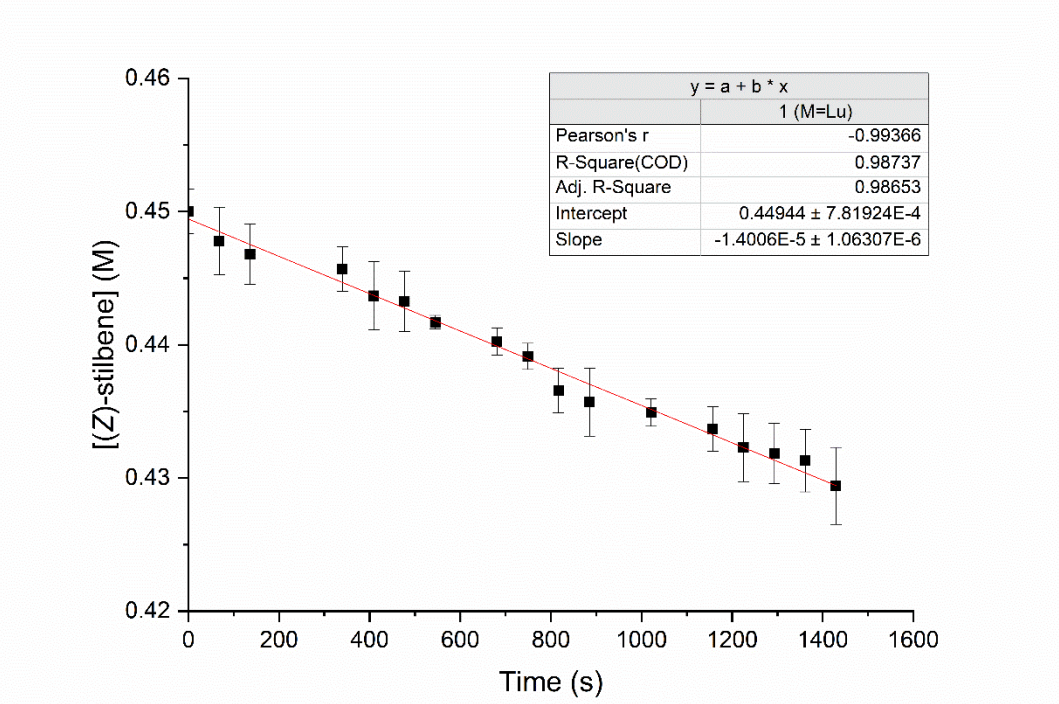

Figure S53. Initial rate kinetic data for the cis to trans isomerization of (*Z*)–stilbene for $NiLuL_3$ **1**. Data is an average of 3 independent runs.

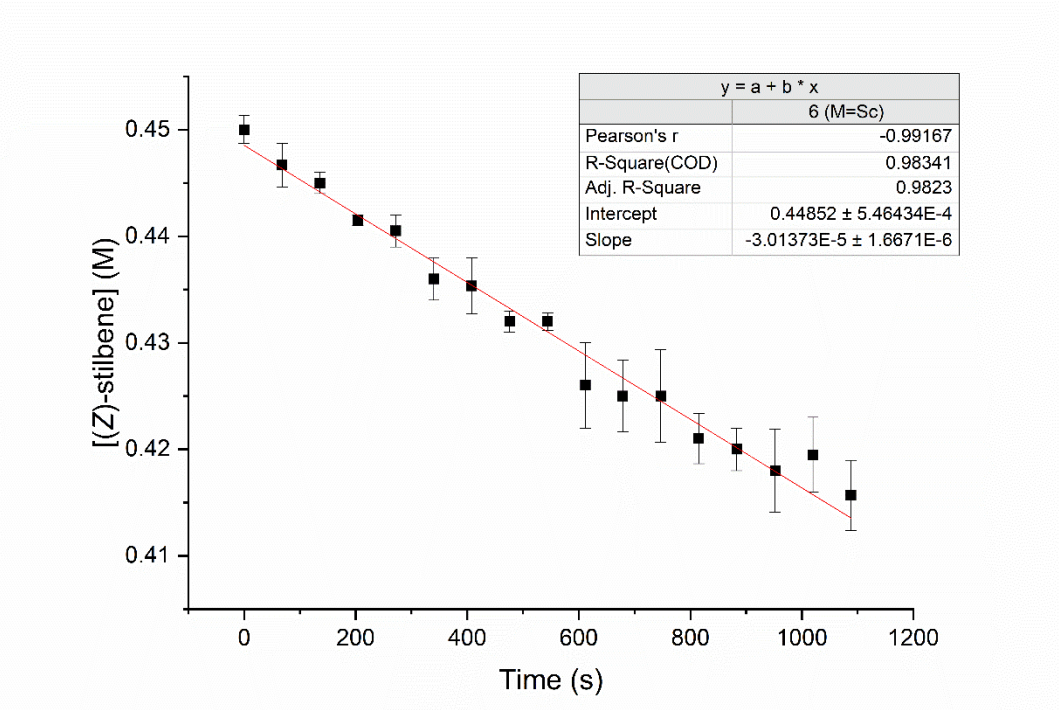

Figure S54. Initial rate kinetic data for the cis to trans isomerization of (*Z*)–stilbene for $NiScL_3$ **6**. Data is an average of 3 independent runs.

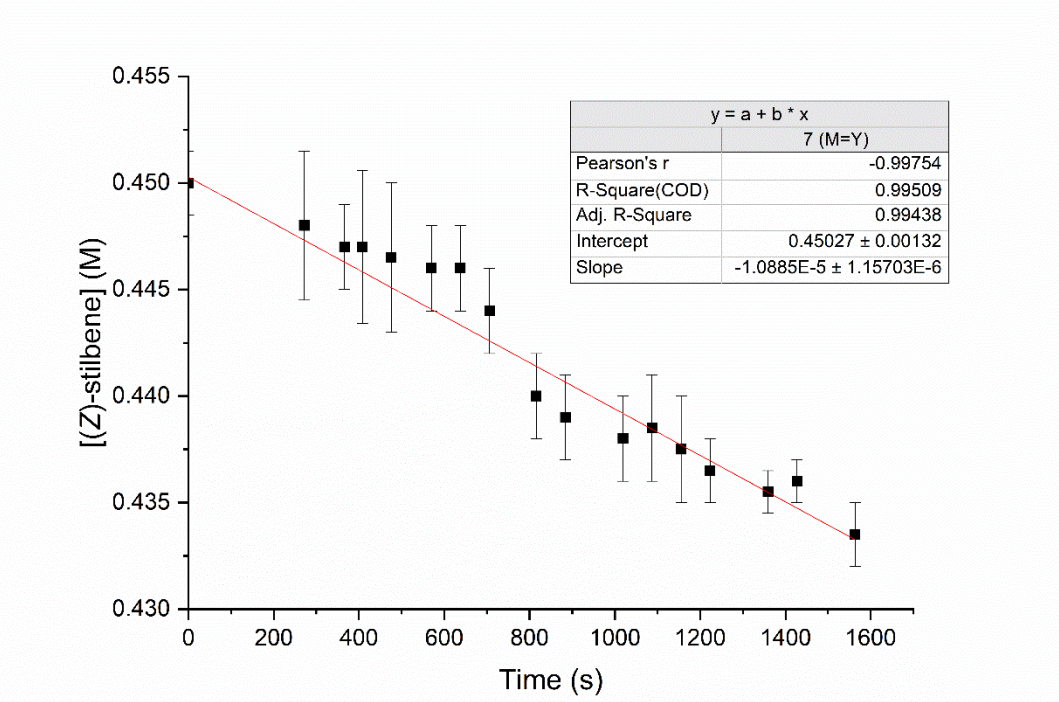

Figure S55. Initial rate kinetic data for the cis to trans isomerization of (*Z*)–stilbene for NiYL$_3$**7**. Data is an average of 3 independent runs.

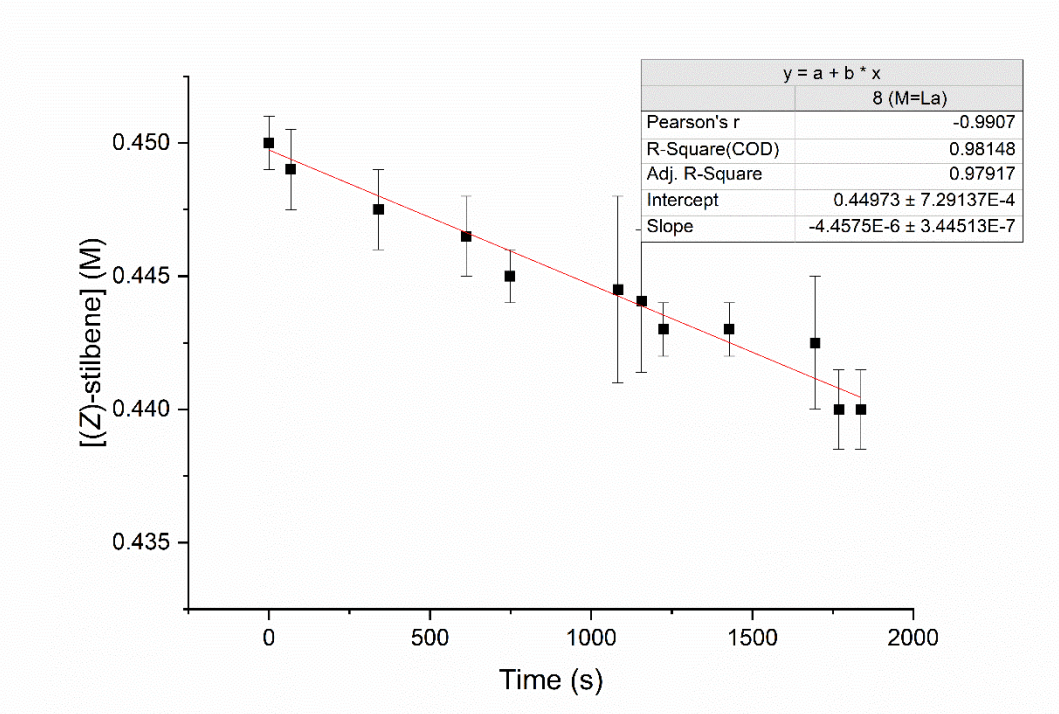

Figure S56. Initial rate kinetic data for the cis to trans isomerization of (*Z*)–stilbene for NiLaL$_3$ **8**. Data is an average of 3 independent runs.

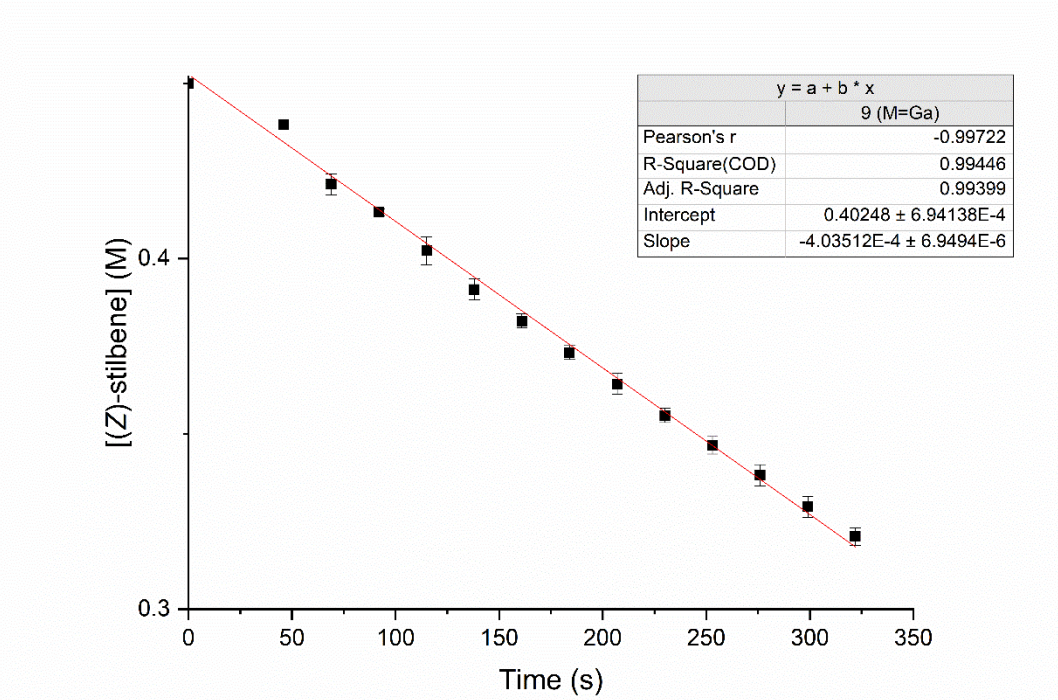

Figure S57. Initial rate kinetic data for the cis to trans isomerization of (*Z*)–stilbene for $NiGaL_3$ **9**. Data is an average of 3 independent runs.

Table S8. R^2_{adj} correlation values for initial rate of syn-hydrogenation of complexes 1 and 6-9 vs different M(III) parameters.

$NiML_3$	Initial Rate (10^{-5} M/s)	E_{pa} (V)	M^{3+} Ionic Radii (Å)[a]	Pyykkö Covalent Radii (Å)[b]	Pauling Metallic Radii (Å)[c]	Codero Covalent Radii (Å)[d]	Pauling Electronegativity[e]	p*K*a of $M(H_2O)_n^{3+}$ ion[f]	Charge Density (mm^3)
6 (M=Sc)	0.67	-0.57	0.745	1.48	1.429	1.7	1.36	5.11	277
7 (M=Y)	1.88	-1.23	0.9	1.63	1.616	1.9	1.22	8.43	157
1 (M=Lu)	1.71	-1.01	0.861	1.62	1.557	1.87	1.27	7.9	180
8 (M=La)	2.13	-1.17	1.032	1.8	1.69	2.07	1.1	9.06	104
9 (M=Ga)	2.45	-0.48	0.62	1.24	1.245	1.22	1.81	2.95	481
Ni-RE R^2_{adj}		0.94	0.85	0.82	0.94	0.87	0.81	**0.99**	**0.96**
Ni-M R^2_{adj}		0.05	0.01	0.01	0.00	0.04	0.08	0.00	0.03

[a]Ionic radii for six-coordinate species. Ref. 11, [b]single–bond radii for a coordination number of three. Ref. 12&13, [c]Ref. 14, [d]Ref. 15, [e]Ref. 16, [f]Ref. 10.

Table S9. R^2_{adj} correlation values for initial rate of *Z* to *E* isomerization of complexes 1 and 6-9 vs different M(III) parameters.

$NiML_3$	Initial Rate ($-1x10^{-5}$ M/s)	E_{pa} (V)	M^{3+} Ionic Radii (Å)[a]	Pyykkö Covalent Radii (Å)[b]	Pauling Metallic Radii (Å)[c]	Codero Covalent Radii (Å)[d]	Pauling Electronegativity[e]	p*K*a of $M(H_2O)_n^{3+}$ ion[f]	Charge Density (mm^3)
6 (M=Sc)	3.00	-0.57	0.745	1.48	1.429	1.7	1.36	5.11	277
7 (M=Y)	1.10	-1.23	0.9	1.63	1.616	1.9	1.22	8.43	157
1 (M=Lu)	1.40	-1.01	0.861	1.62	1.557	1.87	1.27	7.9	180
8 (M=La)	0.450	-1.17	1.032	1.8	1.69	2.07	1.1	9.06	104
9 (M=Ga)	40.4	-0.48	0.62	1.24	1.245	1.22	1.81	2.95	481
Ni-RE R^2_{adj}		0.84	0.87	0.84	**0.96**	0.90	0.83	**0.98**	**0.99**
Ni-M R^2_{adj}		0.33	0.50	0.67	0.67	0.83	0.88	0.61	0.82

[a]Ionic radii for six-coordinate species. Ref. 11, [b]single–bond radii for a coordination number of three. Ref. 12&13, [c]Ref. 14, [d]Ref. 15, [e]Ref. 16, [f]Ref. 10. .

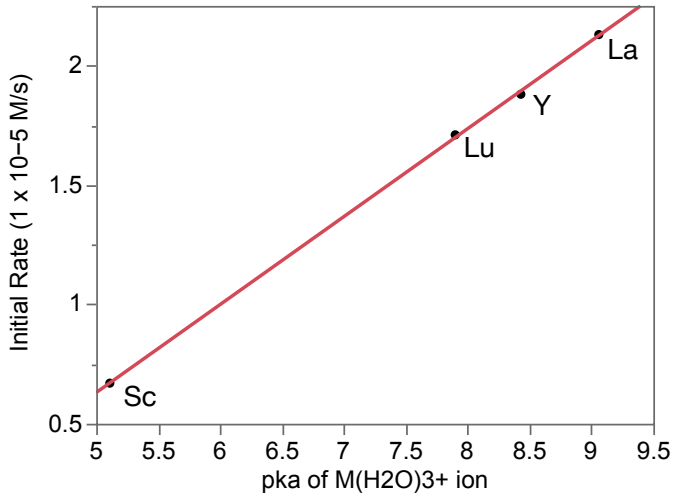

Linear Fit

Initial Rate (1 x 10−5 M/s) = -1.211321 + 0.3683699*pka of M(H2O)3+ ion

Summary of Fit

RSquare	0.999726
RSquare Adj	0.999589
Root Mean Square Error	0.013013
Mean of Response	1.5975
Observations (or Sum Wgts)	4

Analysis of Variance

Source	DF	Sum of Squares	Mean Square	F Ratio
Model	1	1.2359363	1.23594	7298.375
Error	2	0.0003387	0.00017	Prob > F
C. Total	3	1.2362750		0.0001*

Parameter Estimates

Term	Estimate	Std Error	t Ratio	Prob>|t|
Intercept	-1.211321	0.033516	-36.14	0.0008*
pka of M(H2O)3+ ion	0.3683699	0.004312	85.43	0.0001*

Figure S58. Plot of initial rate of syn–hydrogenation of diphenylacetylene vs pK_a of $M(H_2O)_6^{3+}$ ion by complexes **1** and **6**–**8**.

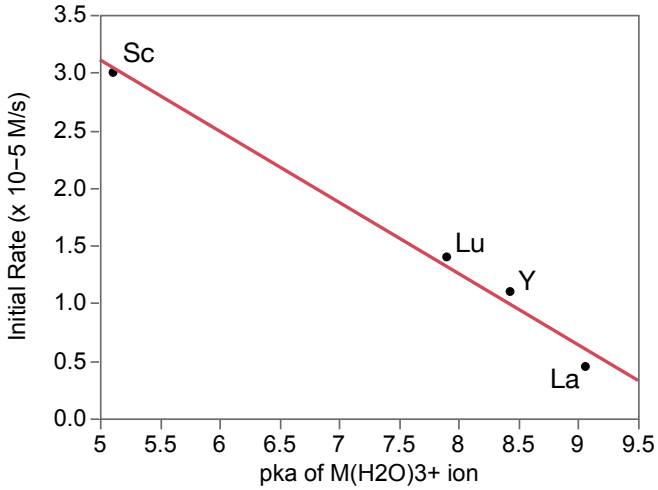

Linear Fit

Initial Rate (x 10−5 M/s) = 6.1997033 - 0.6179939*pka M(H2O)3+

Summary of Fit

RSquare	0.987693
RSquare Adj	0.98154
Root Mean Square Error	0.147211
Mean of Response	1.4875
Observations (or Sum Wgts)	4

Analysis of Variance

Source	DF	Sum of Squares	Mean Square	F Ratio
Model	1	3.4785330	3.47853	160.5156
Error	2	0.0433420	0.02167	Prob > F
C. Total	3	3.5218750		0.0062*

Parameter Estimates

Term	Estimate	Std Error	t Ratio	Prob>|t|
Intercept	6.1997033	0.379147	16.35	0.0037*
pka M(H2O)3+	-0.617994	0.048778	-12.67	0.0062*

Figure S59. Plot of initial rate of *Z* to *E* isomerization of *cis*–stilbene vs pK_a of $M(H_2O)_6^{3+}$ by complexes **1** and **6**–**8**.

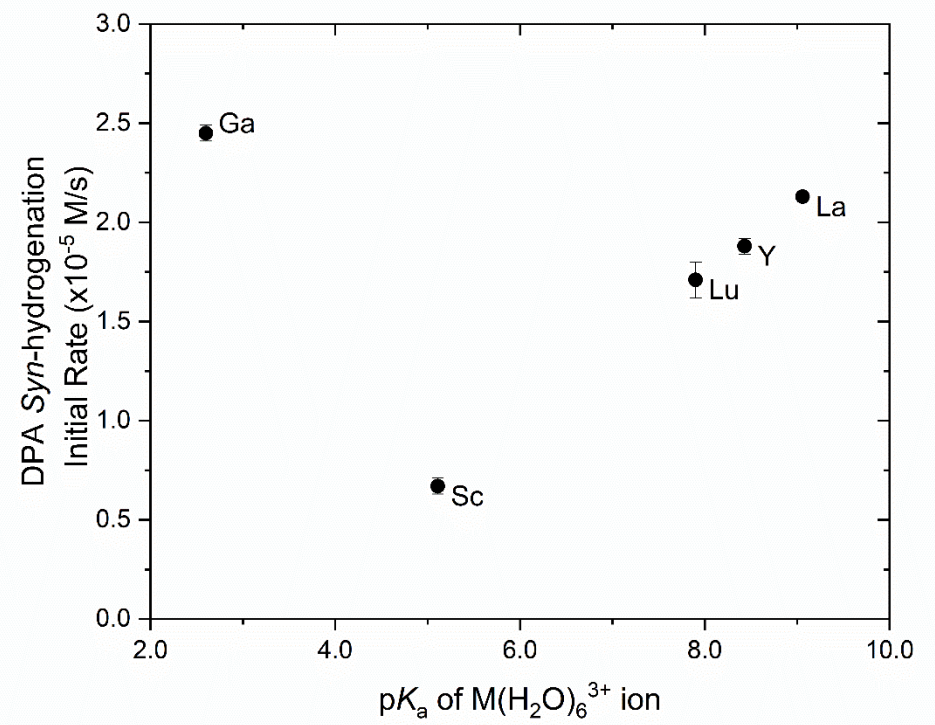

Figure S60. Plot of initial rate of *syn*-hydrogenation of diphenylacetylene vs pK_a of $M(H_2O)_6^{3+}$ ion by complexes **1** and **6**–**9**.

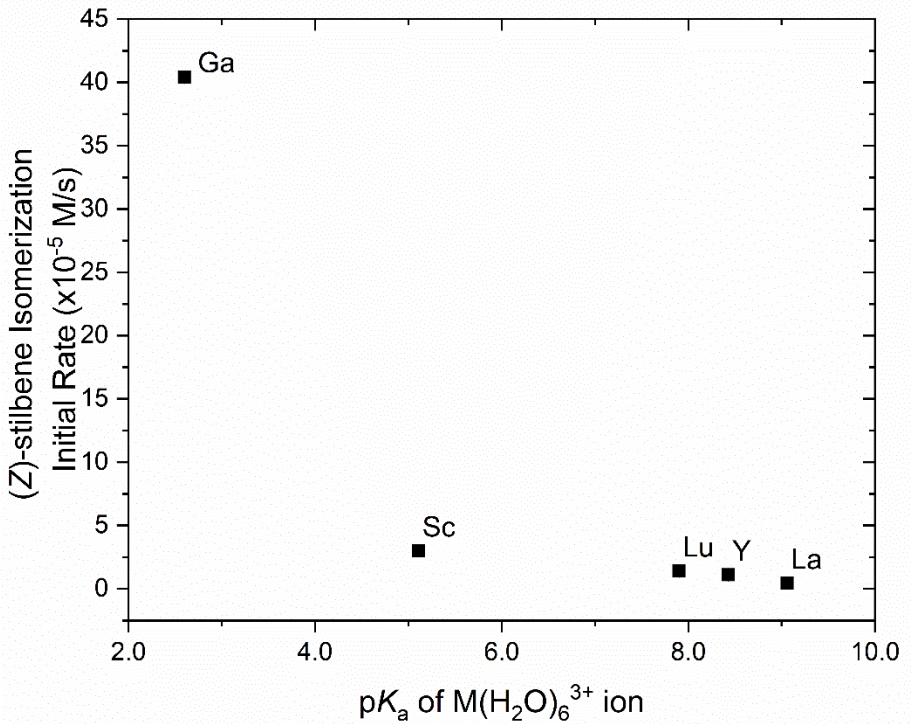

Figure S61. Plot of initial rate of *Z* to *E* isomerization of *cis*–stilbene vs pK_a of $M(H_2O)_6^{3+}$ ion by complexes **1** and **6**–**9**.

Mechanistic and Reaction Monitoring Studies

(Z)-stilbene isomerization catalysis

^{1}H NMR proton resonances used in quantification of starting material conversion and product yields (toluene–d_8, 400 MHz):
(*E*)–stilbene: 7.29 (dd, J = 8.3, 1.3 Hz, 4 H)
(*Z*)–stilbene: 6.43 (s, 2 H)
1, 2–diphenylethane: 2.71 (s, 4H)

Table S10. *Cis*–stilbene isomerization at 16 h for complexes 6, 7, and 9[a]

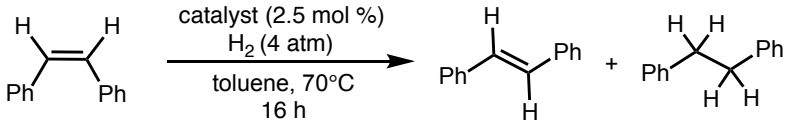

entry	catalyst	*Z*–stilbene conversion (%)[b,c]	*E*–stilbene:1,2–diphenylethane (%)[b,c]
1	**1** (M = Lu)	92	85:7
2	**6** (M = Sc)	>99	99:0
3	**7** (M = Y)	80	76:4
4[d]	**8** (M = La)	35	21:14
5	**9** (M = Ga)	>99	97:3

[a]Catalytic Conditions: 2.5 mol % precatalyst, 0.45 M *Z*–stilbene in ca. 500 μL of toluene–d_8, 4 atm H_2, heated to 70 °C. [b]Conversion at 16 h for triplicate runs based on ^{1}H NMR integration against an internal trimethoxybenzene standard (0.02 mmol). [c]Averaged over triplicate runs (±0.5 error bars).[d]Catalyst decomposition observed by ^{31}P and ^{1}H NMR spectroscopy.

Table S11. *Cis*–stilbene isomerization at 16 h for complexes 6, 7, and 9 in absence of H_2[a]

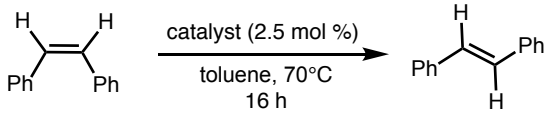

entry	catalyst	*Z*–stilbene conversion (%)[b,c]	*E*–stilbene (%)[b,c]
1	**1** (M = Lu)	<1	<1
2	**6** (M = Sc)	13	13
3	**7** (M = Y)	<1	<1
4	**8** (M = La)	<1	<1
5	**9** (M = Ga)	28	28

[a]Catalytic Conditions: 2.5 mol % precatalyst, 0.45 M *Z*–stilbene in ca. 500 μL of toluene–d_8 under Ar heated to 70 °C. [b]Conversion or yield at 16 h for duplicate runs based on ^{1}H NMR integration against an internal 1, 3,5–trimethoxybenzene standard (0.02 mmol). [c]Averaged over duplicate runs (±0.5 error bars).

Table S12. Alkene isomerization studies of **7** ($NiYL_3$) with varying conditions

entry	alkene	variation on conditions	*E:Z:alkane*[a]
1	*trans*-stilbene	none	99:<1:0
2	*cis*-stilbene	catalyst omitted	<1:99:0

[a]From ^{1}H NMR integration against an internal trimethoxybenzene standard at a 24 h timepoint.

General procedure for alkyne semi–hydrogenation reaction monitoring studies

Each catalytic run was set up as described under "Standard Catalytic Runs for Alkyne Semihydrogenation" in the Experimental Section. ^{1}H and ^{31}P{^{1}H} NMR time points were gathered every 30 min to 2 h for the first 8 h. All experiments were performed in triplicate.

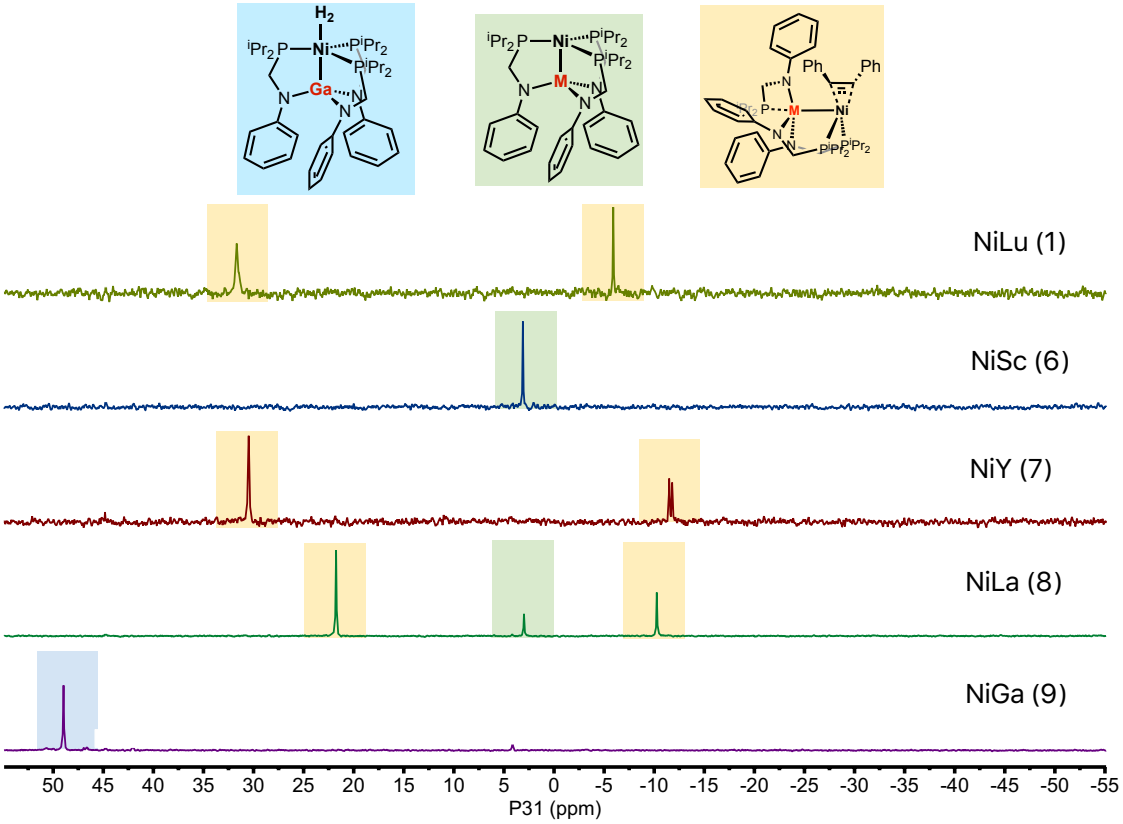

Figure S62. ^{31}P{^{1}H} NMR spectra (162 MHz, toluene–d_8) for complexes **6**–**9** at t = 0 h for the semihydrogenation of diphenylacetylene (40 equiv). For complexes **1**, **7**, and **8**, a diphenylacetylene adduct can be observed. For all diphenylacetylene adducts, the downfield shift (20-35 ppm) integrates to 2P, whereas the upfield shift (<0 ppm) integrates to 1P.

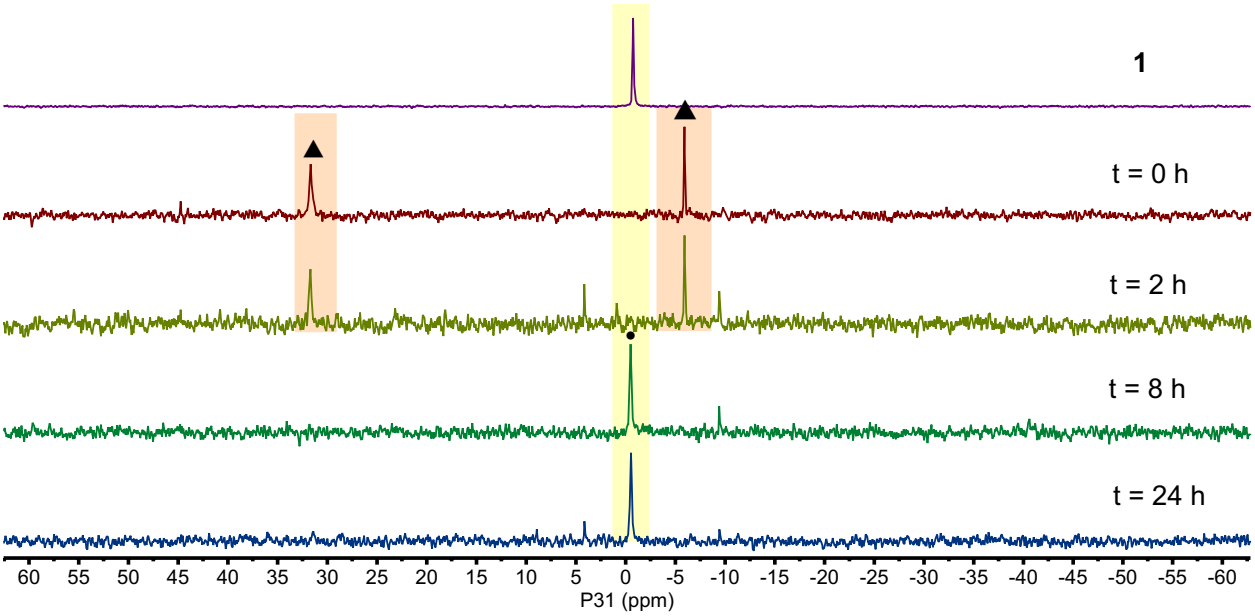

Figure S63. Changes in $^{31}P\{^{1}H\}$ NMR spectra (162 MHz, toluene–d_8) over the course of the semihydrogenation of 40 equiv diphenylacetylene with $NiLuL_3$ **1**. Naked Ni-Lu **1** is marked by a circle (•) and the DPA adduct (**1**-DPA) is marked by a triangle (▲).

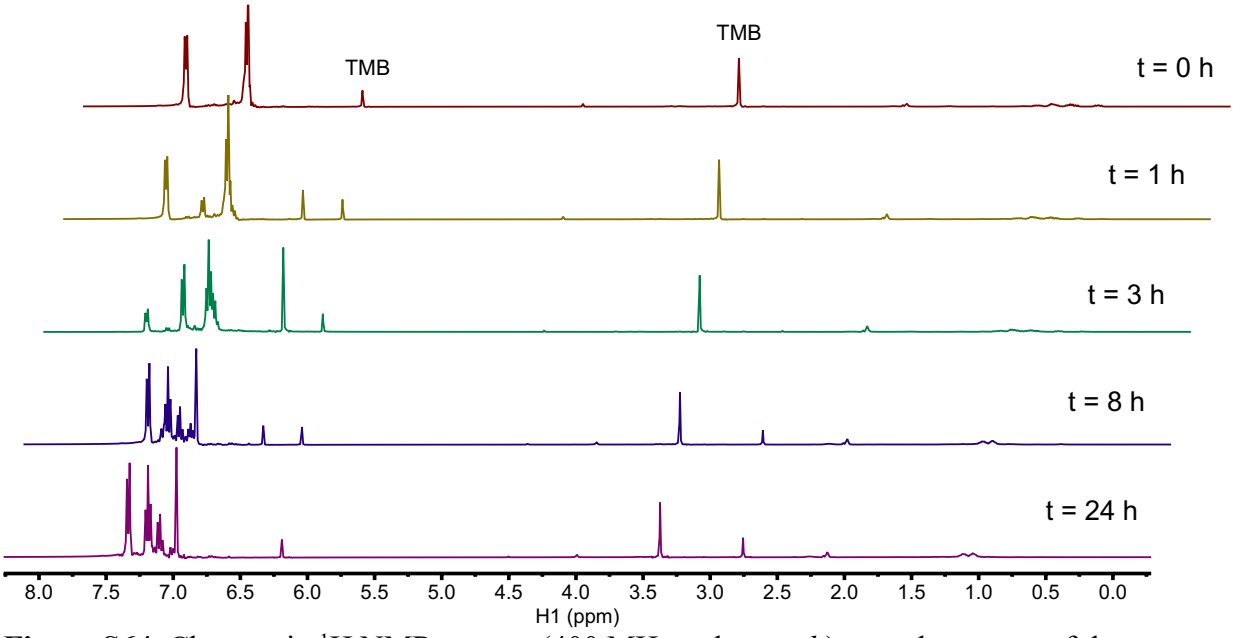

Figure S64. Changes in ^{1}H NMR spectra (400 MHz, toluene–d_8) over the course of the semihydrogenation of diphenylacetylene (40 equiv) with $NiLuL_3$ **1**.

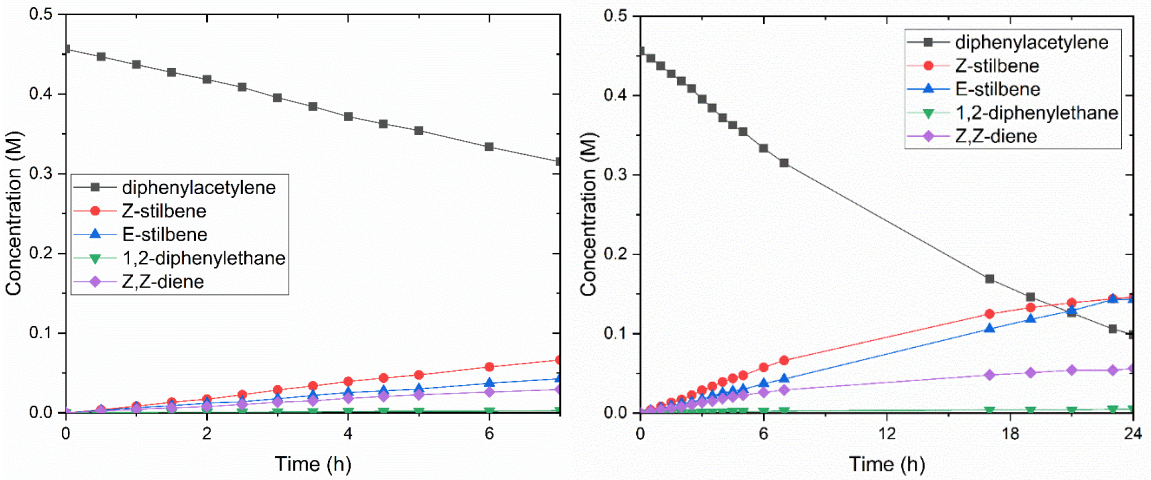

Figure S65. Time course of the semihydrogenation of DPA (40 equiv) with **6** at 70 °C: (left) 0 to 7 h, and (*right*) 0 to 24 h. The product 1,2,3,4-tetraphenyl-1,3-butadiene is abbreviated as Z,Z-diene.

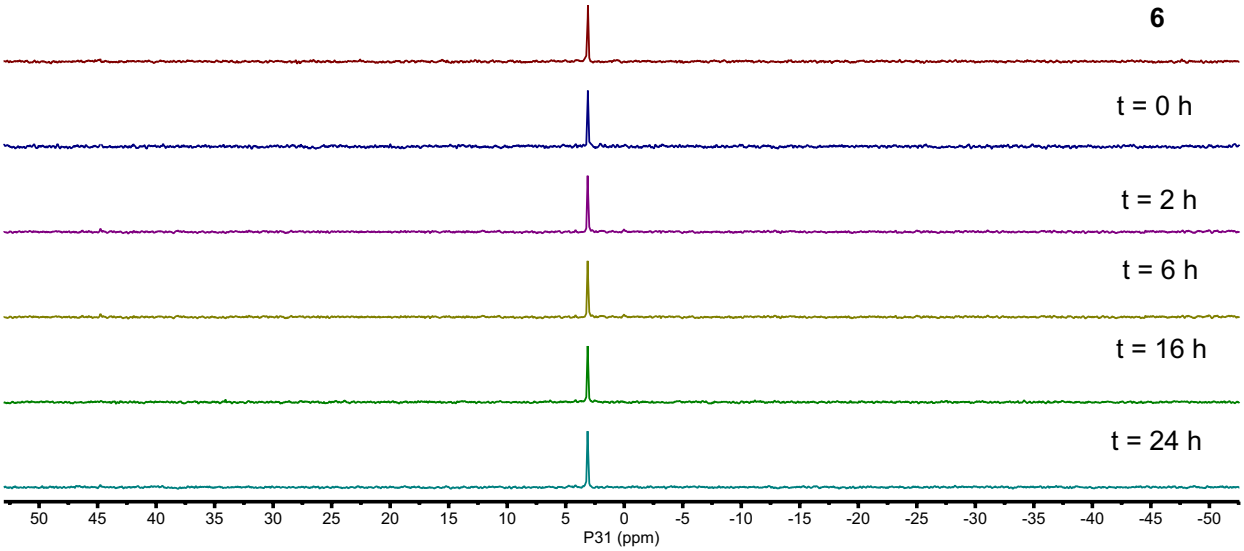

Figure S66. Changes in $^{31}P\{^{1}H\}$ NMR spectra (162 MHz, toluene–d_8) over the course of the semihydrogenation of 40 equiv diphenylacetylene with $NiScL_3$ **6**.

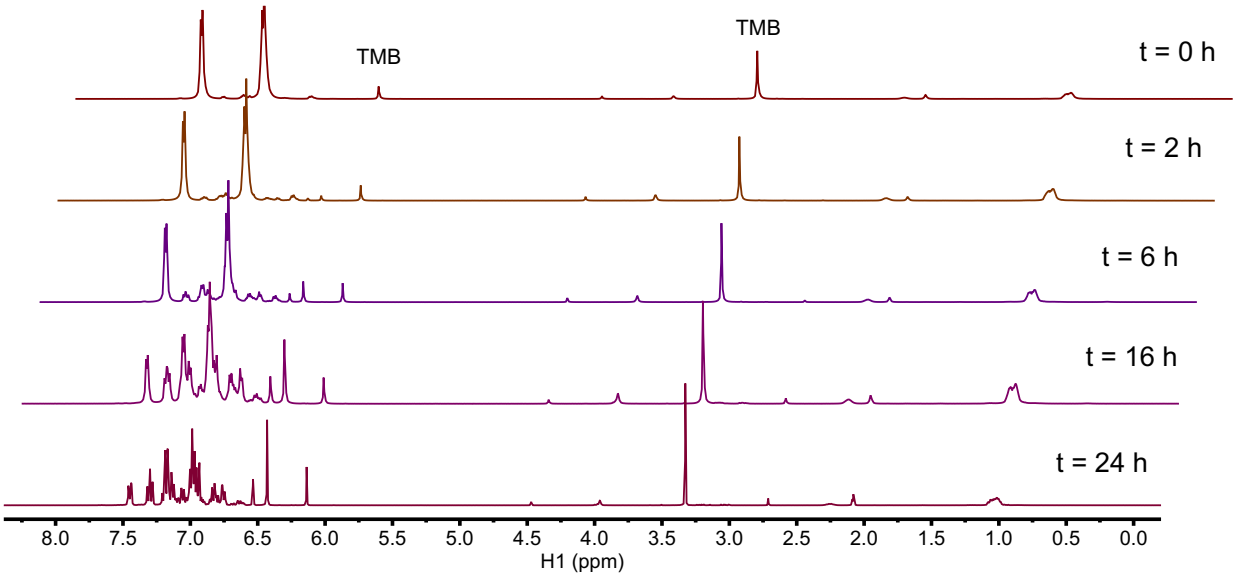

Figure S67. Changes in ^{1}H NMR spectra (400 MHz, toluene–d_8) over the course of the semihydrogenation of 40 equiv diphenylacetylene with $NiScL_3$ **6**.

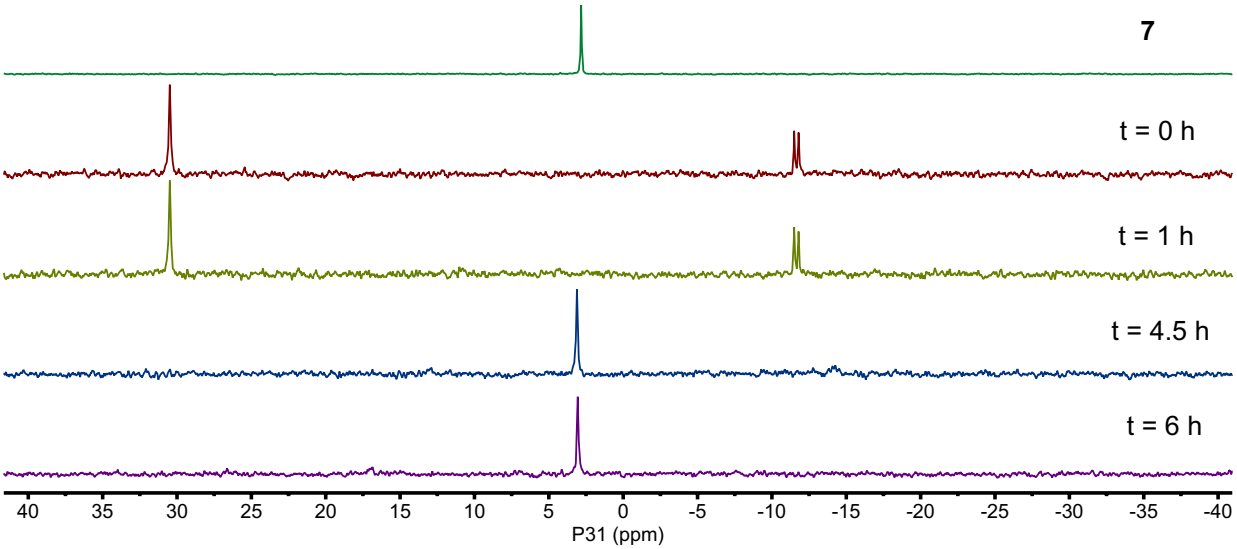

Figure S68. Changes in ^{31}P{^{1}H} NMR spectra (162 MHz, toluene–d_8) over the course of the semihydrogenation of 40 equiv diphenylacetylene with $NiYL_3$ **7**.

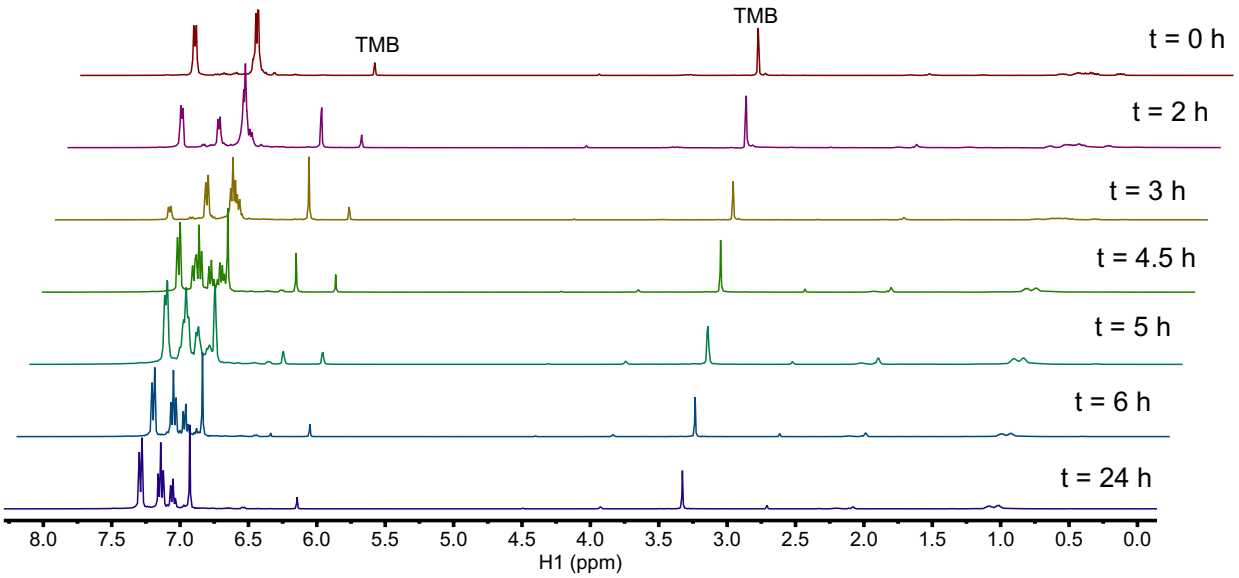

Figure S69. Changes in ^{1}H NMR spectra (400 MHz, toluene–d_8) over the course of the semihydrogenation of 40 equiv diphenylacetylene with NiYL$_3$ **7**.

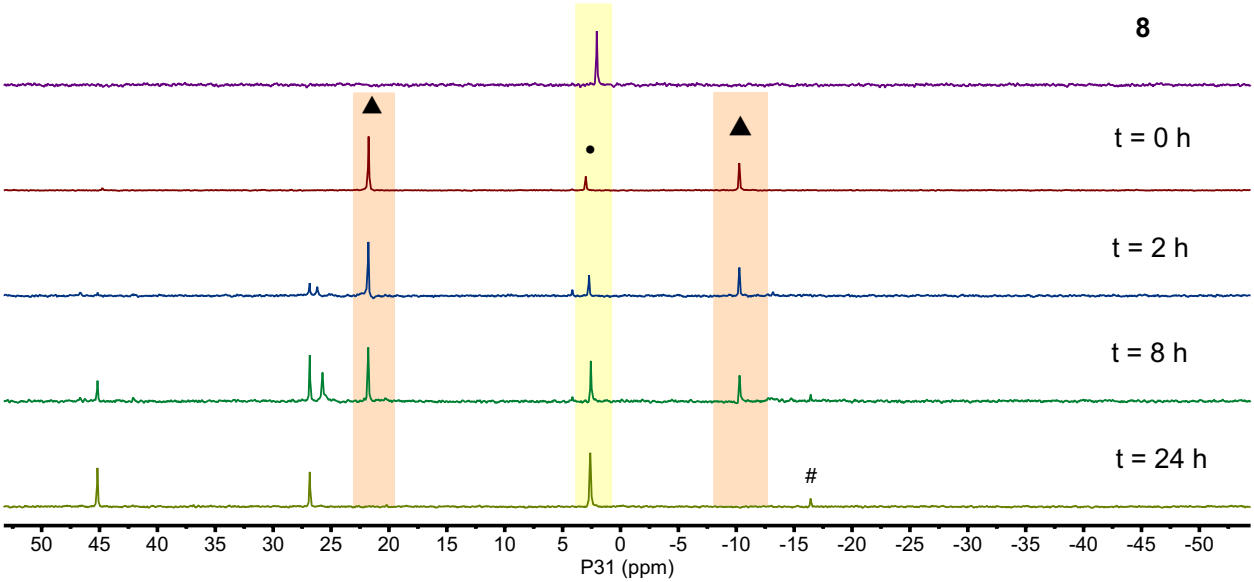

Figure S70. Changes in ^{31}P{^{1}H} NMR spectra (162 MHz, toluene–d_8) over the course of the semihydrogenation of 40 equiv diphenylacetylene with NiLaL$_3$ **8**. Naked Ni-La **8** is marked by a circle (•) and the DPA adduct (**8**-DPA) is marked by a triangle (▲). At 24 h, the only decomposition peak that could be definitively assigned was the singlet at –16.5 ppm, which corresponds to free diisopropylphosphine.[17]

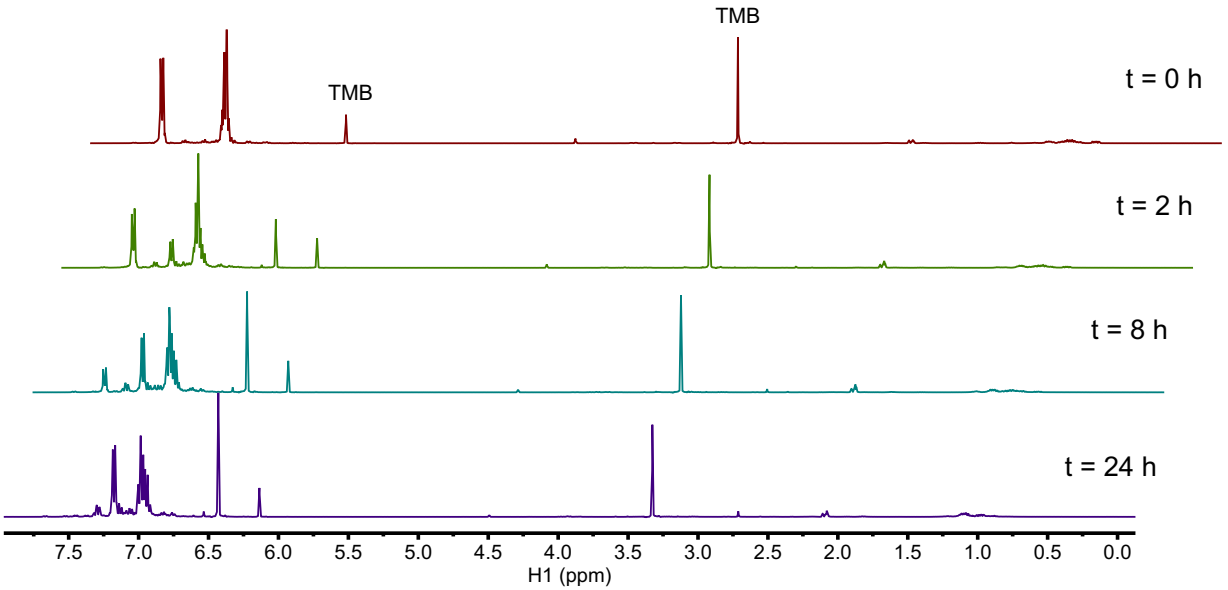

Figure S71. Changes in ^{1}H NMR spectra (400 MHz, toluene–d_8) over the course of the semihydrogenation of 40 equiv diphenylacetylene with NiLaL$_3$ **8**.

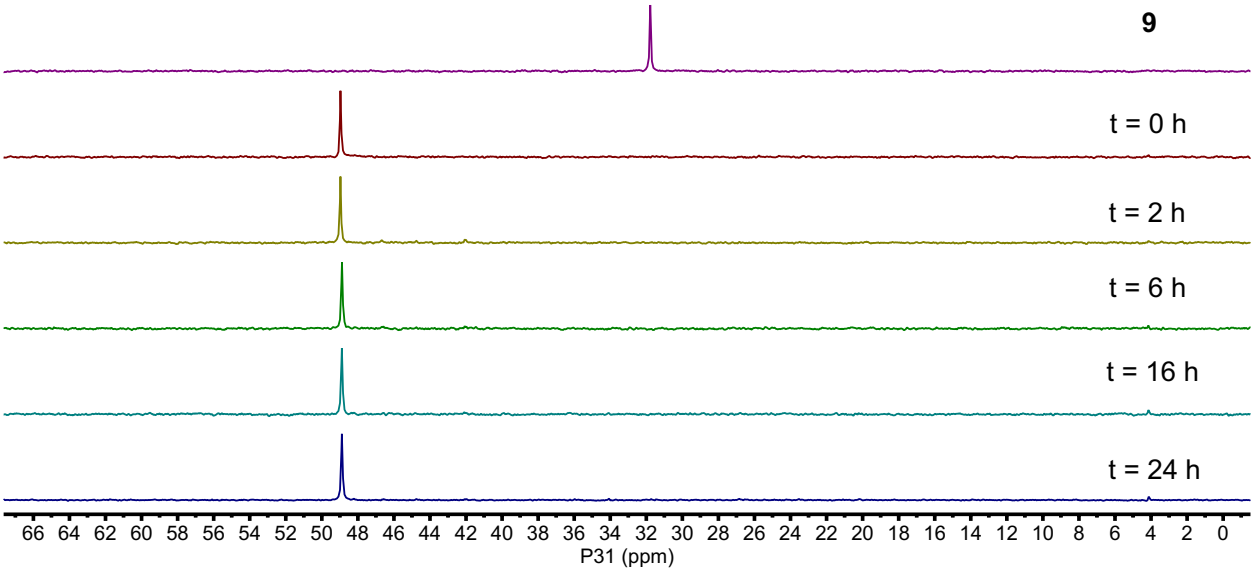

Figure S72. Changes in ^{31}P{^{1}H} NMR spectra (162 MHz, toluene–d_8) over the course of the semihydrogenation of 40 equiv diphenylacetylene with NiGaL$_3$ **9**.

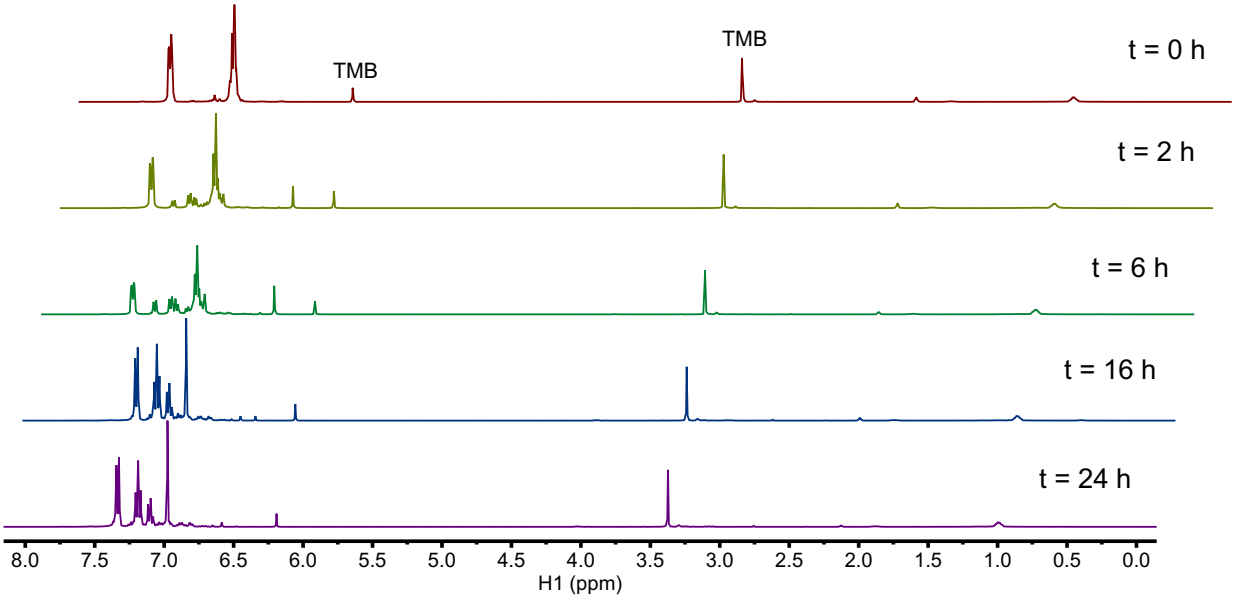

Figure S73. Changes in ^{1}H NMR spectra (400 MHz, toluene–d_8) over the course of the semihydrogenation of 40 equiv diphenylacetylene with NiGaL$_3$ **9**.

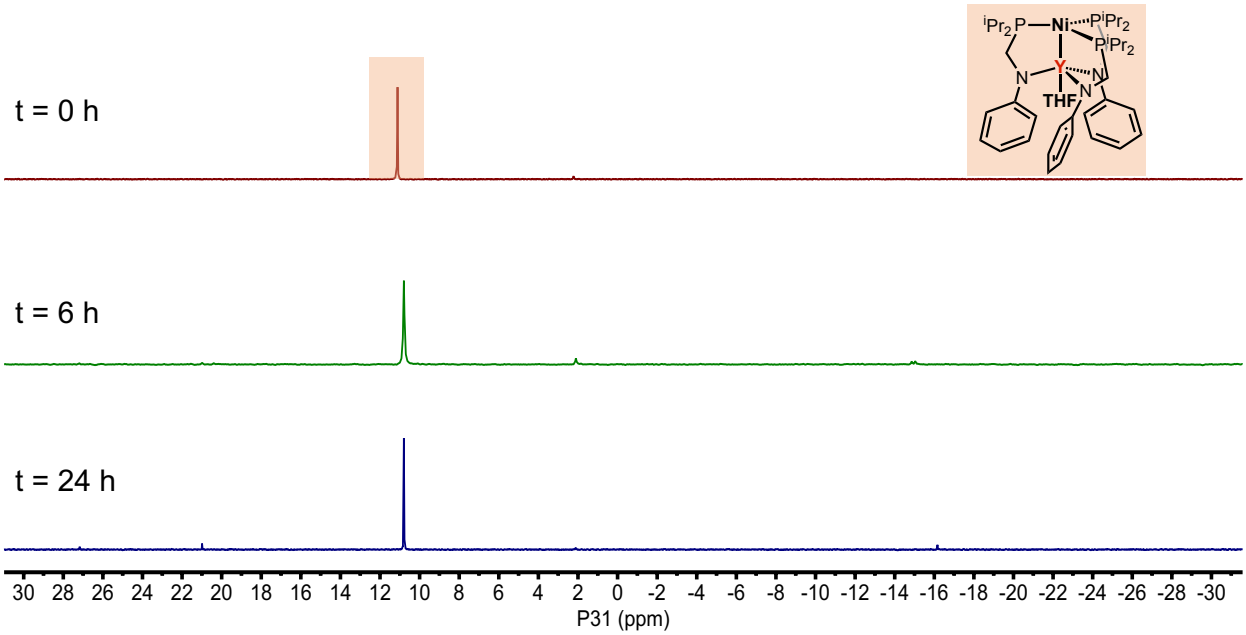

Figure S74. Changes ^{31}P{^{1}H} NMR (162 MHz, THF–d_8) spectra over the course of the semihydrogenation of 40 equiv diphenylacetylene with NiYL$_3$–THF (**7**–THF).

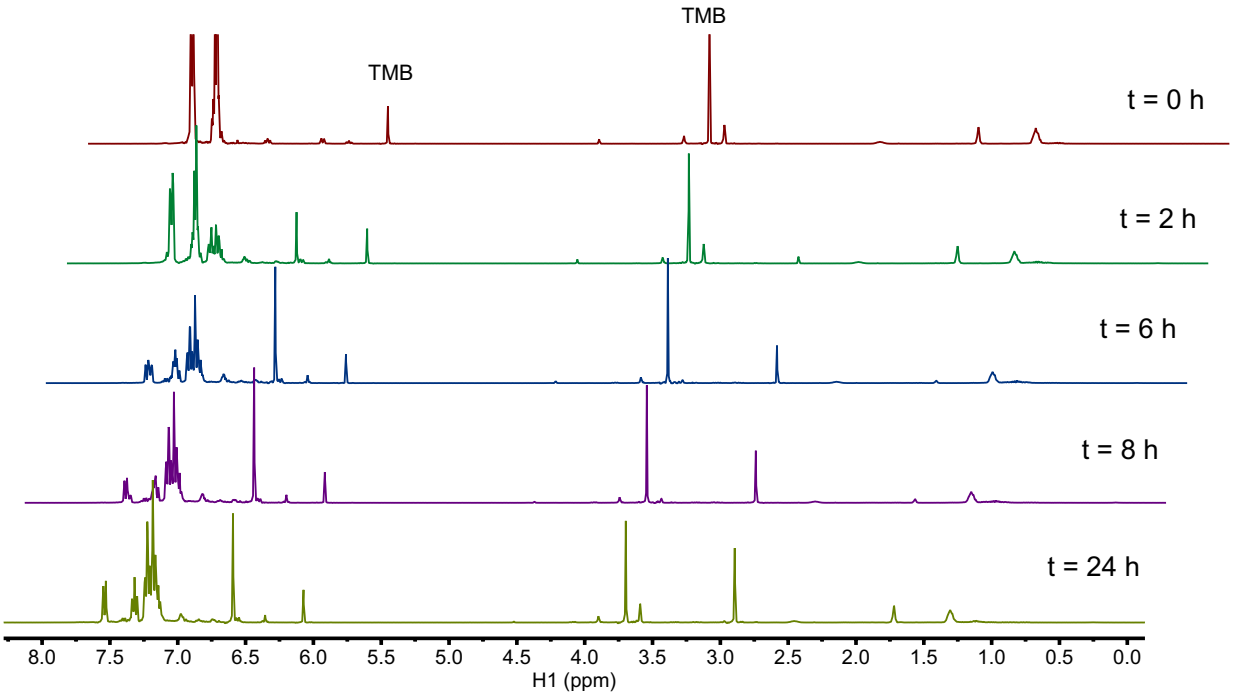

Figure S75. Changes in ^{1}H NMR spectra (400 MHz, THF–d_8) over the course of the semihydrogenation of 40 equiv diphenylacetylene with NiYL$_3$–THF (**7**–THF).

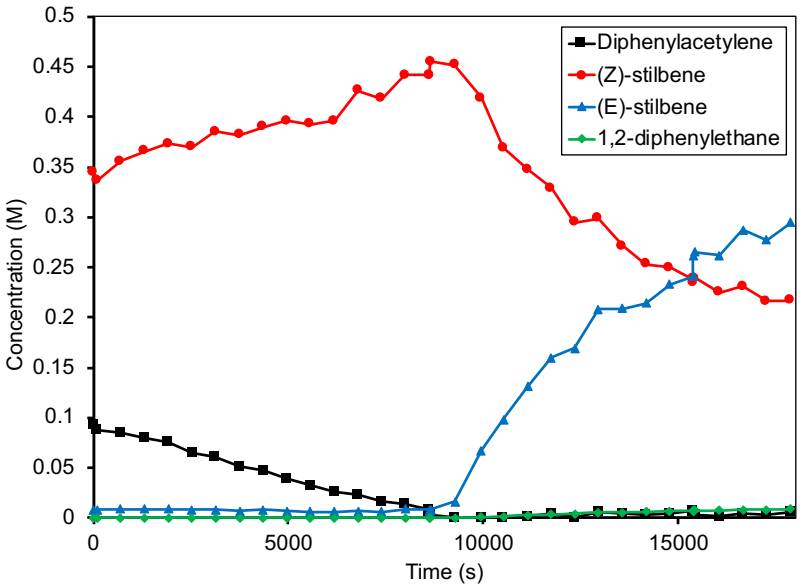

Figure S76. Semihydrogenation reaction time course of 10 equiv DPA and 30 equiv (Z)–stilbene with NiYL$_3$ **7** (equivalents with respect to catalyst).

Low Temperature NMR Catalytic Resting State Studies

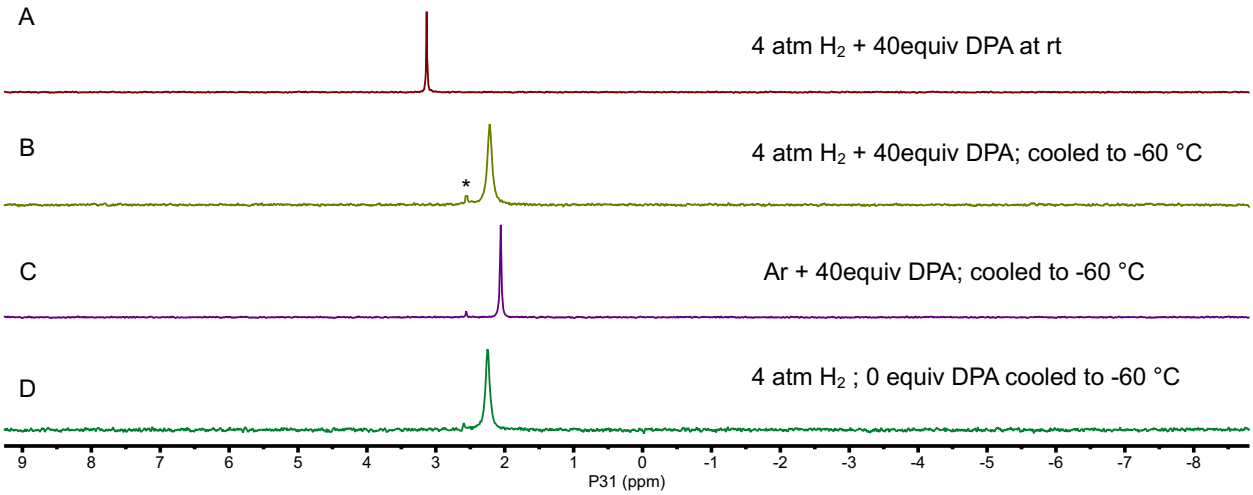

Figure S77. $^{31}P\{^{1}H\}$ NMR spectra overlay (162 MHz, toluene–d_8) of $NiScL_3$ **6** mixed with A) 40 equiv DPA under 4 atm H_2 at rt, B) 40 equiv DPA under 4 atm H_2 at –60 ºC, C) 40 equiv DPA under Ar at –60 ºC, D) 0 equiv DPA under 4 atm H_2 at –60 ºC. At low T, no evidence of a Ni-DPA adduct is observed, indicating $NiScL_3$ **6** does not favor binding of DPA. Residual water in H_2 gas results in the formation of a small amount of Pr_2PCH_2NHPh denoted by an asterisk (*).

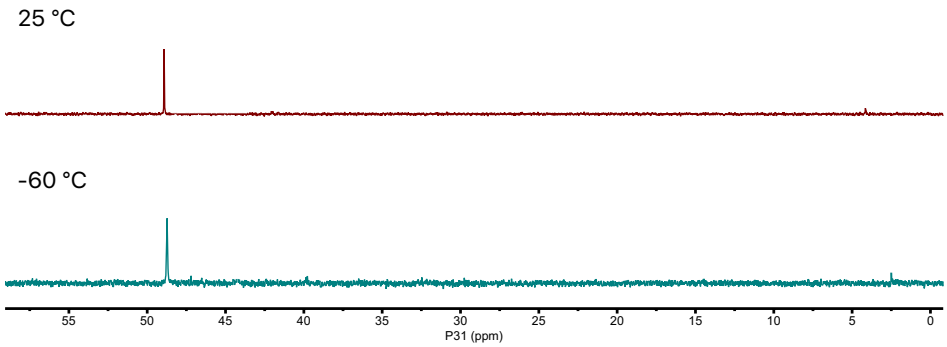

Figure S78. $^{31}P\{^{1}H\}$ NMR spectra overlay (162 MHz, toluene–d_8) of $NiGaL_3$ **9** mixed with A) 40 equiv DPA under 4 atm H_2 at rt and –60 ºC. The NMR data is consistent with **9**–H_2.

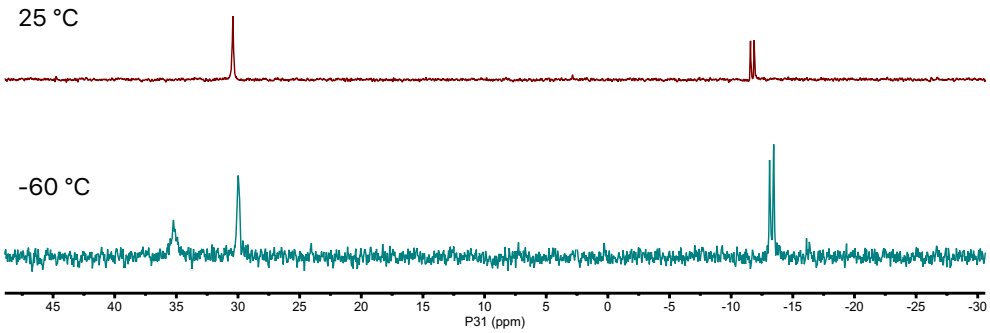

Figure S79. $^{31}P\{^{1}H\}$ NMR spectra overlay (162 MHz, toluene–d_8) of $NiYL_3$ **7** mixed with A) 40 equiv DPA under 4 atm H_2 at rt and –60 ºC. At –60 ºC, **7**–DPA is the major species in solution. Upon cooling, all ligand arms of **7**–DPA become locked leading to three ^{31}P resonances at 32.2, 30.3, and –13.3 (J_{Y-P} = 53.1 Hz) ppm with an integration of 1:1:1.

Deuterium Labeling Studies

A J. Young NMR tube was charged with a solution of *cis*-stilbene (40 µL, 0.224 mmol) and **7** or **9** (0.0056 mmol) in 0.5 mL of toluene. The sample was subjected to one freeze-pump-thaw cycles and D_2 gas (1 atm) was added at 77 K on a high-vacuum line. The sample was warmed to ambient temperature, resulting in 4 atm of D_2 gas. The samples were then heated at 70°C in an oil bath (resulting in 4.6 atm of D_2 gas). After heating for 15 h, a ^2H and ^1H NMR spectra were collected.

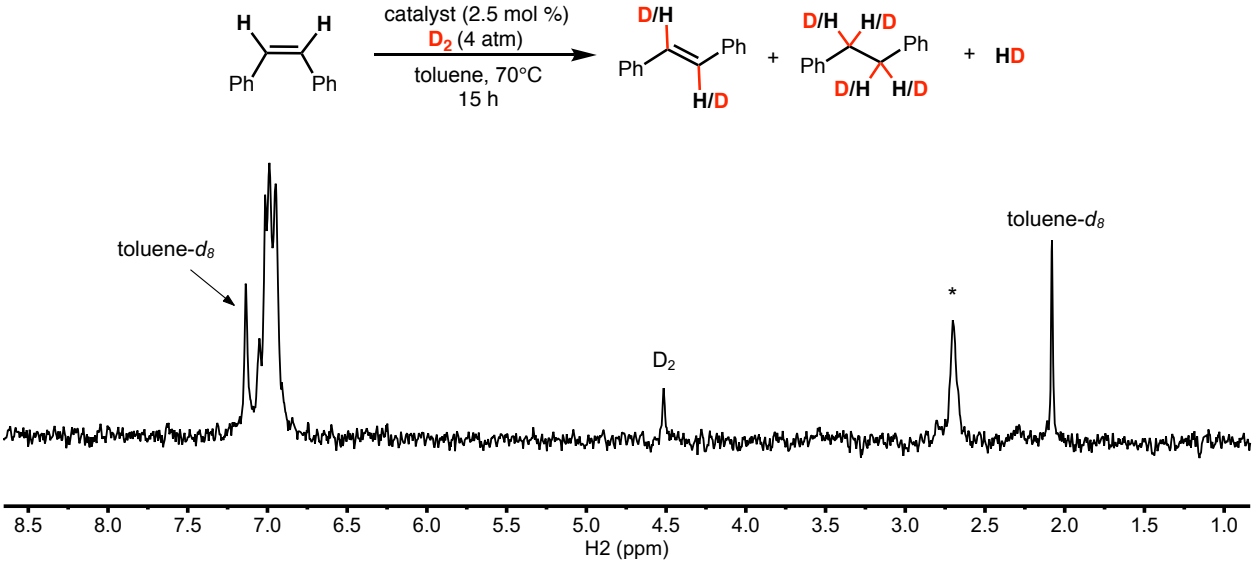

Figure S80. ^2H NMR (61 MHz, toluene) spectrum of **7** (2.5 mol%) and *cis*-stilbene under 4 atm of D_2 after 15 h at 70 °C. (* denotes alkane (sp^3-CD_2) protons).

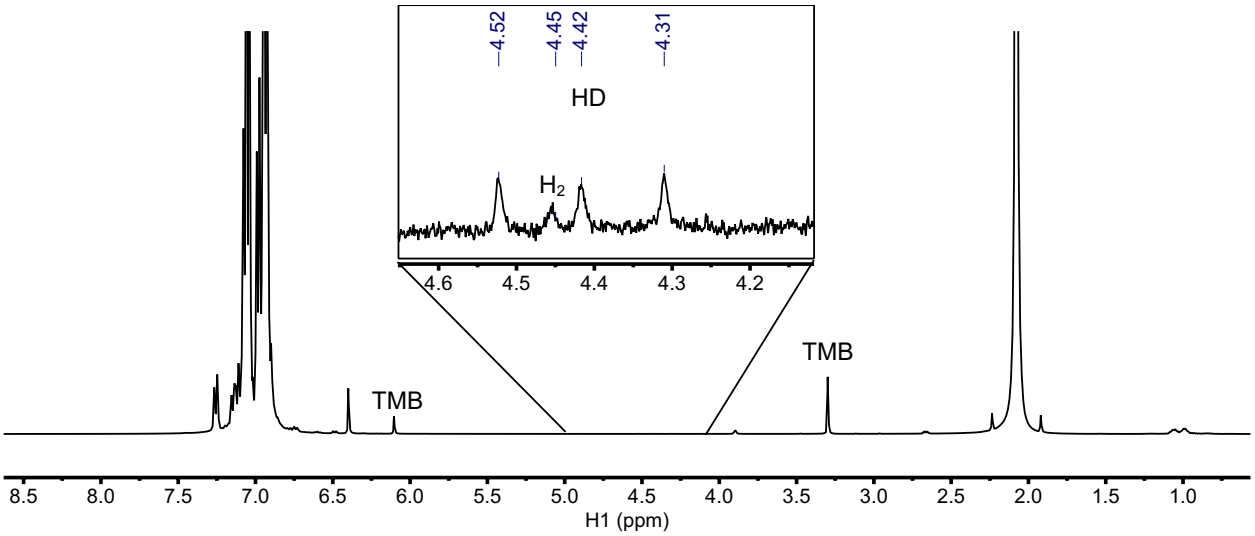

Figure S81. ^1H NMR (61 MHz, toluene) spectrum of **7** (2.5 mol%) and *cis*-stilbene under 4 atm of D_2 after 15 h at 70 °C.

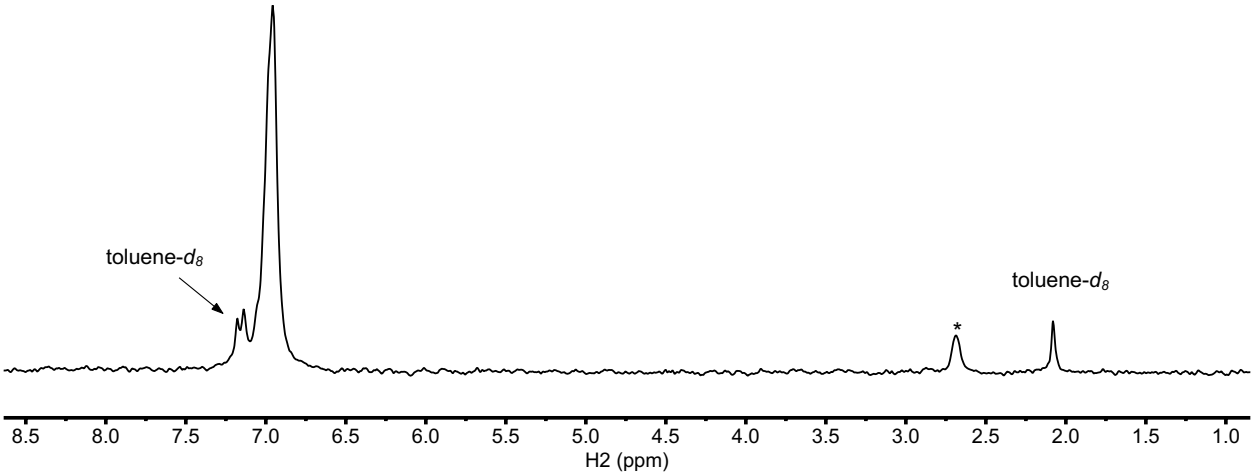

Figure S82. ^{2}H NMR (61 MHz, toluene) spectrum of **9** (2.5 mol%) and *cis*-stilbene under 4 atm of D_2 after 15 h at 70 °C (bottom). (* denotes alkane (sp^3-CD_2) protons).

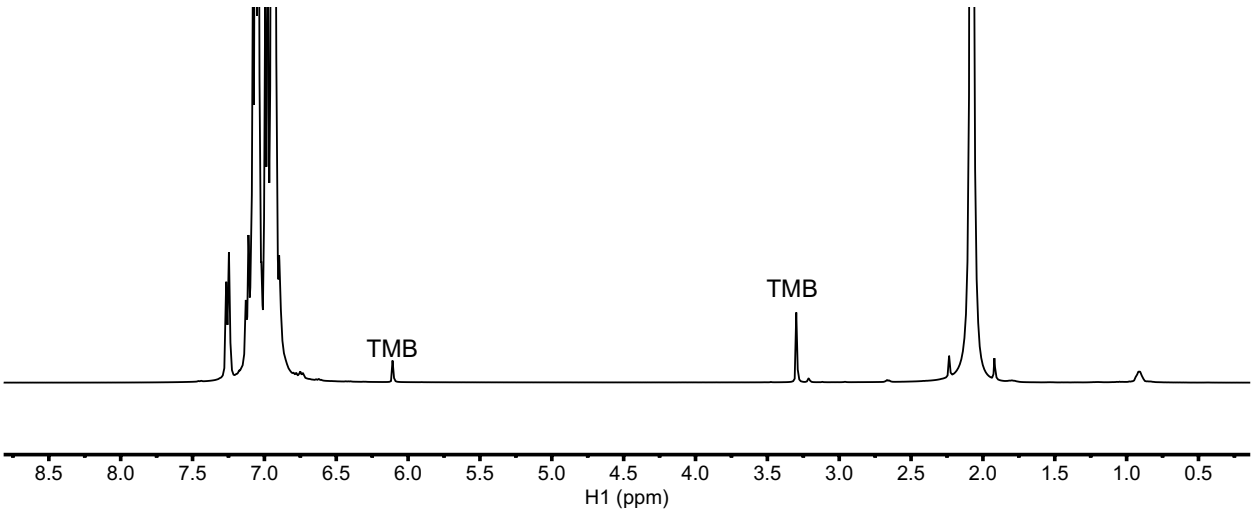

Figure S83. ^{1}H NMR (61 MHz, toluene) spectrum of **9** (2.5 mol%) and *cis*-stilbene under 4 atm of D_2 after 15 h at 70 °C. No free HD or H_2 can be observed at the completion of the experiment due to the strong preference of **9** to bind HD, H_2, and D_2.

H_2 Binding Studies of $NiML_3$ Complexes 6-9

At ambient temperature and 1 atm H_2, NiGa (**9**) cleanly generates the Ni(η^2-H_2) adduct **9**–H_2. Complex **9**–H_2 is characterized by a $^{31}P\{^1H\}$ singlet at 48.5 ppm, and a broad ^1H resonance at –2.03 ppm, which is typical of a Ni(η^2-H_2) adduct (Figure S23 and S24).[18-19] The H-H bond is intact in 9–H_2 as evidenced by a short T_1(min) value of 28(1) ms (500 Hz) (Figure S86).[18] An H−H distance of 0.86 Å (*c.f.* 0.74 Å in free H_2) was determined from the J_{H-D} value of 35 Hz for the corresponding HD adduct (Figure S87).[19] The H_2 binding was reversible as evacuating a solution of **9**−H_2 regenerates **9**.

In contrast, Ni-rare earth compounds **6**, **7**, and **8** show no formation of Ni(η^2-H_2) adducts at ambient temperature and 1 atm H_2.[20] Therefore, to maximize H_2 binding, samples of **6**, **7**, and **8** in toluene−d_8 and THF−d_8 were subjected to 4 atm H_2 (at room temperature) and characterized *in situ* by low-temperature NMR spectroscopy. Of note, the low T NMR spectra for **6**, **7**, and **8** have notably weaker signal intensities due to their generally poor solubility in non-coordinating solvents.

At −83 °C and 4 atm H_2 in toluene–d_8, no metal bound H_2 species can be observed for Ni-Sc **6** or Ni-Y **7** by either ^{31}P or ^1H NMR (Figures S88 and S91). As both **6** and **7** can catalyze hydrogenation reactions, it is evident that these complexes indeed bind H_2, however the study of any H_2 adducts can't be performed using our available resources. However, in THF−d_8, an equilibrium between Ni-Sc **6** and a new species was observed at −80 °C in an approximate 1:1.4 ratio based on the appearance of two broad ^{31}P peaks at 1.1 and 25.1 ppm, respectively (Figure S89). A similar equilibrium is observed between **7**−THF (10.4 ppm) and a new species (18.9 ppm) with an approximate 1:0.8 ratio (Figure S92). Examination of the ^1H NMR spectra of **6** and **7**–THF each contain a broad resonance at –2.1 and –1.2 ppm, respectively, suggestive of Ni(η^2-H_2) adducts (Figures S90 and S93). For both **6** and **7**–THF, T_1(min) relaxation time measurements could not be obtained due to the broadness of the resonance at –83 °C and lack of an observable H_2 resonance in the ^1H NMR spectra at higher temperatures.

Complex Ni-La **8** serves as an outlier to the other Ni–rare earth bimetallic complexes. In toluene–d_8, cooling to −50 °C under 4 atm H_2 leads to an equilibrium between the C_3 symmetric Ni-La **8** and an asymmetric species in both the $^{31}P\{^1H\}$ and ^1H NMR spectra (Figures S94 and S95). The species is best described by a triplet in the $^{31}P\{^1H\}$ NMR spectrum at 27.9 and a broad singlet at –2.1 ppm which integrate 1P to 2P, respectively (Figure S98). It's worth noting that the same species is observed with Ni-La **8** under an Ar atmosphere, which suggests that the appearance of this species is not attributed to H_2 binding. We propose that this asymmetry arises from the formation of a η^2 C_{ipso}-N bonding interaction between NPh and La, which is observed in the solid state structure of **8**' (Figure S35). At room temperature, this interaction rapidly exchanges between the 3 aryl rings, leading to the appearance of a C_3-symmetric species (Figure S99). Of note, cooling to –83 °C, leads to the appearance of another sharper singlet at 4.0 ppm. At this time, we do not know what NiLa species leads to this resonance, however, because we can observe the same $^{31}P\{^1H\}$ resonance signal under Ar, the peak is not related to the binding of H_2 (Figure S100). In THF–d_8, the ^{31}P resonance shifts 6.5 ppm downfield to 10.7 ppm upon cooling and is identical whether under 4 atm H_2 or Ar (Figures S101). Therefore, the shift in $^{31}P\{^1H\}$ resonance is associated with THF binding to form **8**–THF rather than H_2 binding. By ^1H NMR, a discrete bound H_2 proton resonance is not observed indicating at the conditions attainable, an **8**-H_2 species can't be observed (Figure S102).

Overall, the strength of the H_2 interaction with the Ni(0) center decreases in the order, **9** >> **6** > **7** > **8**. Since the Ni center is more electron-deficient in NiGa **9** than in the Ni-rare earth complexes, this family of compounds adheres to the trend that was previously established for bimetallic Ni-group 13 complexes.[20-21] Namely, the more Lewis acidic metalloligands lead to more stable and easily accessible Ni(η^2-H_2) adducts.

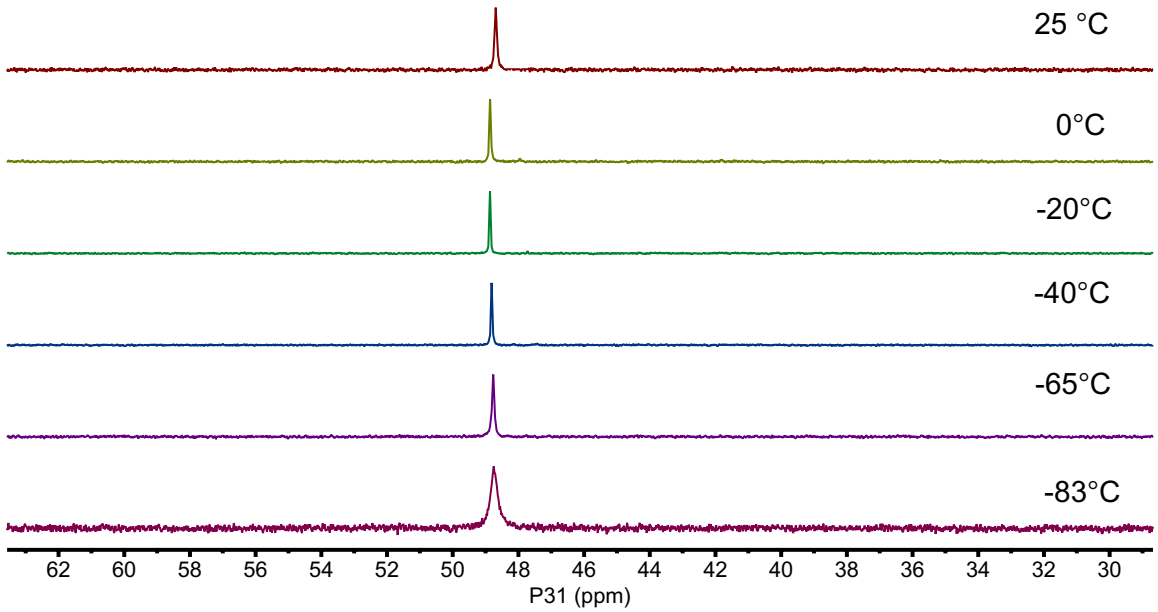

Figure S84. Variable temperature $^{31}P\{^{1}H\}$ NMR (162 MHz, toluene–d_8) spectra of NiGa **9** under 1 atm H_2 at rt. The absence of any substantial shift in the ^{31}P resonance indicates all **9** in solution is fulling binding H_2 to form **9**–H_2.

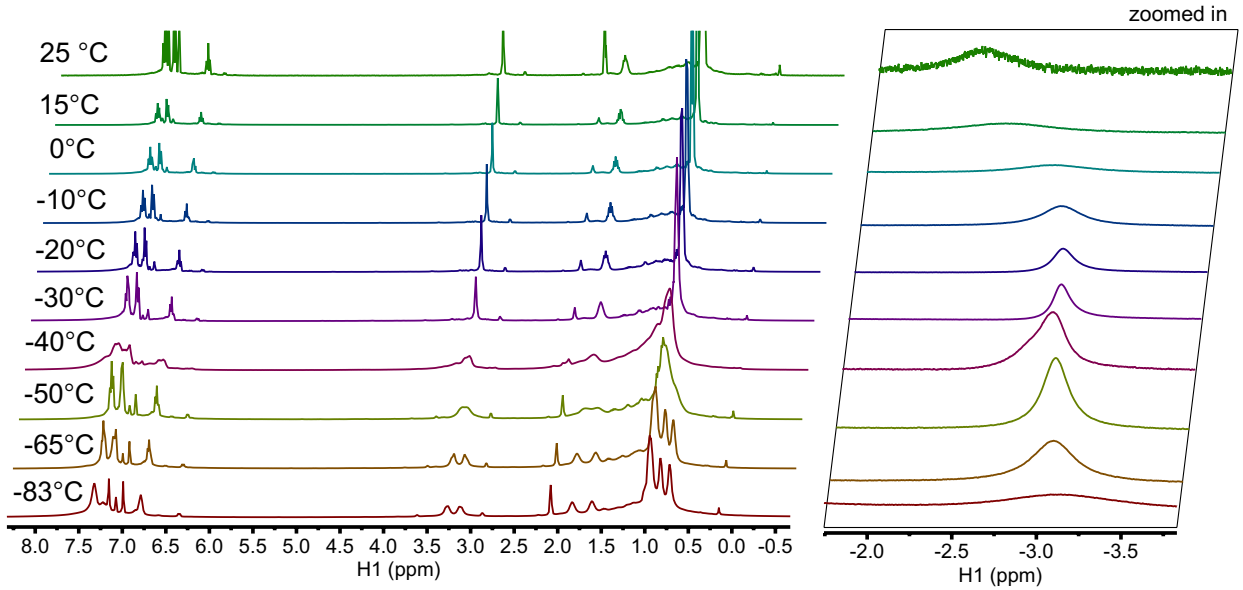

Figure S85. Variable temperature $^{1}H\{^{31}P\}$ NMR (400 MHz, toluene–d_8) spectra of NiGa **9** under 1 atm H_2 (at rt) cooled to –83°C.

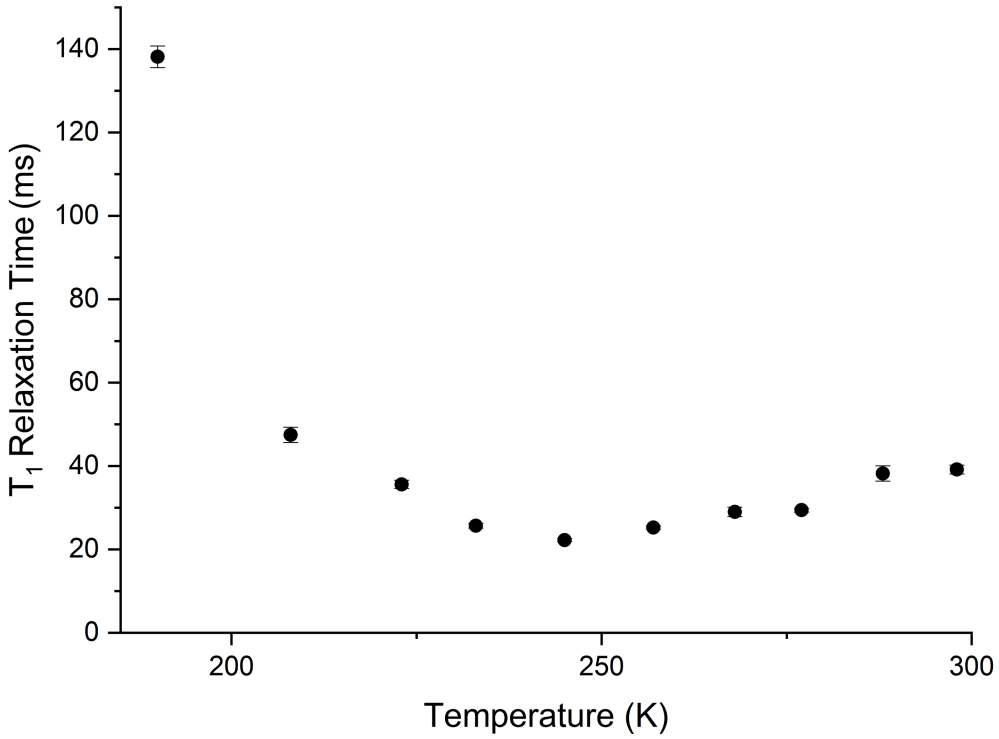

Figure S86. Plot of the T_1 relaxation times of the bound H_2 resonance of **9**–H_2 at various temperatures from 180 K to 298 K (400 MHz, toluene–d_8).

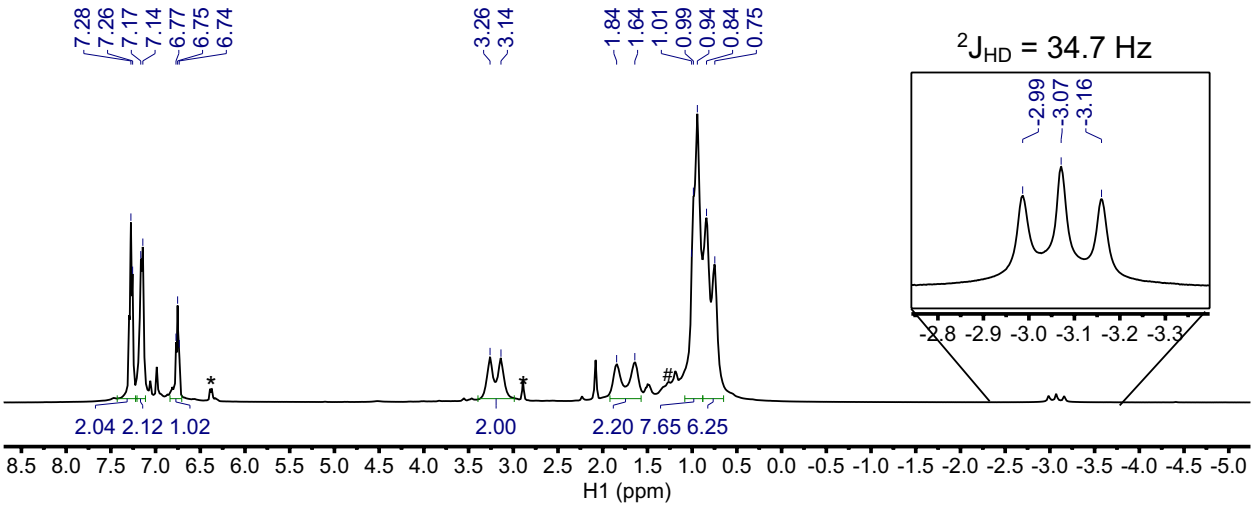

Figure S87. $^1H\{^{31}P\}$NMR (400 MHz, toluene–d_8) spectrum of NiGa **9** under 1 atm HD cooled to –62 °C to observe in situ **9**–HD. No scrambling of HD to H_2 and D_2 was observed.

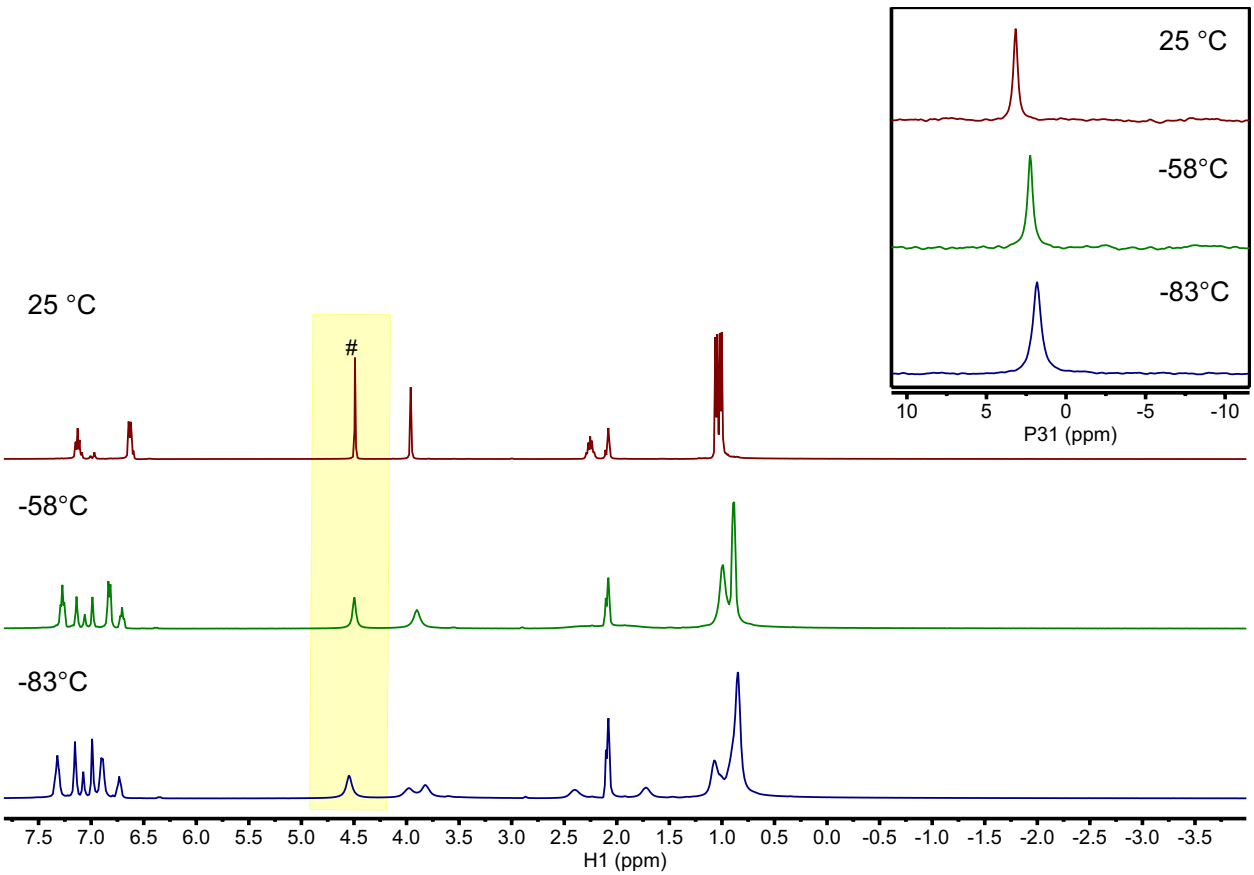

Figure S88. Variable temperature $^{1}H\{^{31}P\}$NMR and $^{31}P\{^{1}H\}$ NMR (inset) (400 MHz (^{1}H), 162 MHz (^{31}P), toluene–d_8) spectra of NiSc **6** under 4 atm H_2 (at rt) cooled to 190 K. The ^{1}H resonance of free H_2 in toluene–d_8 is denoted by a pound sign (#). Upon cooling, there is no shift in the proton resonance of H_2 or the observation of a Ni(H_2) adduct resonance which would indicate strong binding with H_2. In addition, upon cooling, little variation in the ^{31}P NMR resonance is observed, indicating that any H_2 binding taking place is too weak to observe with the achievable conditions.

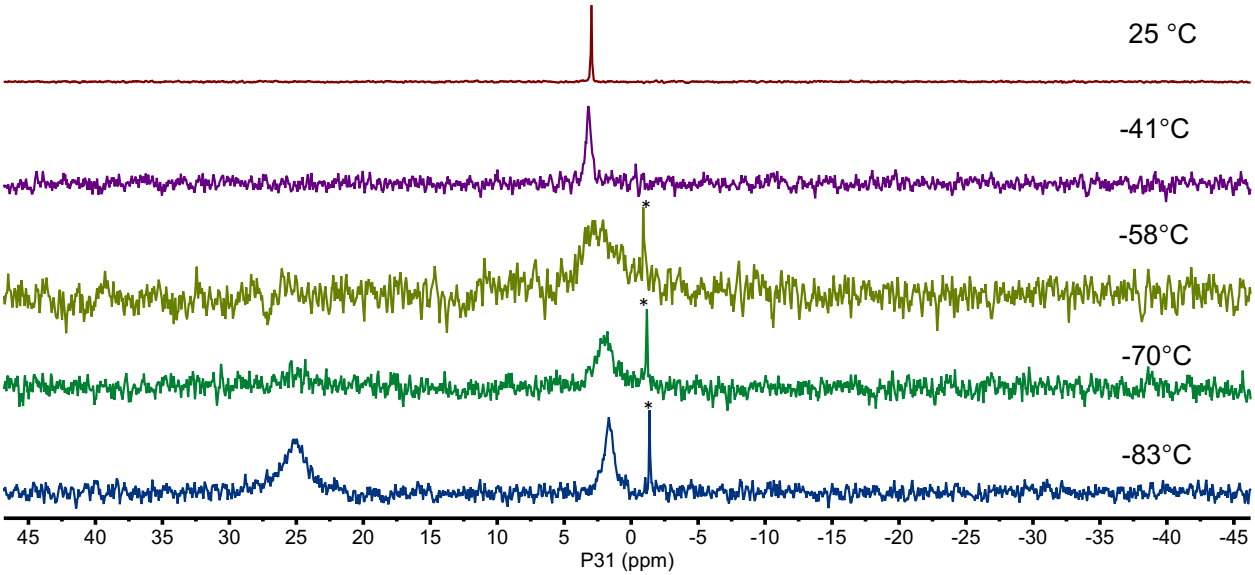

Figure S89. Variable temperature $^{31}P\{^{1}H\}$ NMR (162 MHz, THF–d_8) spectra of NiSc **6** under 4 atm H_2 (at rt) cooled to 190 K. Initially, the ^{31}P resonance broadens upon cooling. At –83°C, the H_2 exchange becomes slower such that a slow exchange regime is achieved in which both **6** and **6**–(H_2) can be observed. In turn, a discrete bound **6**–(H_2) phosphorus resonance (25.0 ppm) appears at –83°C. Residual water in H_2 gas results in the formation of a small amount of Pr_2PCH_2NHPh denoted by an asterisk (*), which is only observable at low temperatures where the complex signals have greatly broadened.

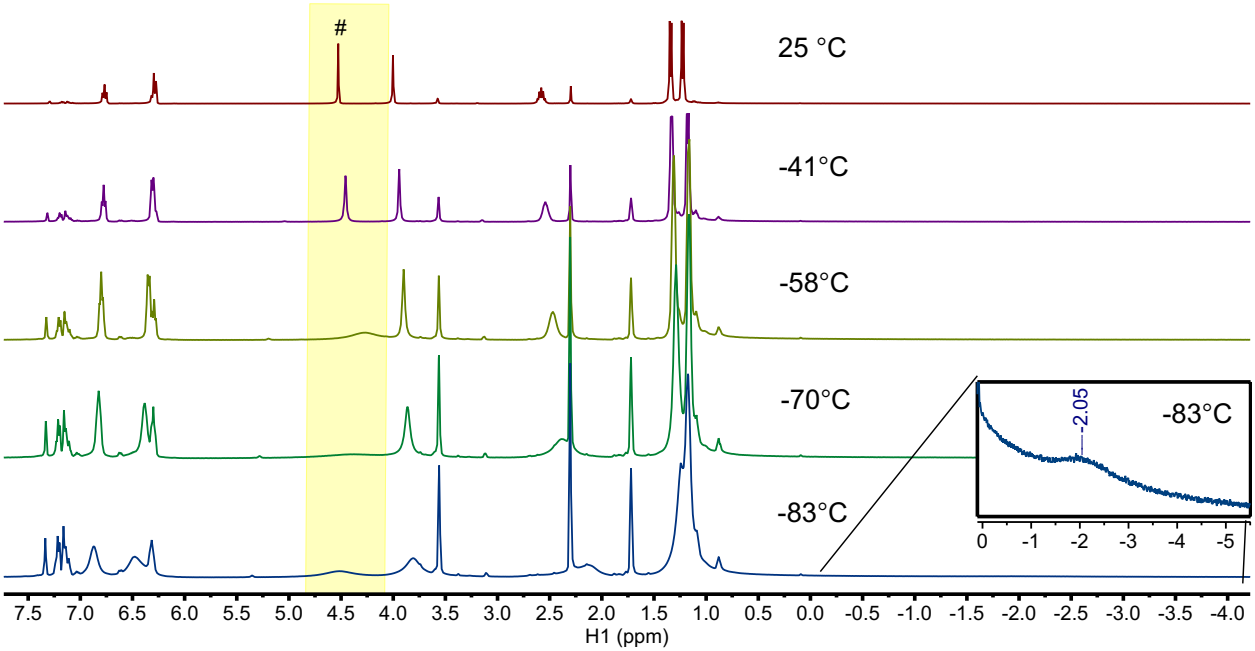

Figure S90. Variable temperature $^{1}H\{^{31}P\}$ NMR (400 MHz, THF–d_8) spectra of NiSc **6** under 4 atm H_2 at rt. The resonance of free H_2 (marked by an (#) at 4.55 ppm) broadens and shifts slightly upfield upon cooling to –83°C. At –83°C, the resonance shifts back downfield to that of free H_2 (4.55 ppm) and a discrete bound **6**-H_2 proton resonance (–2.1 ppm) appears. A reliable T_1 value could not be obtained due to the broadness of the bound H_2 resonance at 190 K.

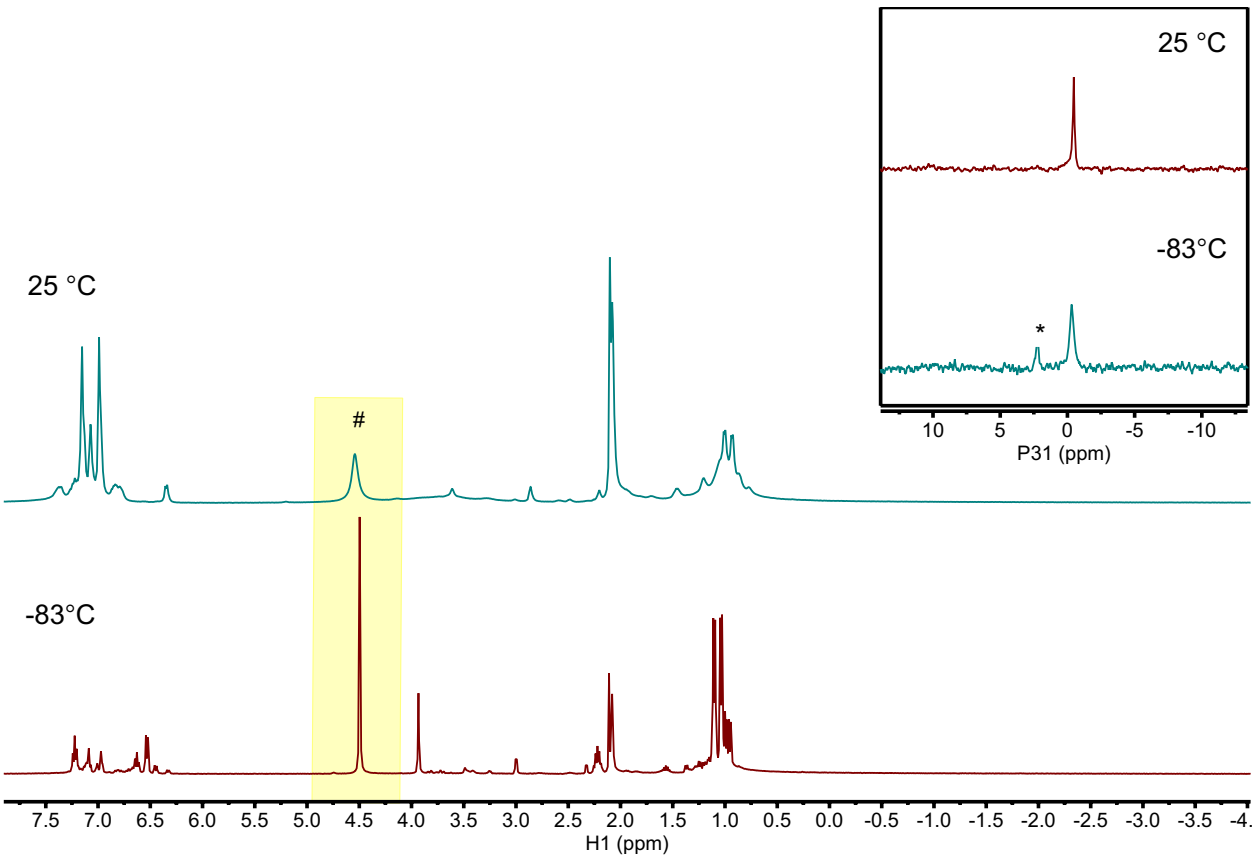

Figure S91. $^{1}H\{^{31}P\}$NMR and ^{31}P NMR (inset) (400 MHz (^{1}H), 162 MHz (^{31}P), toluene–d_8) overlay of NiY **7** under 4 atm H_2 (at rt) cooled to 190 K. The ^{1}H resonance of free H_2 in toluene–d_8 is denoted by a pound sign (#). Upon cooling, there is no shift in the proton resonance of H_2 or the observation of a Ni(H_2) adduct resonance which would indicate strong binding with H_2. Furthermore, upon cooling, little variation in the ^{31}P NMR resonance is observed, indicating that any H_2 binding taking place is too weak to observe with the achievable conditions. Signals for **7** appear weak in spectra due to its poor solubility in aromatic solvents. Residual water in H_2 gas results in the formation of a small amount of Pr_2PCH_2NHPh denoted by an asterisk (*), which is only observable at low temperatures where the complex signals have greatly broadened.

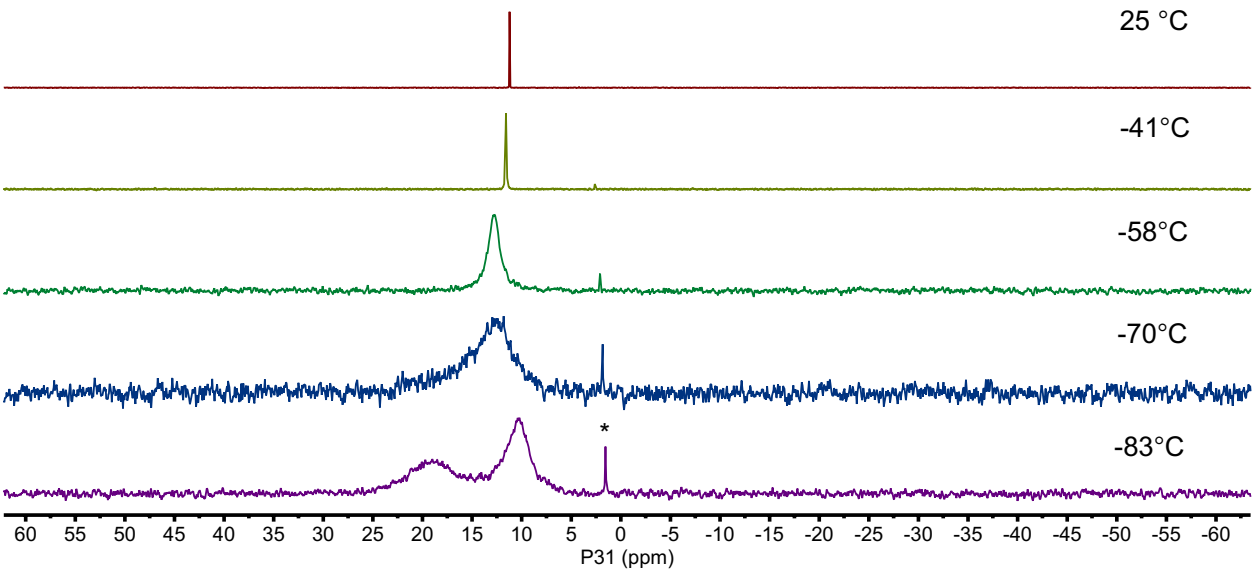

Figure S92. $^{31}P\{^{1}H\}$ NMR (162 MHz, THF–d_8) overlay of **7**–THF 4 atm H_2 (at rt) cooled to –83°C. Initially, the ^{31}P resonance broadens upon cooling. At –83°C, the H_2 exchange becomes slower such that a slow exchange regime is achieved in which both **7**–THF and (H_2)**7**–THF can be observed. In turn, a discrete bound (H_2)**7**–THF phosphorus resonance (19.0 ppm) appears at –83°C. Residual water in H_2 gas results in the formation of a small amount of Pr_2PCH_2NHPh denoted by an asterisk (*), which is only observable at low temperatures where the complex signals have greatly broadened.

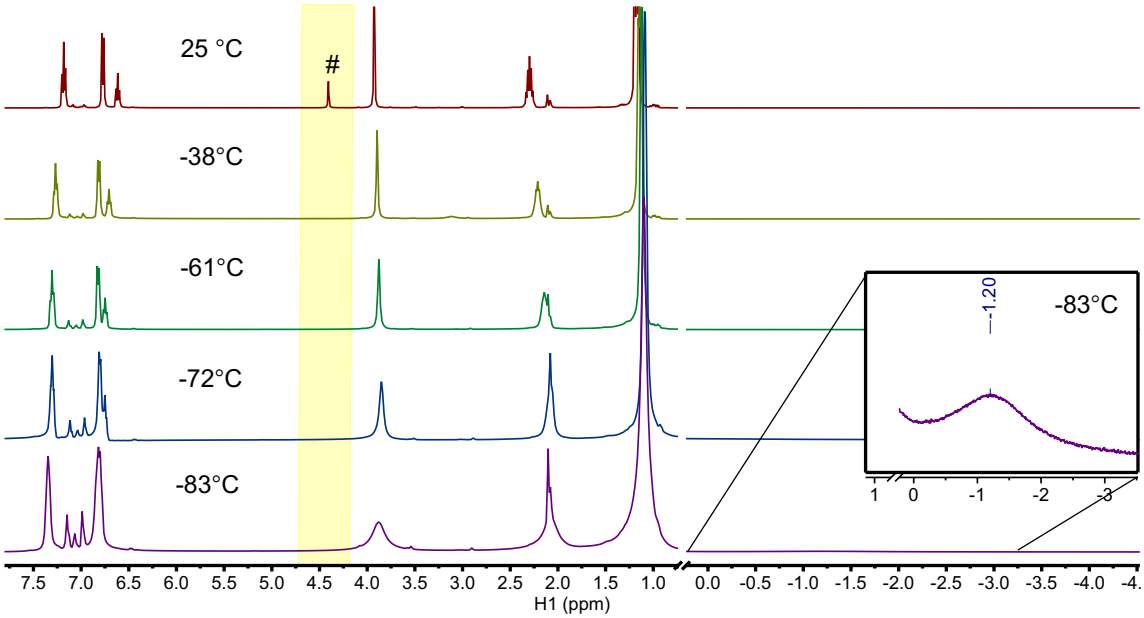

Figure S93. Variable temperature $^{1}H\{^{31}P\}$ NMR (400 MHz, THF–d_8) spectra of **7**–THF under 4 atm H_2 at rt. The ^{1}H resonance of free H_2 in toluene–d_8 is denoted by a pound sign (#). Initially, the ^{1}H resonance disappears upon cooling due to fast exchange of H_2 with **7**–THF. At –83°C, the H_2 exchange becomes slower such that a slow exchange regime is achieved in which (H_2)**7**–THF can start to be observed. In turn, a discrete bound (H_2)**7**–THF proton resonance (–1.2 ppm) appears at –83°C. A reliable T_1 value could not be obtained due to the broadness of the bound H_2 resonance at 190 K.

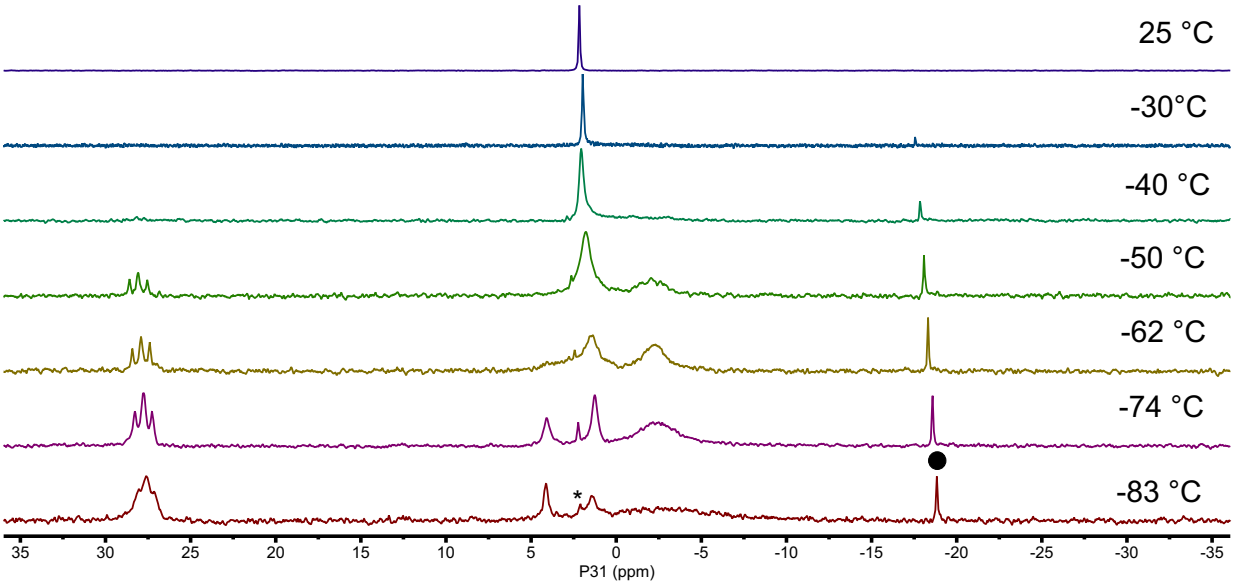

Figure S94. Variable temperature $^{31}P\{^{1}H\}$ NMR (162 MHz, toluene–d_8) spectra of NiLa **8** under 4 atm H_2 (at rt) cooled to –83°C. The spectra of **8** becomes asymmetric upon cooling, but returns to C_3 symmetry upon warming back to rt. An in-depth discussion of the VT profile can be found at the beginning of this section. Residual water in H_2 gas results in the formation of a small amount of Pr_2PCH_2NHPh is denoted by an asterisk (*), which is only observable at low temperatures where the complex signals have greatly broadened. In addition, isopropyl phosphine, a decomposition product for **8**, is denoted by a circle (•), which is only largely observable at low temperatures where the complex signals have greatly broadened.

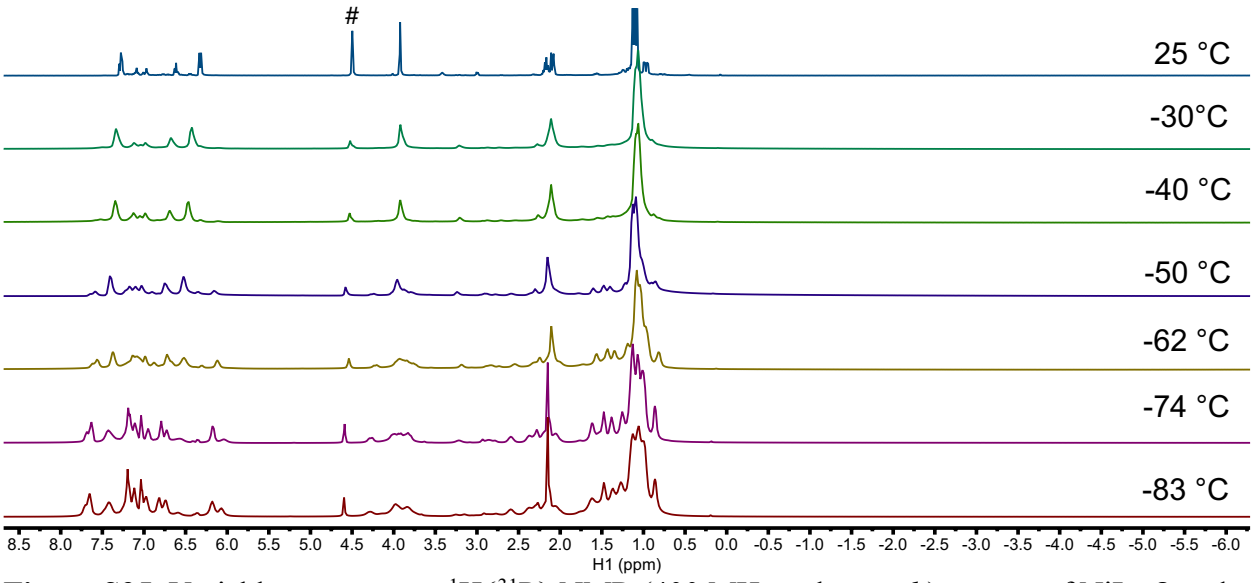

Figure S95. Variable temperature $^{1}H\{^{31}P\}$ NMR (400 MHz, toluene–d_8) spectra of NiLa **8** under 4 atm H_2 at rt. The spectra of **8** becomes asymmetric upon cooling, but returns to C_3 symmetry upon warming back to rt. No discrete bound H_2 proton resonance is observed and the free H_2 ^{1}H resonance does not shift. An in-depth discussion of the VT profile can be found at the beginning of this section.

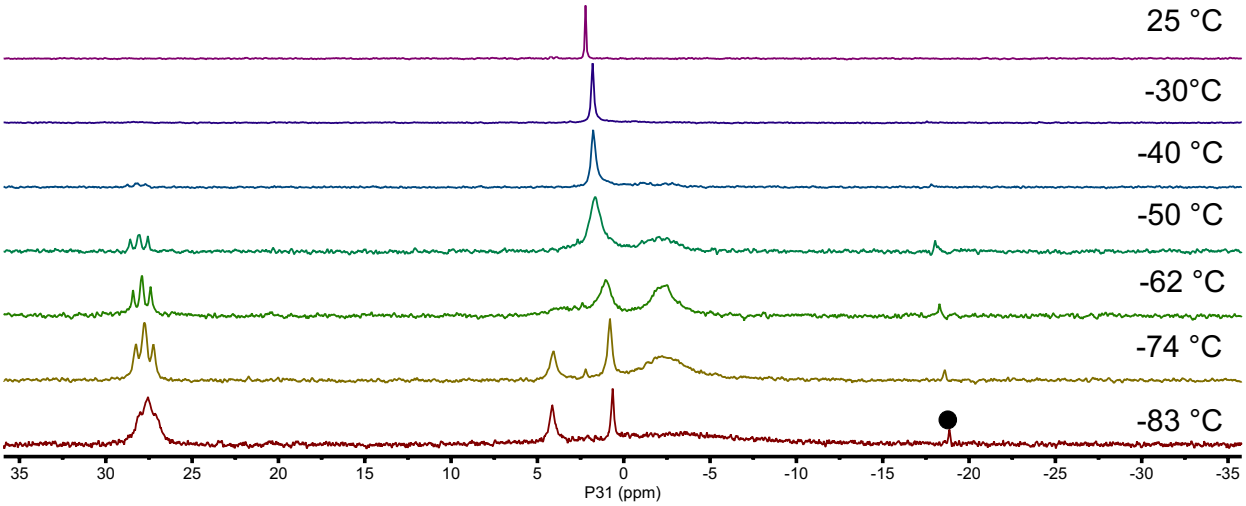

Figure S96. Variable temperature $^{31}P\{^{1}H\}$ NMR (162 MHz, toluene–d_8) spectra of NiLa **8** under Ar at rt. The spectra of **8** becomes asymmetric upon cooling, but returns to C_3 symmetry upon warming back to rt. An in-depth discussion of the VT profile can be found at the beginning of this section. Residual water in H_2 gas results in the formation of a small amount of Pr_2PCH_2NHPh is denoted by an asterisk (*), which is only observable at low temperatures where the complex signals have greatly broadened. In addition, isopropyl phosphine, a decomposition product for **8**, is denoted by a circle (•), which is only largely observable at low temperatures where the complex signals have greatly broadened.

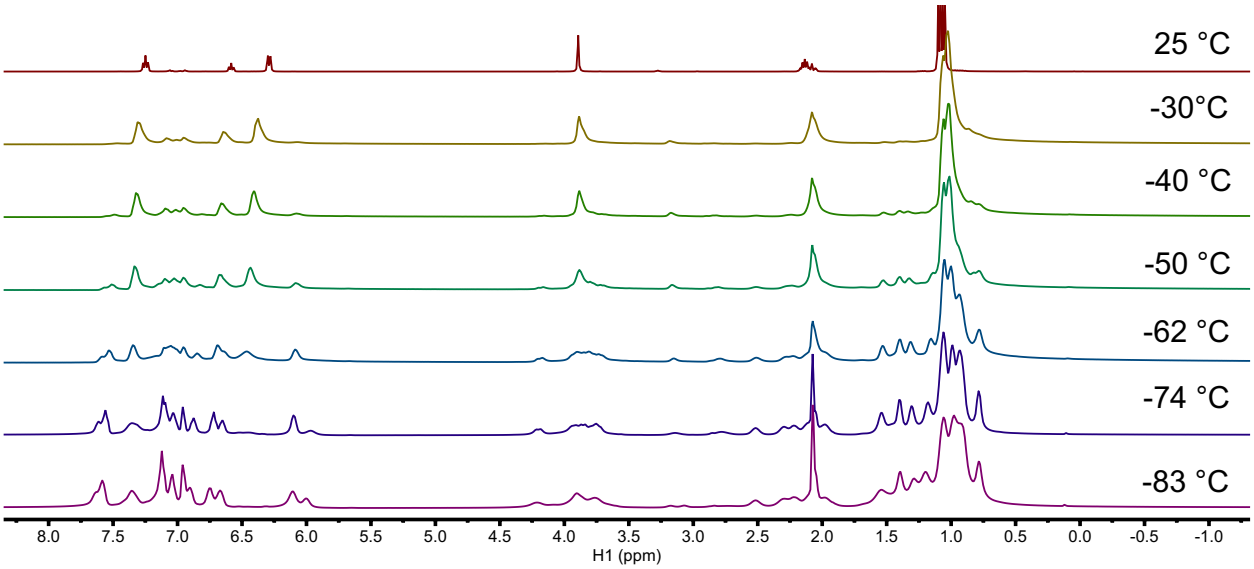

Figure S97. Variable temperature $^{1}H\{^{31}P\}$ NMR (400 MHz, toluene–d_8) spectra of NiLa **8** under Ar at rt. The spectra of **8** becomes asymmetric upon cooling, but returns to C_3 symmetry upon warming back to rt. An in-depth discussion of the VT profile can be found at the beginning of this section.

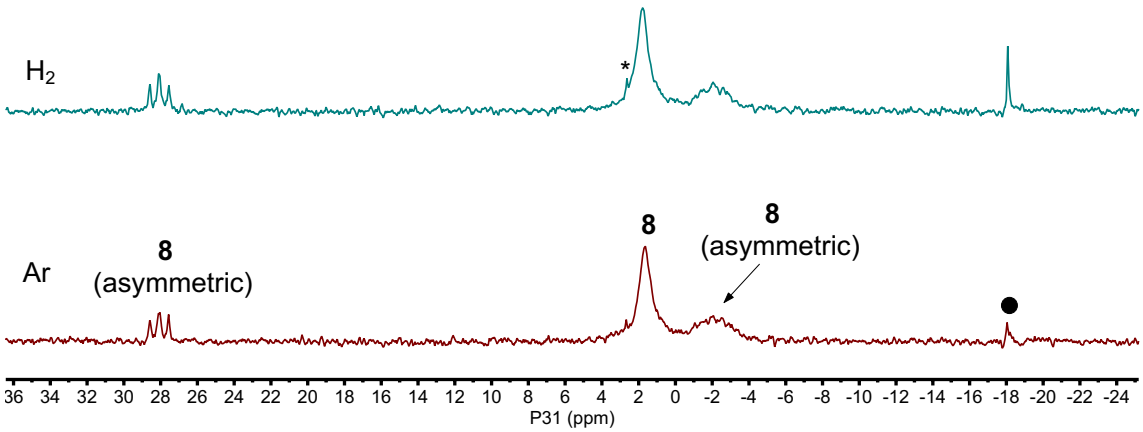

Figure S98. $^{31}P\{^{1}H\}$ NMR (162 MHz, toluene–d_8) spectra of **8** under Ar and 4 atm H_2 (at rt) cooled to –50 °C. The similarity between the two spectra indicates that H_2 binding does not contribute to any of the observed species. Isopropylphosphine, a decomposition product for **8**, is denoted by a circle (•). Residual water in H_2 gas results in the formation of a small amount of Pr_2PCH_2NHPh is denoted by an asterisk (*).

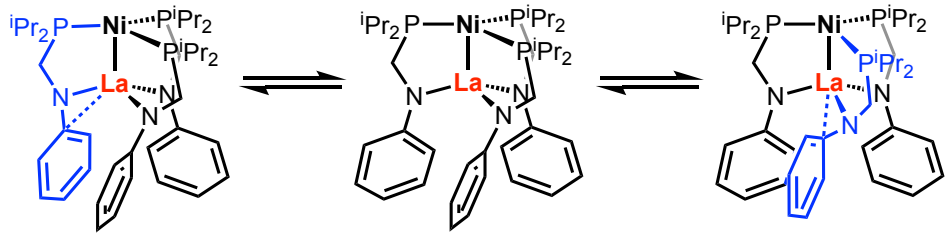

Figure S99. Proposed η^2-(C_{ipso}–N) bonding interaction between NPh and La in **8'**, which is in equilibrium with C_3 symmetric **8** in non-coordinating solvents. At room temperature, this interaction rapidly exchanges between the 3 aryl rings, leading to the appearance of a C_3-symmetric species.

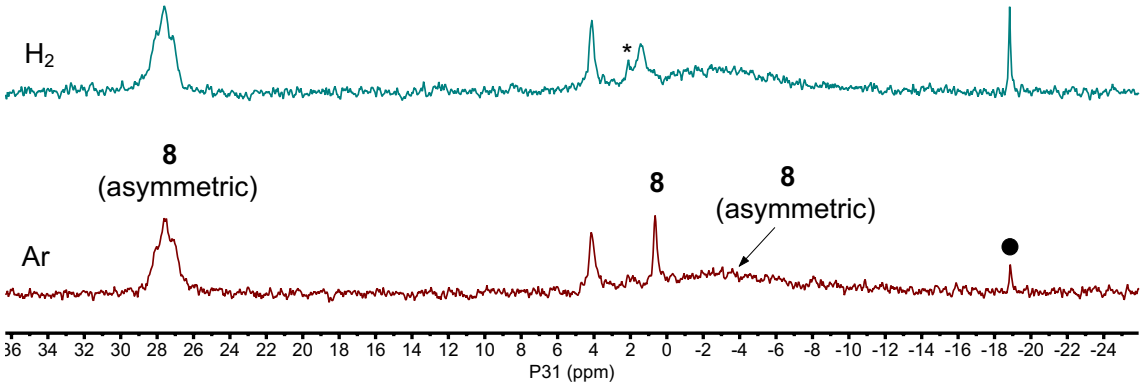

Figure S100. $^{31}P\{^{1}H\}$ NMR (162 MHz, toluene–d_8) spectra of **8** under Ar and 4 atm H_2 (at rt) cooled to –83 °C. The similarity between the two spectra indicates that H_2 binding does not contribute to any of the observed species. Isopropylphosphine, a decomposition product for **8**, is denoted by a circle (•). Residual water in H_2 gas results in the formation of a small amount of Pr_2PCH_2NHPh is denoted by an asterisk (*).

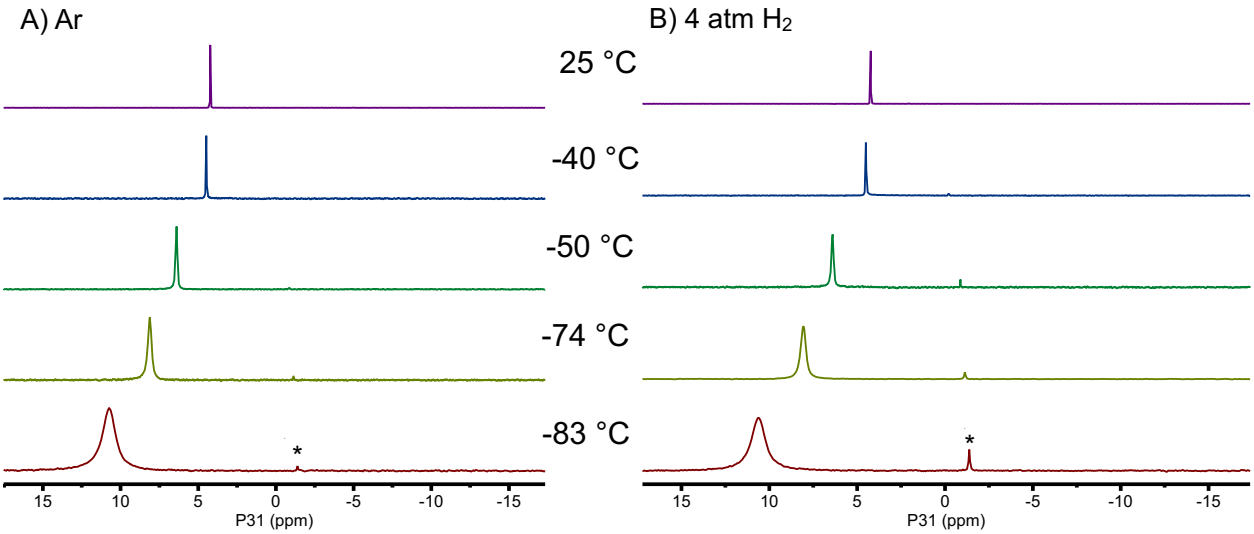

Figure S101. $^{31}P\{_1H\}$ NMR (162 MHz, THF–d_8) overlays of **8** under A) Ar and B) 4 atm H_2 (at rt) cooled to –83°C. Upon cooling, independent of the gas atmosphere, the ^{31}P resonance shifts 6.5 ppm downfield to 10.7 ppm. Due to the identical shift and broadening between the 4 atm H_2 and Ar spectra, the shift in ^{31}P resonance is associated with THF binding to form **8**–THF rather than H_2 binding. Residual water in H_2 gas or THF–d_8 results in the formation of a small amount of Pr_2PCH_2NHPh denoted by an asterisk (*), which is only observable at low temperatures where the complex signals have greatly broadened.

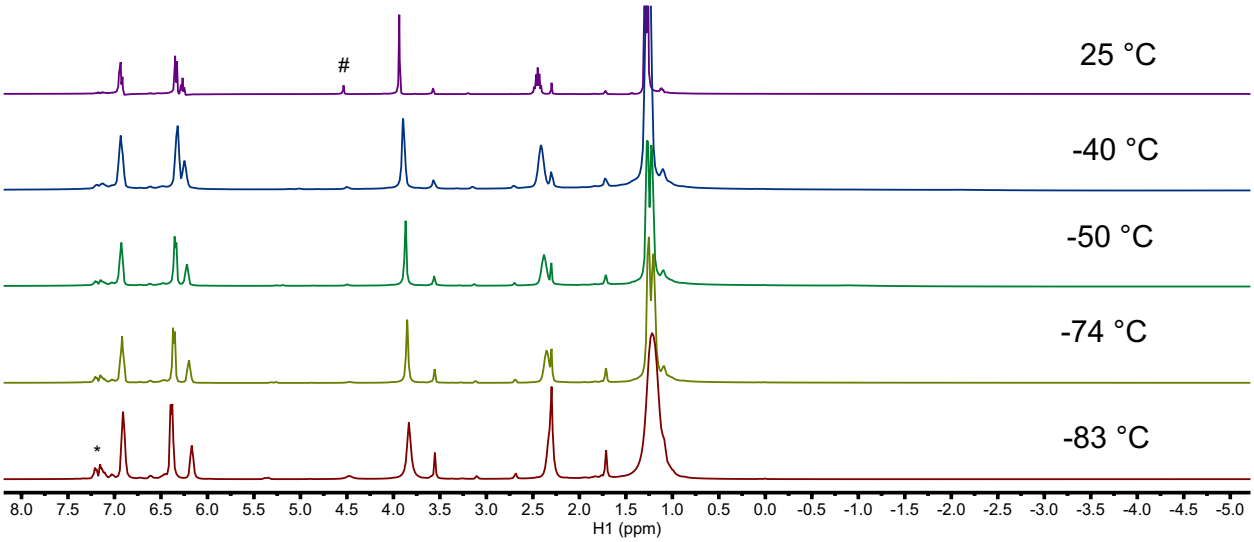

Figure S102. Variable temperature $^1H\{^{31}P\}$NMR (400 MHz, THF–d_8) spectra of **8** under 4 atm H_2 at rt. The ^1H resonance of free H_2 in THF–d_8 is denoted by a pound sign (#). Upon cooling, a discrete bound H_2 proton resonance is not observed and the free H_2 ^1H resonance does not shift. Therefore, with at the conditions attainable, an **8**(H_2) species can't be observed. Residual toluene solvent is denoted by an asterisk (*).

Substrate Scope Representative ^{1}H NMR Spectra

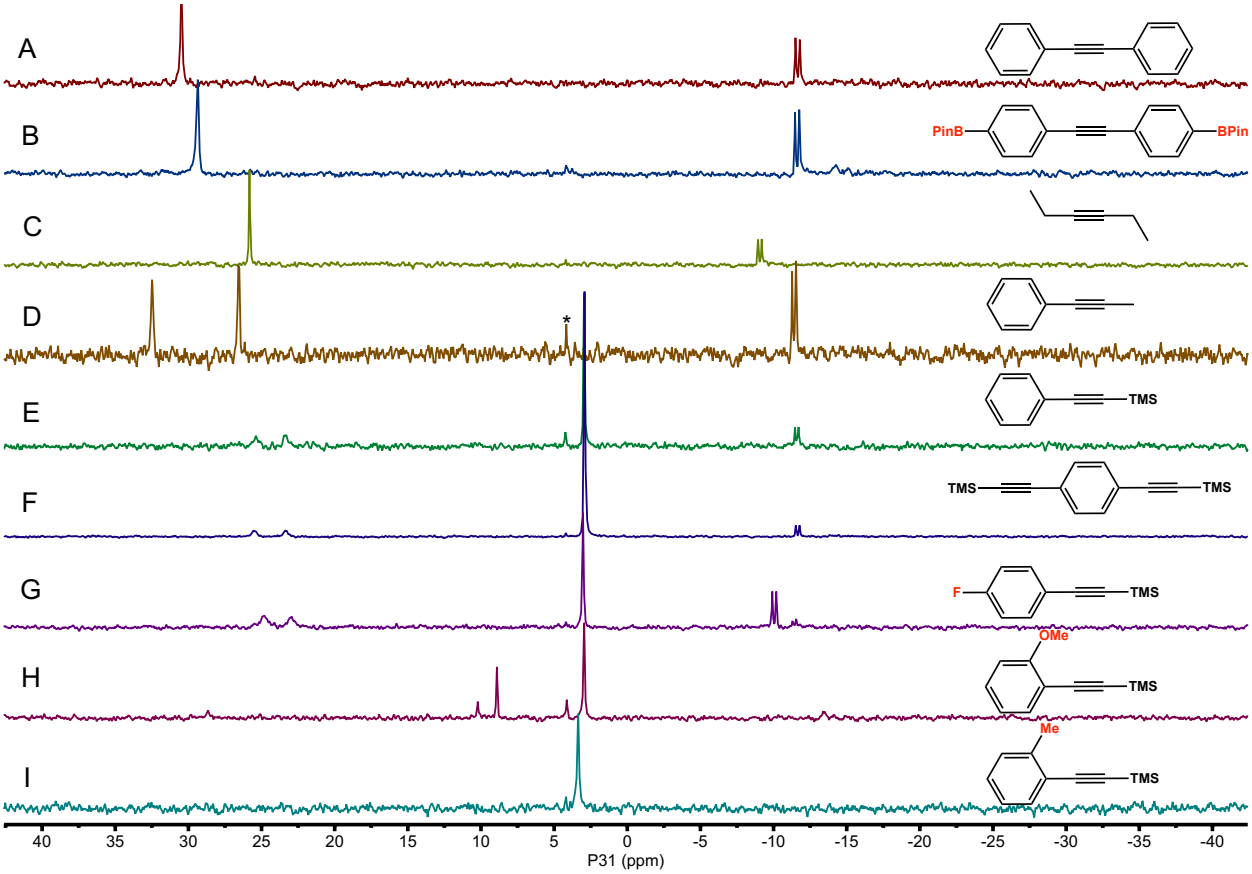

Figure S103. $^{31}P\{^{1}H\}$ NMR (162 MHz, toluene–d_8) spectra overlay of $NiYL_3$ **7** treated with 40 equiv. of various alkynes: A) diphenylacetylene, B) diphenylacetylene-4,4'-diboronic acid bis(pinacol) ester, C) 3–hexyne, D) 1-phenyl-2-propyne, E) 1-phenyl-2-trimethylsilylacetylene, F) 1,4-bis[1,1-bis(trimethylsilyl)ethenyl]benzene, G) (4-fluorophenylethynyl)trimethylsilane, H) 2-[(Trimethylsilyl)ethynyl]anisole, I) 2-[(Trimethylsilyl)ethynyl]toluene.

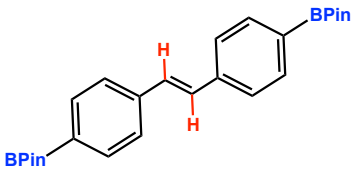

[22]**(*E*)–stilbene–4,4'-diboronic acid bis(pinacol) ester (10b)**: ^{1}H NMR (400 MHz, toluene–d_8): δ 8.05 (d, ^2J = 7.7 Hz, 4H), 7.33 (d, ^2J = 7.8 Hz, 4H), 6.93 (s, 2H), 1.14 (s, 24H). Alkyne conversion was >99%. Alkene NMR yield: 99% (E:Z >99). Catalyst loading was 2.5%.

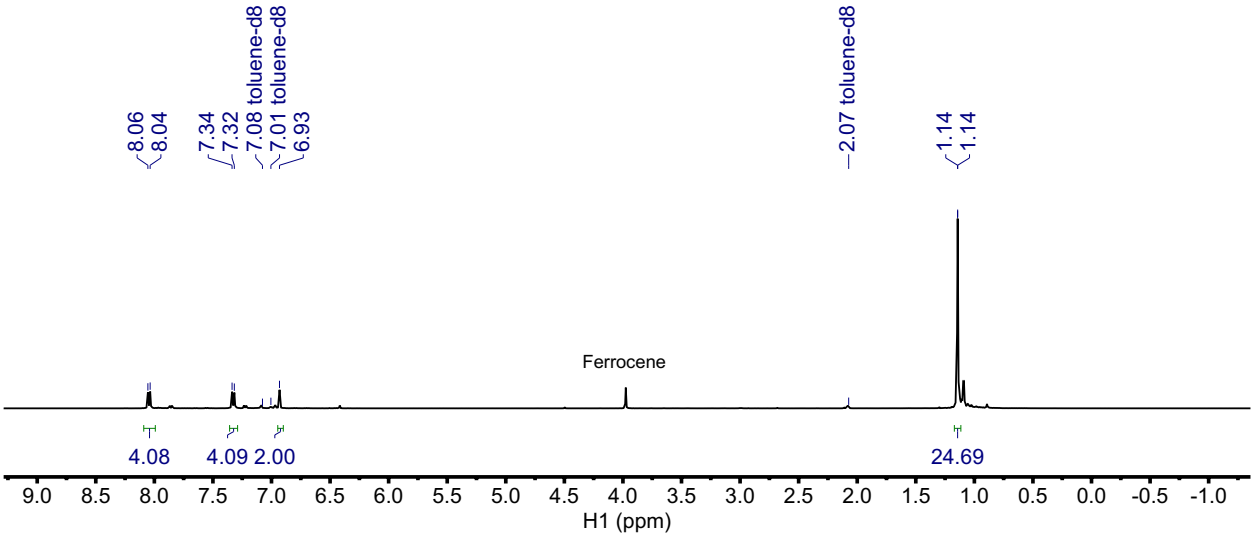

Figure S104. Representative ^{1}H NMR spectrum (400 MHz, toluene–d_8) of the catalytic semihydrogenation of diphenylacetylene-4,4'-diboronic acid bis(pinacol) ester by **7** (2.5 mol %, 70°C, 24 h). Ferrocene used as integration standard.

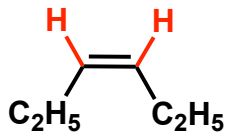

[23]**(*Z*)–3-hexene (10c)**: ^{1}H NMR (400 MHz, toluene–d_8): δ 5.33 (t, J = 4.8, 2H), 2.96 (m, 6, 2H), 0.90 (m, 6H). Alkyne conversion was >99%. Alkene NMR yield: 95% (E:Z 1: 99). Catalyst loading was 2.5%.

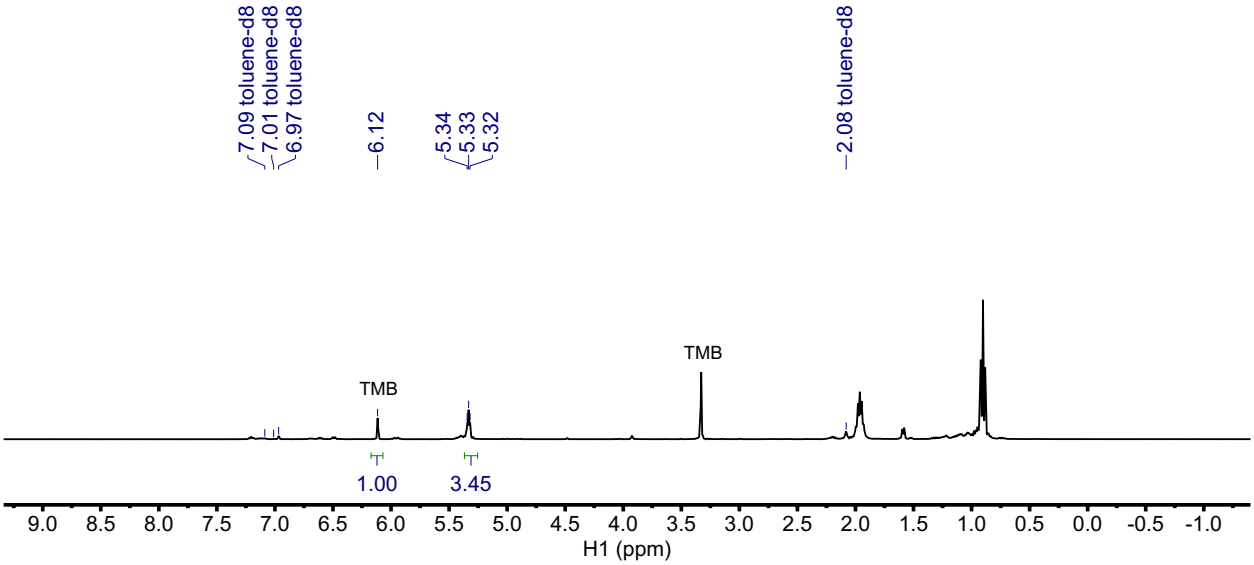

Figure S105. Representative ^{1}H NMR spectrum (400 MHz, toluene–d_8) of the catalytic semihydrogenation of 3–hexyne by **7** (2.5 mol %, 70°C, 8 h).

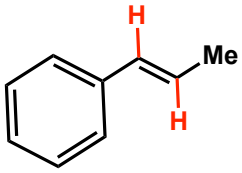

[24]**(*E*)–1–phenyl–1–propylene (10d):** Alkyne conversion: >99%. Alkene NMR yield: 86% (E:Z >99). Catalyst loading was 2.5%.[1]H NMR signals used in quantification (toluene–d_8, 400 MHz): 1–phenyl–1–propyne: 7.43 (d, J = 7.15 Hz); (*E*)–1–phenyl–1–propylene: 6.30 (d, J = 15.6, 1 H); (*Z*)–1–phenyl–1–propylene: 5.62 (dq, J = 14.0, 7.2 Hz, 1 H); 1–phenylpropane: 2.45 (t, J = 7.7 Hz, 3 H).

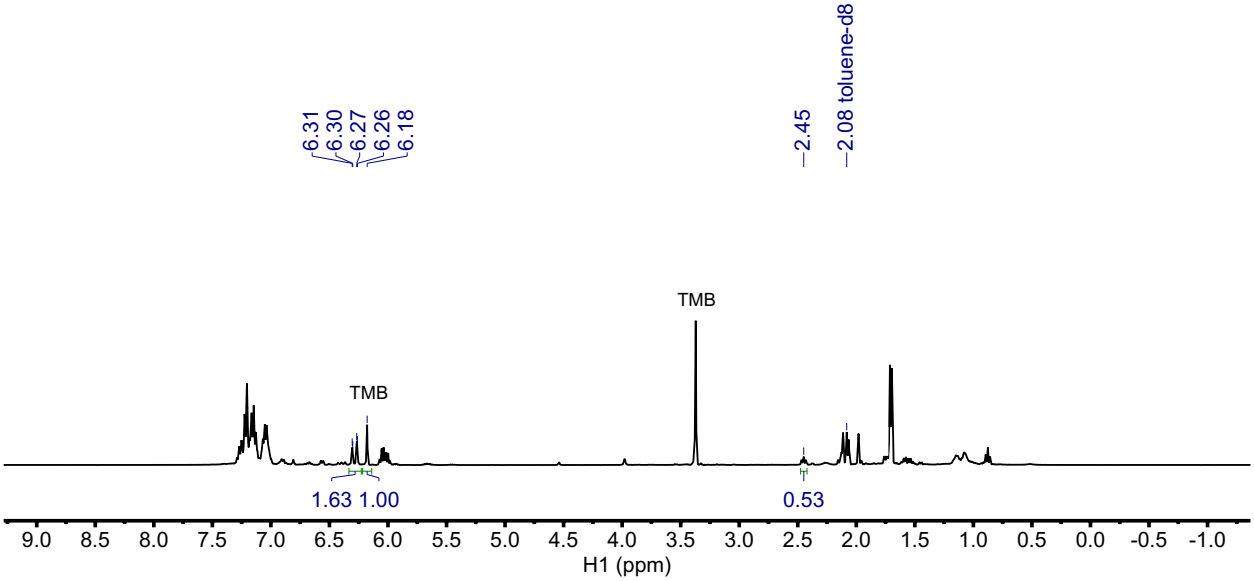

Figure S106. Representative [1]H NMR spectrum (400 MHz, toluene–d_8) of the catalytic semihydrogenation of 1-phenyl-2-propyne by **7** (2.5 mol %, 70°C, 24 h). Integrations used to quantify conversion are labeled.

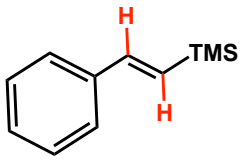

[23]**(*E*)–1-phenyl-2-(trimethylsilyl)ethene (10e)**: [1]H NMR (400 MHz, toluene–d_8): δ 7.26 (d, J = 7.6, 2H), 7.11 (t, J = 7.5, 2H), 7.04 (t, 1H), 6.88 (d, J = 19.1, 1H), 6.42 (d, J = 19.2, 1H), 0.15 (s, 9H). Alkyne conversion was >99%. Alkene NMR yield: 97% (E:Z >99). Catalyst loading was 2.5%.

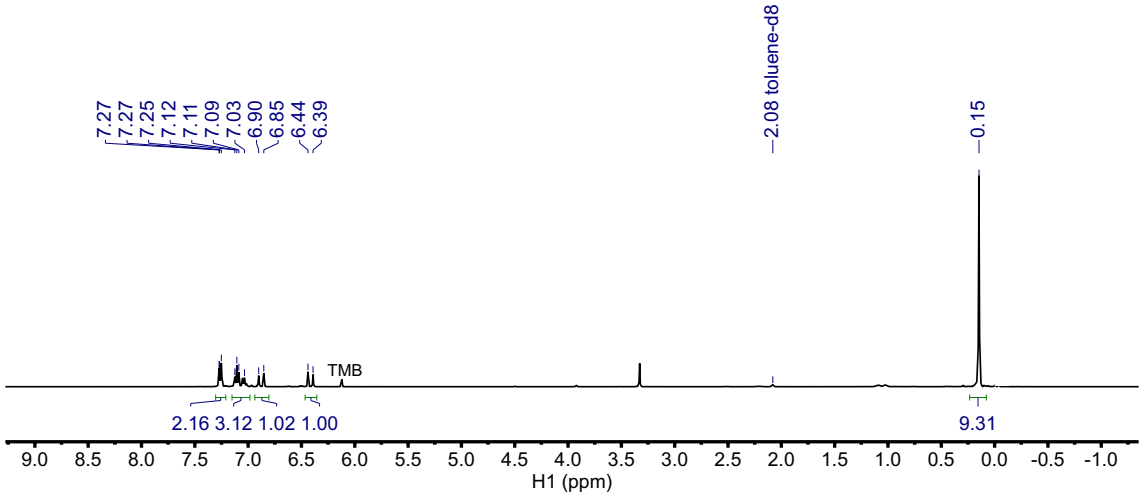

Figure S107. Representative [1]H NMR spectrum (400 MHz, toluene–d_8) of the catalytic semihydrogenation of 1-phenyl-2-trimethylsilylacetylene by **7** (2.5 mol %, 70°C, 24 h).

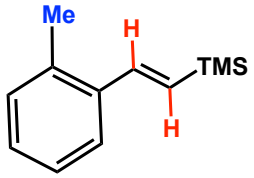

[3]**(*E*)–trimethyl(2-methylstyryl)silane (10f):** [1]H NMR (400 MHz, toluene–d_8): δ 7.44 (d, J = 7.3, 1.9 Hz, 1H), 6.39 (d, J = 19.0 Hz, 1H), 7.10–6.87 (m, 3H), 6.34 (d, J = 19.0 Hz, 1H), 2.16 (s, 3H), 0.16 (s, 9H). Alkyne conversion was >99% after 60h. NMR yield: 96% (E:Z >99). Catalyst loading was 2.5%.

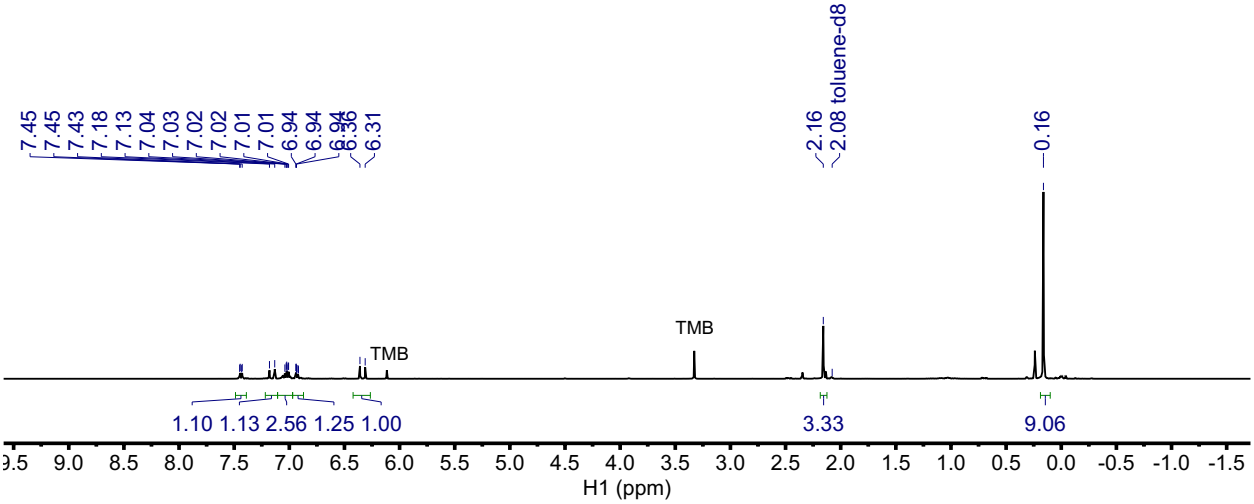

Figure S108. Representative [1]H NMR spectrum (400 MHz, toluene–d_8) of the catalytic semihydrogenation of 2-[(Trimethylsilyl)ethynyl]toluene by **7** (5 mol %, 70°C, 24 h).

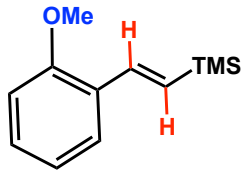

[3]**(*E*)–(2-methoxystyryl)trimethylsilane (10g):** [1]H NMR (400 MHz, toluene–d_8): δ 7.59 (d, ^2J = 19.3, 1H), 7.49 (d, ^2J = 7.7, 1.7 Hz, 1H), 7.23 (t, ^2J = 7.7 Hz, 1H), 6.82 (t, ^2J = 7.6, 1H), 6.49 (d, ^2J = 7.6 HZ, 1H), 6.47 (d, ^2J = 19.5, 1H), 3.30 (s, 3H), 0.17 (s, 9H). Alkyne conversion was >99%. Alkene NMR yield: 96% (E:Z >99). Catalyst loading was 3.5%.

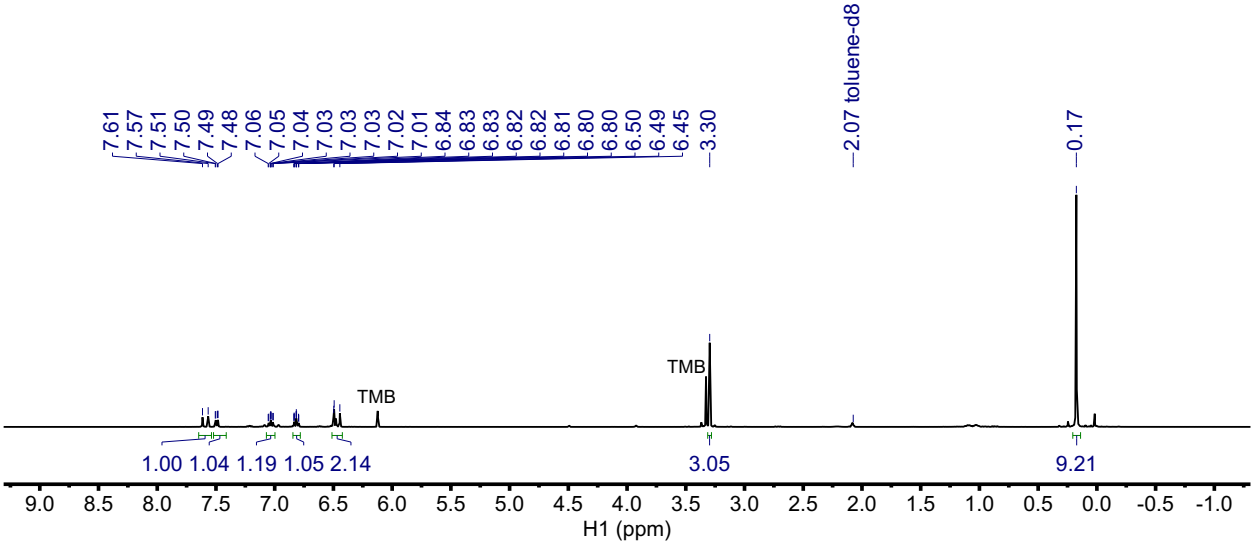

Figure S109. Representative [1]H NMR spectrum (400 MHz, toluene–d_8) of the catalytic semihydrogenation of 2-[(Trimethylsilyl)ethynyl]anisole by **7** (3.5 mol %, 70°C, 24 h).

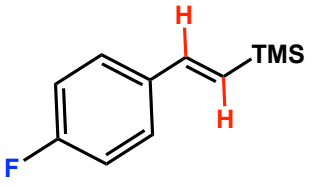

[24]**(*E*)–2–(4-fluorophenylethenyl)trimethylsilane (10h):** Alkyne conversion was 65%. Alkene NMR yield: 65% (E:Z >99). Catalyst loading was 5%. ^{1}H NMR signals used in quantification (toluene–d_8, 400 MHz): (4-fluorophenylethynyl)trimethylsilane: 6.51 (t, ^2J = 8.77 Hz, 2H); (*E*)–2–(4-fluorophenylethenyl)trimethylsilane: 6.82 (d, ^2J = 19.1 Hz, 1H); (*Z*)–2–(4-fluorophenylethenyl)trimethylsilane: 5.73 (d, ^2J = 19.0 Hz, 1H); trimethyl(4-fluorophenethyl)silane: 2.39 (m, 2H).

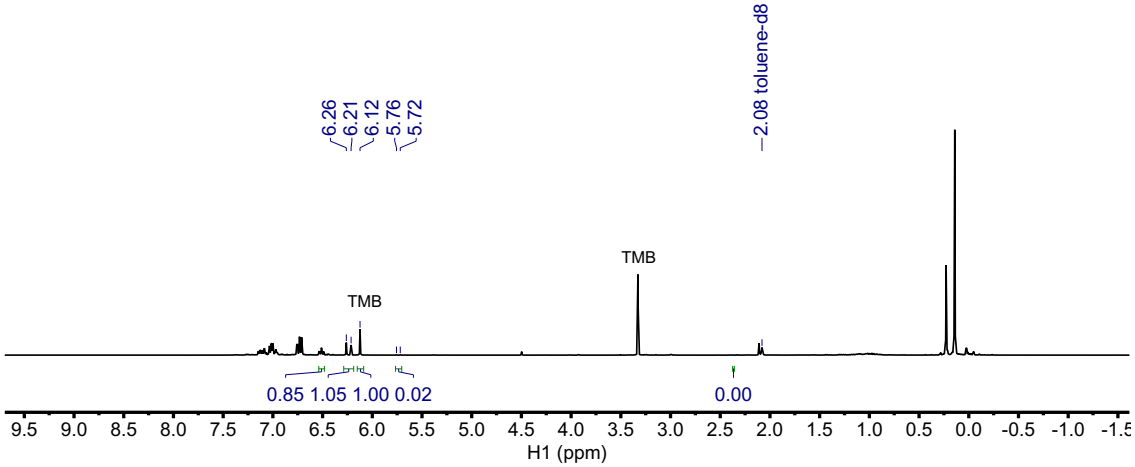

Figure S110. Representative ^{1}H NMR spectrum (400 MHz, toluene–d_8) of the catalytic semihydrogenation of (4-fluorophenylethynyl)trimethylsilane by **7** (2.5 mol %, 70°C, 24 h). Integrations used to quantify conversion are labeled.

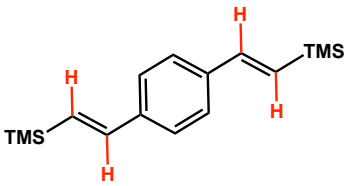

[3]**1,4-bis((E)-2-(trimethylsilyl)vinyl)benzene (10i):** ^{1}H NMR (400 MHz, toluene–d_8): δ 7.26 (s, 4H), 6.89 (d, J = 19.1, 2H), 6.45 (d, J = 19. 2 H), 0.1 (s, 18H). Alkyne starting material conversion: >99%. Alkene NMR yield: 88% (E:Z >99). remainder of yield is mono-hydrogenated alkene. Catalyst loading was 2.5%.

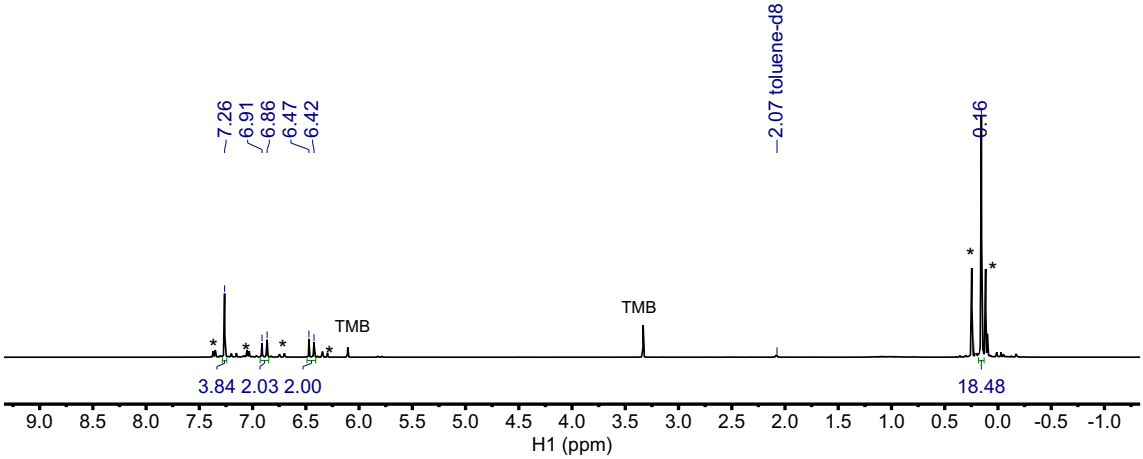

Figure S111. Representative ^{1}H NMR spectrum (400 MHz, toluene–d_8) of the catalytic semihydrogenation of 1,4-bis[1,1-bis(trimethylsilyl)ethenyl]benzene by **7** (2.5 mol %, 70°C, 48 h). The mono–hydrogenated product trimethyl-[2-[4-[(*E*)-2-trimethylsilylethenyl]phenyl]-ethynyl]silane (12 % NMR yield) is marked by an asterisk (*).

References

(1) Ramirez, B. L.; Sharma, P.; Eisenhart, R. J.; Gagliardi, L.; Lu, C. C. Bimetallic nickel-lutetium complexes: tuning the properties and catalytic hydrogenation activity of the Ni site by varying the Lu coordination environment. *Chem. Sci.* **2019**, *10*, 3375-3384.

(2) Thomson, R. K.; Scott, B. L.; Morris, D. E.; Kiplinger, J. L. Synthesis, structure, spectroscopy and redox energetics of a series of uranium(IV) mixed-ligand metallocene complexes. *Comptes Rendus Chimie* **2010**, *13*, 790-802.

(3) Tokmic, K.; Fout, A. R. Alkyne Semihydrogenation with a Well-Defined Nonclassical Co–H_2 Catalyst: A H_2 Spin on Isomerization and E-Selectivity. *J. Am. Chem. Soc.* **2016**, *138*, 13700-13705.

(4) Blessing, R. An Empirical Correction for Absorption Anisotropy. *Acta Crystallogr., Sect. A: Found. Crystallogr.* **1995**, *51*, 33.

(5) Sheldrick, G. SHELXT - Integrated Space-group and Crystalstructure Determination. *Acta Crystallogr., Sect. A: Found. Adv.* **2015**, *A71*, 3.

(6) Sheldrick, G. Crystal Structure Refinement with SHELXL. *Acta Crystallogr. Sect. C: Struct. Chem.* **2015**, *C71*, 3.

(7) Hubschle, C. B.; Sheldrick, G. M. ShelXle: A Qt Graphical User Interface for SHELXL *J. Appl. Crystallogr.* **2011**, *44*, 1281.

(8) Spek, A. Structure Validation in Chemical Crystallography. *Acta Crystallogr. Sect. D: Biol. Crystallogr.* **2009**, *65*, 148.

(9) Spek, A. PLATON SQUEEZE: a tool for the calculation of the disordered solvent contribution to the calculated structure factors. *Acta Crystallographica Section C* **2015**, *71*, 9-18.

(10) Atkins, P. W.; Overton, T. L.; Rourke, J. P.; Weller, M. T.; Armstrong, F. A., *Shriver and Atkins' Inorganic Chemistry*. 5th ed.; Oxford University Press: New York, 2010. For Y, Lu, La: the pK_a for hydrolysis of M^{3+}; titration of 0.004-0.009 M $M(ClO_4)_3$ with 0.2M $Ba(OH)_2$; I = 0.3($NaClO_4$) was used. For Sc and Ga; the pK_a for hydrolysis of M^{3+}; I =0.5 or 1($NaClO_4$) was used.

(11) Shannon, R. Revised effective ionic radii and systematic studies of interatomic distances in halides and chalcogenides. *Acta Crystallographica Section A* **1976**, *32*, 751-767.

(12) Pyykkö, P. Additive Covalent Radii for Single-, Double-, and Triple-Bonded Molecules and Tetrahedrally Bonded Crystals: A Summary. *J. Phys. Chem. A* **2015**, *119*, 2326-2337.

(13) Pyykkö, P.; Atsumi, M. Molecular Single-Bond Covalent Radii for Elements 1–118. *Chem. Eur. J.* **2009**, *15*, 186-197.

(14) Pauling, L. Atomic Radii and Interatomic Distances in Metals. *J. Am. Chem. Soc.* **1947**, *69*, 542-553.

(15) Cordero, B.; Gómez, V.; Platero-Prats, A. E.; Revés, M.; Echeverría, J.; Cremades, E.; Barragán, F.; Alvarez, S. Covalent radii revisited. *Dalton Trans.* **2008**, 2832-2838.

(16) Perrin, D. D., *Ionisation Constants of Inorganic Acids and Bases in Aqueous Solution*. Oxford, UK, 1982.

(17) Rinehart, N. I.; Kendall, A. J.; Tyler, D. R. A Universally Applicable Methodology for the Gram-Scale Synthesis of Primary, Secondary, and Tertiary Phosphines. *Organometallics* **2018**, *37*, 182-190.

(18) Desrosiers, P. J.; Cai, L.; Lin, Z.; Richards, R.; Halpern, J. Assessment of the "T1 criterion" for distinguishing between classical and nonclassical transition-metal hydrides: hydride relaxation rates in tris(triarylphosphine)osmium tetrahydrides and related polyhydrides. *J. Am. Chem. Soc.* **1991**, *113*, 4173-4184.

(19) Luther, T. A.; Heinekey, D. M. Synthesis, Characterization, and Reactivity of Dicationic Dihydrogen Complexes of Osmium and Ruthenium. *Inorg. Chem.* **1998**, *37*, 127-132.

(20) Cammarota, R. C.; Lu, C. C. Tuning Nickel with Lewis Acidic Group 13 Metalloligands for Catalytic Olefin Hydrogenation. *J. Am. Chem. Soc.* **2015**, *137*, 12486-12489.

(21) Cammarota, R. C.; Clouston, L. J.; Lu, C. C. Leveraging molecular metal–support interactions for H_2 and N_2 activation. *Coord. Chem. Rev.* **2017**, *334*, 100-111.

(22) Baltus, C. B.; Chuckowree, I. S.; Press, N. J.; Day, I. J.; Coles, S. J.; Tizzard, G. J.; Spencer, J. Olefin cross-metathesis/Suzuki–Miyaura reactions on vinylphenylboronic acid pinacol esters. *Tetrahedron Letters* **2013**, *54*, 1211-1217.

(23) Pinkas, J.; Gyepes, R.; Císařová, I.; Kubišta, J.; Horáček, M.; Mach, K. Steric Effects in Reactions of Decamethyltitanocene Hydride with Internal Alkynes, Conjugated Diynes, and Conjugated Dienes. *Organometallics* **2014**, *33*, 3399-3413.

(24) Wang, Y.; Qin, C.; Jia, X.; Leng, X.; Huang, Z. An Agostic Iridium Pincer Complex as a Highly Efficient and Selective Catalyst for Monoisomerization of 1-Alkenes to trans-2-Alkenes. *Angew. Chem. Int. Ed.* **2017**, *56*, 1614-1618.